Optimizing Ion-Shuttling Operations in Trapped-Ion Quantum Computers

by

Luke Qi

Submitted to the Department of Physics
in partial fulfillment of the requirements for the degree of

Bachelor of Science in Physics

at the

MASSACHUSETTS INSTITUTE OF TECHNOLOGY

June 2021

© Luke Qi 2021. All rights reserved.

The author hereby grants to MIT permission to reproduce and to distribute publicly paper and electronic copies of this thesis document in whole or in part in any medium now known or hereafter created.

Author . . . .
Department of Physics
May 14, 2021

Certified by . . . .
Isaac L. Chuang
Professor of Physics and Electrical Engineering
Thesis Supervisor

Certified by . . . .
John Chiaverini
MIT Lincoln Laboratory Technical Staff
Thesis Supervisor

Accepted by . . . .
Deepto Chakrabarty
Associate Department Head, Department of Physics

Optimizing Ion-Shuttling Operations in Trapped-Ion Quantum Computers

by

Luke Qi

Submitted to the Department of Physics
on May 14, 2021, in partial fulfillment of the
requirements for the degree of
Bachelor of Science in Physics

Abstract

Trapped ions are a promising candidate for quantum computation. As experiments with ions increase in size and complexity, a trap array-based architecture for an ion trap with many independent zones provides a path towards large-scale integration. A crucial element in the operation of a trap array is the ability to split, move and recombine chains of ions on diabatic timescales and without incurring excessive decoherence of information stored in ion qubits. In this thesis, I investigate whether ion transport and splitting can be realistically integrated in the future quantum processor and what the requirements are to achieve this.

I discuss my end-to-end numerical simulation pipeline of the ion shuttling process. Using these simulation tools, I investigate the leading theories for ion transport and splitting, based on Shortcuts-to-Adiabaticity principles, and extend these methods into two central criteria for optimal ion shuttling. I present a novel method for optimizing the voltage controls to achieve optimal ion shuttling, that use accurate models of the digital-to-analog converters, amplifiers, and low-pass filters of our ion trapping system.

I demonstrate fast and robust transport of ^{40}Ca on our custom-designed surface electrode trap and share spectroscopy data taken during the first ever attempt at optimal splitting. I then outline the necessary steps to achieve fast splitting with less than 1 quanta of excitation. It is my hope that the theories, software, and experimental results presented in this thesis demonstrate the feasibility of optimal ion transport and splitting in state-of-the-art, scalabale surface traps and become a standard for future ion shuttling experiments.

Thesis Supervisor: Isaac L. Chuang
Title: Professor of Physics and Electrical Engineering

Thesis Supervisor: John Chiaverini
Title: MIT Lincoln Laboratory Technical Staff

Acknowledgments

It's pretty trippy to look back at the years and retrospectively chart your trajectory through life. There are a few doors that you stumble through that end up blossoming into unexpected yet wonderfully exciting territories.

One such door for me was joining Professor Isaac Chuang's quanta group back in the Fall of 2019. My experience since then has led to growth in ways I could have never imagined as a small freshman hoping to be an aerospace engineer. Along the way I've gotten to meet terrific people who have improved my life.

First and foremost is Mr. Jules Stuart. I don't think I could ever overstate the impact you've had on my experience both in Ike's lab and research in general. Since the very beginning, when I had no idea what was wrong with my simulations, you've been incredibly patient and supportive. Thank you for the late night hackathons, the tea spilling over multiple messaging platforms, and giving me some real solid advice about grad schools. Working with you has been such an excellent experience that I actually don't think I've fully comprehended what research without you will be like. I'll be happy if I could have a fraction of your energy and bandwidth for making sure the experimentalists survive and even thrive.

To Professor Ike Chuang, thank you for inspiring me to be a better student and researcher. Your seemingly endless pockets of knowledge, your stories from your undergraduate and graduate years, and your passion for learning has made me want to do it all (but we can't all be Ike). Every group meeting I find myself pondering and digesting your advice and words of wisdom.

To Dr. John Chiaverini, thank you for being such an involved and helpful advisor. I'm always impressed by your attention to detail and how you manage to ask me questions that I have no good answer to. Working with you has inspired me to be more thorough and meticulous in my incoming graduate journey.

To Dr. Jeremy Sage, thank you for making me feel welcome ever since I attended my first group meeting in 2019. Thank you also for connecting with Pro-

fessor Gonzalo Muga; conversations with his group has been a fun experience for me. It's been cool that we could still connect through MIT iQuHACK and I appreciate your support throughout all of it.

To Dr. Susanna Todaro, thank you for always helping me, no matter how busy you are. Even though I'm still finishing this acknowledgements section on May 14th, I'd be in an even worse spot if you hadn't told me to start writing a month ago. I really appreciate everything you do for lab culture, you make academia feel warm (or maybe its the spicy margaritas talking).

To Mr. Gabriel Mintzer, thank you for your hopeful and supportive soul. Seeing you in lab at late hours and getting slack reacts at 4am makes me feel a sense of camaraderie. I don't know how you manage everything on your plate and still are able to assure me about my incoming thesis deadline.

To Mr. Felix Knollman, Mr. "I'm no beginner" and is actually an expert. Thank you for messaging me about climbing and I promise I'll go soon. I've enjoyed our conversations both academic and non-academic, I'm always pleasantly surprised at the similar interests we share. Also, wink ;)

To Mr. Kyle DeBry, thank you for reaching out to me about research topics. Your suggestions have been quite helpful and I'm quite inspired by your work ethic, knowledge, and wit.

To Mr. Xiaoyang Shi, thank you for your calm and level-headed energy. Hanging with you at IP-QGIPSHRE has been a blast.

To Professor Gonzalo Muga, it has been a pleasure working with you and your team. Thank you for your flexibility to find meeting times that work for both of us. I've also enjoyed hearing about Spanish siesta and would love to implement it in my own life.

A special thanks to my roommate, Mr. Soor Vora, who has been kind enough to hold off on watching TV while I write this thesis.

A.G.S and D.J.C., you two already know how much you mean to me.

I reserve the biggest thank you for my mom, dad, brother, uncle, and cat Mr. Oliver Wood.

Contents

1 Introduction **21**

1.1 Ion Array Trap Architecture 22

1.2 Ion Shuttling 24

1.2.1 Primitive Operations 25

1.2.1.1 Transport 25

1.2.1.2 Splitting and Merging 26

1.2.1.3 Reordering 27

1.2.2 State-of-the-Art Experiments 28

1.2.2.1 Shuttling Demonstrations 28

1.2.2.2 Quantum Algorithms 29

1.3 This Work 30

1.3.1 Contributions and Publications 31

2 Trapping Ions **33**

2.1 RF Paul Traps 34

2.1.1 Surface Electrode Trap 39

2.2 Motional Dynamics 42

2.2.1 Micromotion 42

2.2.2 Secular Motion 43

2.2.3 Normal Modes 45

2.3 Electrical Controls 46

3 **Numerical Simulation Pipeline** **49**
3.1 Modelling the Surface Electrode Trap 50
3.2 Solving for Voltage Waveforms 51
3.2.1 Ion Trap Voltage Generation 55
3.2.1.1 Calculating Potentials 55
3.2.1.2 Calculating Voltages 57
3.3 Electrode Circuit Simulation 59
3.4 ODE Solver 60

4 **Optimal Ion Shuttling** **65**
4.1 Transport Profiles 66
4.1.1 Shortcuts-to-Adiabaticity 68
4.1.2 Fourier Excitation 73
4.2 Splitting Profiles 79
4.2.1 Shortcuts-to-Adiabaticity 82
4.2.2 Fourier Excitation 86
4.3 Robustness 90
4.3.1 Experimental Non-Idealities 92
4.4 Summary 93

5 **Voltage Optimization** **95**
5.1 Spectral Content of Voltage Waveforms 98
5.2 Deconvolution 100
5.3 Local Minimization 103

6 **Experimental Results** **107**
6.1 Electrode Circuitry Characterization 107
6.2 Diabatic Ion Transport 111
6.3 Splitting Spectroscopy 114
6.4 Equally-Spaced Ion Chains 120
6.5 Summary 123

7 Conclusion **125**

List of Figures

1-1 An illustration of the ion array trap. 23

1-2 Start of the split. $\alpha \geq 0$, $\beta = 0$ 27

1-3 The critical point. $\alpha = 0$, $\beta \geq 0$ 27

1-4 End of the split. $\alpha \leq 0$, $\beta \geq 0$ 27

2-1 A diagram of a quadrupole trap adapted from [4]. (a) An oscillating voltage is applied to the rf electrodes while the other two are held at rf ground. The ion is located near the center of the trap, where the resulting electric field is zero (rf null). The field lines show the ion is confined in the radial ($\hat{x}$, $\hat{z}$) directions. (b) The four electrodes can be extended as rods in the axial ($\hat{y}$) direction. The rf ground can be segmented and a DC voltage can be applied, providing axial confinement to the two ions. 35

2-2 A schematic of the quadrupole trap being unfolded into a surface trap, adapted from [4]. The rf null is now above the plane of the trap. The rf ground electrodes can be segmented along the axial direction (into the page). 40

2-3 An diagram of the Standard Lincoln Trap. Each electrode has a name and corresponding number. The pitch of the DC electrodes 2–8, and 13–19 is 120 μm. Electrodes 10 and 11 serve to finely adjust the orientation of the ion's principle directions. $\hat{y}$ is the axial direction. 41

2-4 A diagram of the MaxBeta trap. Same coordinate system as the SLT 2-3. Position $y = 0$ μm is right between electrodes S10 and N10. 45 μm pitch on the smaller electrodes, and 74 μm on the larger electrodes. The rf electrodes lie on the outside of the DC electrodes. Electrodes S22, S23, S24, S25 serve to tilt the ion's principle directions. 42

2-5 A schematic of the rf amplification circuitry, created by Mr. Jules Stuart. 47

3-1 An diagram of the ion motion experiment process. The gold boxes denote the input and output of our system. We care about finding the best voltage inputs to shuttle ions optimally. 49

3-2 A harmonic potential on the MaxBeta trap at 186.5 μm. Grid file resolution is 1 μm. A quadratic potential is taylor fitted (red) on the potential calculated with superposition (blue dots). The potential is also calculated through coefficient expansion, with great agreement. 56

3-3 A double well potential centered at 186.5 μm. The superposed potential (blue dots) and coefficient expansion potential (dashed green) differ further from the expansion point. The coefficients from forward ITVG and taylor fitting the superposed potential (dashed red) differ by 12%. 56

3-4 Transport waveforms on the SLT. The voltages ocassionally hop between two solution sets that have similar cost function values. 58

3-5 An example of a time-domain simulation of electrode filtering with LTSpice. The input signal is shown as piece-wise linear discrete step function (blue). The circuit output is shown in orange. The dashed black line shows a target waveform for this electrode. 60

3-6 Simulation of the trajectory of ^{88}Sr under a harmonic oscillator moving with protocol shown in dashed black. Ion position relative to the potential minimum shown in blue and uses the right-hand y-axis scale. The ion's motion during the "heat calculation window" is used to determine the motional excitation after transport 61

3-7 An FFT of the ^{43}Ca ion located an a harmonic potential and interacting with a ^{43}Ca and ^{86}Sr ions. 63

4-1 Various transport profiles plotted in black. Acceleration determined using numerical derivatives, plotted in red and using the right-hand scale. 67

4-2 Motional excitation calculated by determining the classical energy of the ion's motion at the end of transport. The trajectory of ^{88}Sr in a rigid 1.2 MHz trap under the various transport profiles is calculated with my ODE solver. 68

4-3 A 3D representation of the tanh transport profile. The electric potential (V) is plotted along the z axis. $\hat{y}$-position and time plotted in the x and y axis. This particular transport is from 0 μm to 120 μm. 69

4-4 Profiles in time of various STA trajectories and hyperbolic tangent. . 74

4-5 Same excitation plot as Fig 4-2 but with more simulated STA trajectories. The quantized excitation from all three STA protocols is synonymous with zero. 74

4-6 STA 9th order polynomial. 76

4-7 Sinusoidal transport 76

4-8 Linear transport 76

4-9 Hyperbolic tangent, $N = 5$ 76

4-10 Slice of spectrograms at the 1.2 MHz axial frequency. 77

4-11 A typical splitting profile from [31]. Motional excitation from splitting (red), thermal excitation from electric field noise (blue), and total energy transfer (black). The top right inset shows the axial frequency (black) and heating rate (red) during transport. 81

4-12 STA splitting profile with a flat COM frequency (solid red). The stretch frequency (dashed red) starts off at $\sqrt{3}$ and ramps down to almost be equal to the COM frequency. The quadratic, α, coefficient ramps down to -0.5 its initial value (blue). The quartic, β, term reaches a maximum value at the critical point (orange). 84

4-13 Motional excitation in quanta of the common mode oscillation after two types of splitting profiles. Thermal heating from the trap has not been simulated. 85

4-14 Axial frequency modes during the two methods of splitting. 85

4-15 Spectrogram of STA splitting. The common mode frequency is set to be 1.2 MHz for ^{40}Ca, and scales inversely with the mass for higher-mass ions. 87

4-16 Slice of the STA splitting spectrogram at the various axial frequencies corresponding to the ion's mass. 87

4-17 Simulation of two ^{40}Ca ions with my splitting profile. $d(t)$ is given by an STA solution (4.23). The ions get separated ×10 their starting distance. Note how the ions follow an STA profile during the 5 μs split. 88

4-18 Comparisons of my splitting profile with the same two in Fig 4-13. The quanta plotted is the excitation in the common mode. 89

4-19 Transporting a single ^{88}Sr ion with the polynomial STA (4.23) and the trigonometric STA (4.24). The correct axial frequency for transport is 1.2 MHz, but transport with a frequency of 1.0 MHz has also been simulated. 91

5-1 Ion transport waveforms on the MaxBeta trap. Transporting ^{40}Ca according to an STA polynomial protocol (4.23), over a distance of 45 μm in 15 μs. The axial frequency is 4 MHz. 96

5-2 Splitting waveforms on the MaxBeta trap. Splitting two ^{40}Ca according to my developed method in chapter 4. $d(t)$ according to (4.23), COM frequency of 1.2 MHz. Final ion separation of 90 μm. . 97

5-3 DAC input voltages modelled with a piece-wise linear function (blue). Analog output simulated with SPICE (orange). The target waveform is what we want to apply to the trap electrodes (dashed black). 97

5-4 Spectral content of diabatic transport voltages. The total transport time is 4 μs. 99

5-5 Naively sampled voltages. DAC update rate of 1000ns. 99

5-6 Schematic of our circuitry in LTSpice. Our DAC inputs are modelled as piecewise linear functions applied at "Vinput". The stages "End of Fastino" and "End of HVamp" and labeled. The voltage output at "ION" is our expected electrode voltage. 100

5-7 Impulse response of our electrode circuitry. 100

5-8 Magnitude of the transfer function 101

5-9 Phase of the transfer function. Phase delay: $\frac{\phi}{f}$. Group delay: $\frac{\mathrm{d}\phi}{\mathrm{d}f}$ . . 101

5-10 Deconvolved signal (red) of the target waveform for electrode N9 (black). The analog output of the deconvolved signal is simulated in SPICE (blue). 102

5-11 Sampling the deconvolved signal. Time (μs) plotted on the x-axis. The timing of the voltages are better than the naive voltages, but there's uncontrolled oscillations at the end. 104

5-12 After an optimization cycle. Time (μs) plotted on the x-axis. Smooths out the ending oscillations to better match the target waveform. . . . 104

6-1 The output of the Fastino with a 0 to 2.5 V step input. The cable from the HD68 Fastino connector and the oscilloscope was modelled as a 100 pF parasitic capacitor. 108

6-2 Fastino + HVamp output with 2.5 to 5 V and 5 to 2.5 V input steps. 109

6-3 Circuit model for the EMI filter. 110

6-4 The fitted transfer function is shown in dotted black and the measured data points is shown in blue. The χ^2-probability is 98%. 110

6-5 Full circuit output with output with 2.5 to 5 V and 5 to 2.5 V input steps. 110

6-6 Measurements of S13 waveform (blue) and simulated waveform (dashed black). (a) bang-bang (b) predistorted dt = 1000 ns (c) predistorted dt = 600 ns (d) predistorted dt = 800 ns. 112

6-7 Measured waveform (blue) and simulated waveform (dashed black) for electrode S13 with an adjusted DAC model. (a) bang-bang (b) predistorted dt = 1000 ns (c) predistorted dt = 600 ns (d) predistorted dt = 800 ns. 113

6-8 Sideband data during a slow motion split. Each horizontal trace is a different index of the splitting waveform, starting with index 1 at the bottom and reaching index 83 at the top. The difference between the two sideband peaks gives the mode frequency. The vertical bars shows the expected sideband location for a COM frequency of 1.2 MHz (red) and a stretch frequency of 2.1 MHz (green). 115

6-9 Expected and measured axial frequencies during a slow motion split. 115

6-10 Simulated spectroscopy after adding various Ez fields, shown on the y-axis. The vertical bars show the experimentally measured frequencies at index 15. Based on this scan, an optimal E_z field is $\sim$9.5 V/cm 116

6-11 Spectroscopy tuning 118

6-12 Simulated spectroscopy with measured data overlaid. The bars show the measured data. Each horizontal trace represents a different time step along the split, with index 0 at the bottom and index 83 at the very top. 119

6-13 Funky potential on the MaxBeta! 120

6-14 The frequency of the four axial modes in a chain of four ^{40}Ca ions spaced by 5 μm. 122

List of Tables

1.1 State of the art experimental demonstrations of ion shuttling operations. 29

3.1 A summary of hyperparameters for voltage solving. 58

6.1 Voltages for $E_z = 1$ V/cm on the MaxBeta, applied at a position of $(x, y, z) = (0, 186.5, 50)$ μm. Electrode names correspond to positions in Fig 2-4. 116

6.2 α and β values for a 4-, 5-, and 9-ion ^{40}Ca chain. [a]For a purely harmonic potential with an α value confines an ion at frequency $\omega_0 = \sqrt{2\alpha q/m}$. [b]The maximum beta value, β_0 on our trap is $2{\times}10^{-7}$ V/m^4. 121

6.3 Voltages for achieving a quartic potential to equally space four ^{40}Ca ions. Electrode names correspond to positions in Fig 2-4. 122

Chapter 1

Introduction

Quantum computation with trapped-ions has achieved numerous milestones over the past decades [6, 12]. Single-qubit rotations [9, 25, 2, 20], two-qubit gates [2, 20, 1], qubit state preparation [14] and readout [47] have all been demonstrated with fidelities that approach or exceed the high threshold for fault tolerant quantum computing [49]. Additionally, the long coherence times achievable with trapped-ions has allowed them to be a front-running physical qubit candidate in the Noisy Intermediate-Scale Quantum (NISQ) regime [59, 35, 79].

Scaling the current quantum systems beyond the NISQ regime of 50-100 noisy qubits remains a formidable engineering challenge. In trapped-ion systems, multiple ions in a single chain (or crystal) will interact with one another via the Coulomb force. These interactions can lead to experimental challenges as one tries to increase the number of ions in a single chain. Longer ion crystals are harder to control, resulting in a higher rate of decrystallization and increased sensitivity to environmental noise. Furthermore, addressing each ion qubit in a long chain requires an optical system with a complexity that scales unfavorably with the number of qubits. Lastly, long ion chains exhibit tightly packed frequency modes that can lead to crosstalk errors on unaddressed qubits. Quantum gates mediated by the Coulomb interaction must be performed slower on longer chains to avoid these crosstalk errors.

A proposed solution towards scalability that addresses the aforementioned challenges takes advantage of a crucial concept in the development of classical technologies: modularity. Rather than increasing the size of a single ion chain, one may choose to use multiple smaller chains that can communicate quantum information to one another [33, 80]. This modular architecture would increase the number of possible quantum gates while keeping the largest ion chain at a manageable size. A drawback to a modular trapped-ion quantum processor is the time required to communicate between ion chains. Any time spent on transferring quantum information decreases the time available for quantum gates before the qubit states decohere. Thus to fully reap the benefits of modularity, one must implement a communication scheme that is reliable and fast, compared to the speed of typical two-qubit gates ($\sim$30 μs) [12].

Multiple methods have been developed for transferring quantum information between ions, including the use of photonic links, lattice arrays, and ion shuttling operations [46, 13, 62]. Ion shuttling operations have gained traction over the past decade and have been experimentally implemented to varying degrees of success, as I will discuss in section 1.2. I define a "shuttling" operation as controlling the motion of trapped-ions along a specified trajectory using time-dependent electric fields. Multiple operations fall under the category of shuttling, as I will explain in section 1.2.1.

This thesis will tackle some of the outstanding questions in ion shuttling research: What are the most optimal methods for shuttling ions in state-of-the-art ion traps? What are the required specifications on our hardware to perform optimal shuttling? In a practical setting with a scalable trap architecture, is there a way to seamlessly integrate shuttling operations in large-scale quantum computing algorithms?

1.1 Ion Array Trap Architecture

One type of ion trap that has demonstrated potential for large-scale quantum computing is the ion array trap or Quantum Charge-Coupled Device (QCCD),

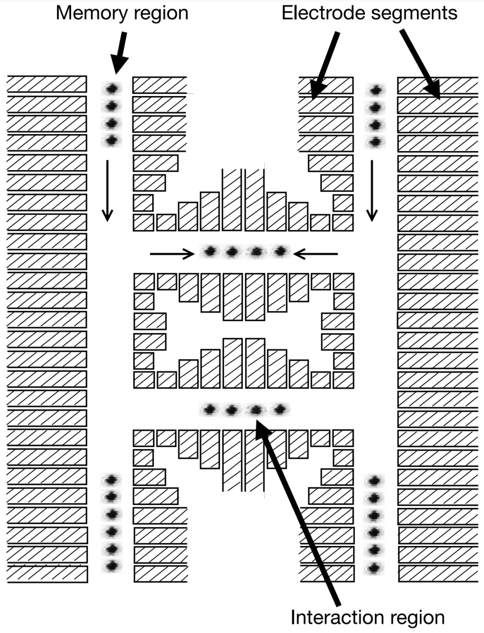

Figure 1-1: An illustration of the ion array trap originally from [33]. The segmented electrodes can be controlled to transport ion chains from one region to the next. Some ion qubits may be stored in the "memory region" while others can be transported into the "interaction region" to be used in a quantum gate.

shown in Fig 1-1 [33, 80]. The ion array trap/QCCD consists of radio frequency (rf) electrodes that confine ions in two (radial) dimensions, and segmented "DC" electrodes that provides confinement in the third (axial) direction. The trap electrodes produce potentials that are most often harmonic in the three confinement directions, although more complex, anharmonic potentials have been used and will be discussed in this thesis. The DC electrodes can be individually controlled to produce time-varying electric potentials that move ions along the axial direction (drawn as lanes in diagram 1-1). "Waveforms" is the accepted term to describe the time-dependent voltages that are applied to the DC electrodes, and will be used frequently throughout this thesis. The physics of ion motion in this trap architecture will be discussed more thoroughly in Chapter 2.

This ion trap array profitably allows for small ion chains to exist in separated regions, which can each be specialized for a specific task. These tasks may comprise the various parts of a quantum algorithm, including ion loading, single-qubit rotations, two-qubit gates, memory storage, and state readout.

1.2 Ion Shuttling

A qubit is typically encoded in the electronic or spin states of a trapped-ion, which are generally decoupled from its motional state. This is not true, however, during most two-qubit entangling gates, where the motional states of the ions acts as a bus to transmit quantum information. Otherwise, during non-gate times, ion qubits can be physically transported from one register to the next without losing its quantum information [62].

Although the qubit is protected during shuttling operations, there are still constraints to consider when performing shuttling operations. First, we require that the shuttling operation adds minimal excitation to the ion qubit's motional state because the fidelity of any subsequent gate decreases with ion qubit temperature. One could potentially remove the ion qubit's excitation by shuttling it along with an ancilla ion[1] to sympathetically cool the qubit after shuttling. Sympathetic cooling requires the ancilla ion to be of a different species, so the laser frequencies will not interact with the qubit ion, but the motion between the two ions is shared and cooled together. The downside to this strategy is that sympathetic cooling is a slow process (on the order of ms), which greatly sacrifices time that could be spent performing quantum gates.

This leads to the second constraint on shuttling, which asserts that the time required to perform shuttling operations should be negligible compared to gate times, for the reasons discussed previously. These heat and time constraints end up intertwined in most trapped-ion systems. Ions naturally become excited over time due to the electric field noise from electronics and other anomalous surface effects [65, 10]. Therefore with long shuttling operation times, the ion qubit will experience more motional excitation from the ion trap, violating the first constraint.

Conversely, longer shuttling times typically means the electric potential varies slower in time. In this case, the change in the ion qubit's Hamiltonian falls under the adiabatic regime, $T\frac{\mathrm{d}\lambda}{\mathrm{d}t} \ll \lambda$ [71], in other words λ varies only slightly during a period T of motion. An ion qubit is highly likely to remain in the same eigenstate after an adiabatic change, ΔH, in the Hamiltonian, so if the qubit starts with no motional excitation before shuttling, it is likely to end with no motional excitation. However, shuttling time in the adiabatic regime is many multiples of the ion's motional period (which is usually around 1 μs in typical ion traps) and places the total operation time comparable to ion gate times. Faster-than-adiabatic shuttling that do not excite the ions is possible, and must be accomplished delicately and with precise control over the changes in the ion qubit's Hamiltonian[2].

---

[1] an ion that does not encode any quantum information

These trade-offs between fast and cold shuttling are quite necessary to consider when engineering shuttling protocols with realistic system parameters. The most optimal shuttling operations do not excite the ion qubits and can be performed as fast as possible, given the specifications of the electronic control system.

1.2.1 Primitive Operations

There are only a few basic shuttling operations that are crucial for achieving modular trapped-ion quantum computation. These are the ability to transport ions from one chain to another, join and remove ions from a chain, and reorder the ions within a chain.

1.2.1.1 Transport

The most common method for transporting an ion is to move the harmonic potential along the axial direction with individually-controlled DC electrodes [27]. Typically one would also like to keep the curvature of the harmonic potential in the axial direction constant throughout the transport operation. Curvature is defined as the second derivative of the potential along a specified axis; ions placed in a potential with axial curvature α, will experience a frequency of oscillation in the axial direction, ω_0, given by,

---

[2] methods to achieve faster-than-adiabatic shuttling will be discussed in chapter 4

$$\phi(y) = \alpha(y - q_0)^2 = \frac{1}{2}\frac{m}{q}\omega_0^2(y - q_0)^2 \tag{1.1}$$

$$\omega_0 = \sqrt{\frac{2q\alpha}{m}} \tag{1.2}$$

where ϕ is the electric potential in the axial direction ($\hat{y}$ will be the axial direction in this thesis), q_0 is the location of the potential minimum, and q, m are the charge and mass of the ion, respectively.

To vary the harmonic potential, one can simply change the location of the potential minimum, q_0, as a function of time. The trajectory, $q_0(t)$, is called a transport "profile"—an infinite number of profiles are possible, both only a subset are worth considering. Certain profiles lead to less ion excitation during adiabatic transport times, while others can lead to no excitation at very specific transport times in the faster-than-adiabatic regime.

Although we can prescribe any profile we desire, there is no guarantee that we can perfectly achieve this potential on realistic ion trap. We can only apply finite voltages to a finite set of segmented electrodes, which vary in shape and layout from one ion trap to the next. Therefore it is important to consider profiles that not only lead to fast and cold ion transport, but are also robust against deviations from the desired trajectory.

1.2.1.2 Splitting and Merging

Splitting an ion chain canonically requires a fourth order potential [31],

$$\phi(y) = \alpha y^2 + \beta y^4 \tag{1.3}$$

where the coefficients α and β are implicit functions of time. One can start with a purely harmonic potential ($\beta = 0$), start decreasing α while increasing β until a "critical point" is reached, in which $\alpha = 0$ and the ions are confined by the quartic coefficient only. Afterwards α may become to be negative to effectively act as a

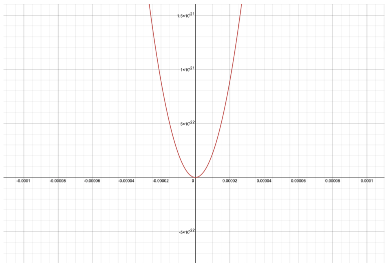

Figure 1-2: Start of the split. $\alpha \geq 0$, $\beta = 0$

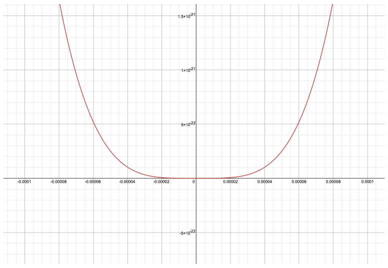

Figure 1-3: The critical point. $\alpha = 0$, $\beta \geq 0$

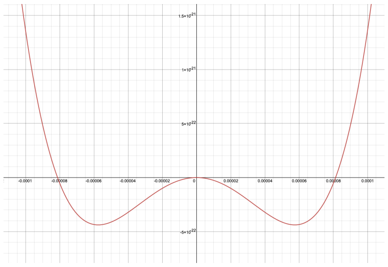

Figure 1-4: End of the split. $\alpha \leq 0$, $\beta \geq 0$

wedge to force the ion chain apart. This process is shown in Figs 1-2,1-3,1-4.

A splitting "profile" can thus be achieved by cleverly engineering the coefficient trajectories, $\alpha(t)$ and $\beta(t)$. Similar considerations of imperfect voltage controls discussed for ion transport also exist for ion splitting. Most notably, a large quartic coefficient may prove to be very difficult to achieve on certain trap architectures [50]. Furthermore, the axial confinement that ion crystals experience in a quartic well is significantly reduced compared to a quadratic well [26], and thus a large β value is needed at the critical point to keep the axial confinement high[3].

Due to these reasons, it is considerably more difficult to keep the ion confinement constant during a splitting operation than it is during transport. These added challenges are reflected in the state-of-the-art experimental demonstrations (Table 1.1), where cold, diabatic transport has been achieved, but splitting below 1 quanta of energy and faster than 50 μs remains an open challenge.

Merging of ion crystals can be achieved by reversing the splitting profile.

1.2.1.3 Reordering

While I will not investigate the reordering of ion crystals in this thesis, this is still a beneficial operation to increase the connectivity in a future trapped-ion quantum processor.

Multiple methods exist for reordering an ion chain, all of which have been demonstrated experimentally. The first method is to rotate the ion crystal in a plane, temporarily bringing the crystal out of the axial direction [73, 77, 55, 58].

---

[3] it is advantageous to keep the axial confinement high, as will be explained in chapter 4.

A second method is to transport ions through a junction and changing the order in which one transports the ions back [80, 6]. Finally, in particular situations where higher levels of motional excitation are acceptable, one can rotate an chain of mixed-species ions by increasing the confinement along the crystal axis, and thereby squeezing the various ion species different amounts, creating a new shape that one can relax back into a linear crystal [8].

The above methods are all considered shuttling operations, however one can also reorder the qubits encoded in an ion crystal without physically shuttling the ions by performing a SWAP operation [69].

1.2.2 State-of-the-Art Experiments

Leading trapped-ion groups have experimentally demonstrated ion shuttling operations to various degrees of success. Ion transport, arguably the most straightforward of the basic primitive operations, has been well executed at fast speeds with low motional excitation. The more complex operations of splitting, transport through junction, and ion crystal rotation, has been successfully performed at slower speeds. Shuttling operations have not only been demonstrated in isolation, but they have also been incorporated within quantum algorithms.

1.2.2.1 Shuttling Demonstrations

A full overview of experimental shuttling demonstrations can be found in Table 1.1. Most of the basic primitive operations have been implemented with low-mass ions. This is partly because lighter ions, such as ^{9}Be+ and ^{40}Ca+, are able to be trapped with smaller voltages than heavier ions due to their high charge-to-mass ratio [7, 32]. Linear transport has been demonstrated on diabatic time scales with very low heat gain. Splitting, however, has only been achieved on adiabatic time scales, with single digit quanta gain. Ion chain reordering has found the most success through crystal rotation, with low heat gain achieved on fast adiabatic timescales [67]. Transport through junctions has been accomplished, but the

Experiment	**Operation(s)**	**Species**	**Group**	**Time (μs)**	**Heat (quanta)**
Shuttling Primitives	Transport	^{40}Ca	Mainz [76]	3.6	0.1
		^{9}Be	NIST [7]	8	0.1
	Splitting	^{9}Be–^{9}Be	NIST [7]	55	2
		^{40}Ca–^{40}Ca	Mainz [63]	80	4.16
Ion Chain Reordering	Rotation	^{40}Ca–^{40}Ca	Mainz [29]	42	0.05
		^{40}Ca–^{40}Ca	Innsbruck [73]	25	(0.6, 3.9)
	X-Junction	^{9}Be	NIST [6]	350	0.1
		^{9}Be–^{9}Be	NIST [5]	1000	1.7
CNOT Gate Teleportation	Transport, Split/Join	^{9}Be, ^{24}Mg	NIST [78]	2980	—
		^{171}Yb, ^{133}Ba	Honeywell [58]	3000-5000	<2

Table 1.1: State of the art experimental demonstrations of ion shuttling operations.

speed of the transport was limited by the heating of the ion from the update noise of the digital-to-analog converter [5, 6].

Some open shuttling problems include, but are not limited to, diabatic splitting of ion chains with less than 1 quanta gained, and the splitting/joining of mixed-species ions. Lastly, diabatic transport of mixed-species ion chains has yet to be experimentally demonstrated, although there have been theoretical investigations into this problem [51].

1.2.2.2 Quantum Algorithms

Recently, ion trapping experimental groups have been able demonstrate quantum algorithms using ion qubits trapped in a segmented electrode array. NIST and Honeywell Quantum Solutions were each able to combine single- and two-qubit gates, along with fast transport and splitting, to execute a quantum circuit that teleports a CNOT gate with high fidelity [78, 58]. Schmidt-Kaler's group at the University of Mainz used shuttling operations to create an long-lived Greenberger-Horne-Zeilinger state [30]. Average shuttling operations in these algorithms took hundreds of microseconds and required sympathetic cooling to the ground state, adding a time overhead of a couple miliseconds. While these results show the feasibility of the ion array trap paradigm in a future processor, more work needs to be done to achieve cold, fast, and also robust shuttling operations.

1.3 This Work

The main focus of my thesis is aimed at achieving optimal and robust ion transport and ion chain splitting on surface electrode traps[4]. Many of the shuttling operations detailed in section 1.2.2 used a multi-layered Paul trap, and it still remains an open challenge to split an ion crystal with less than 1 quanta of heat gain with operation times that approach the diabatic regime ($\sim$10 μs). Ion transport and splitting comprise the majority of the shuttling operations in the recent quantum algorithm demonstrations in the NISQ era. Therefore, gaining the ability to perform optimal transport and splitting operations on modern surface electrode Paul traps paves the way for current trapped-ion quantum computers to achieve more quantum gate operations within a single quantum algorithm, thereby increasing the computational power of these NISQ devices. To this end I present a comprehensive simulation pipeline that takes into account previously overlooked system characterizations (e.g. sampling rate of our digital-to-analog converters), a method for optimizing voltage commands, and an analysis of the feasibility of achieving shuttling profiles on surface electrode traps using leading theories for optimal shuttling (e.g. Shortcuts-to-Adiabaticity).

Chapter 2 will introduce the theory of ion trapping and ion motion in rf Paul traps. Chapter 3 will discuss my numerical simulations of the ion shuttling process in detail. I will also describe the heuristics that I have found useful in solving for voltage waveforms. Chapter 4 will detail the theory behind fast and cold ion transport and splitting. Shortcuts-to-adiabaticity (STA) techniques and Fourier analysis will be discussed in detail. I will also describe my new method for generating splitting profiles that extends the STA method to allow for a wider family of trajectories. Chapter 5 will detail my method to predistort our system's electrode filtering in order to gain stronger control over our electrode waveforms. Finally, in Chapter 6 I will discuss the ion motion data taken on ion traps to demonstrate the feasibility of our approach. It is my hope that this thesis should serve as a starting reference for new methods of experimentally achieving robust diabatic transport and splitting on surface electrode traps.

---

[4] Paul traps, as well as surface electrode traps, will be discussed in the next chapter.

1.3.1 Contributions and Publications

My main contributions centers around developing full numerical simulations of the entire shuttling process. These simulation tools have allowed me to begin implementing shuttling operations based on shortcut-to-adiabaticity principles. Through a collaboration with Prof. Gonzalo Muga's theory group, we have begun investigations into STA solutions that are robust against system imperfections. Using my numerical tools, I have re-framed the shuttling problem into a spectral content analysis and developed a new approach to achieve cold, diabatic splitting.

I have developed heuristics for voltage solving on our new trap architecture. Experimentally, I have developed ion transport waveforms using STA protocols that use a novel method for optimizing control electrode voltages.

It is incredibly important to note that the design of the MaxBeta trap 2-4 was optimized and laid out by Mr. Jules Stuart. The high-voltage amplifier was designed and built by Mr. Jules Stuart, and the ion trapping and data collection on the MaxBeta trap, presented in chapter 6 was also done by Mr. Jules Stuart.

Some of the work in this thesis has been published in the following article(s):

1. **Qi, L.**, Chiaverini, J., Espinós, H., Palmero, M., & Gonzalo Muga, J. (2021). Fast and robust particle shuttling for quantum science and technology. arXiv e-prints, arXiv-2104. [60]

Chapter 2

Trapping Ions

Trapped-ion systems allow for some excellent studies of physics [4]. Ion traps can confine anywhere from single ions to large ion clouds for periods of seconds to multiple days, depending on the trap architecture. Ions confined in a trap may naturally reside far from nearby electrodes (on the order of hundreds of microns), allowing them to be well isolated from unwanted electrical forces. The dynamics of ions in various confining traps has been well-known and trap architectures have been developed and applied in various technologies, such as mass spectrometers, since the mid 1900s.

Samuel Earnshaw proved in 1842 that charged particles are unable to be held in stationary equilibrium in 3D using static electric forces alone [18]. This result can be most readily seen using Gauss's law in free space, which states the divergence of the electric field must vanish when there are no electric sources,

$$\nabla \cdot \vec{E} = 0 = \nabla \cdot (-\nabla \Phi_{\mathrm{st}}) \tag{2.1}$$

where Φ_{st} is an electric potential resulting from static electric fields alone.

One can hope that the static electric potential is confining in all three spatial directions, and model each direction as a harmonic potential with frequency ω_i,

$$\Phi_{\text{st}}(\vec{r}) = \frac{m}{2q}\left(\omega_x^2 x^2 + \omega_y^2 y^2 + \omega_z^2 z^2\right) \tag{2.2}$$

Unfortunately, we quickly see from the Laplacian operator in (2.1) that Φ_{st} can only be confining in at most two directions and must be anti-confining in at least one direction,

$$\nabla^2 \Phi_{\text{st}} = \frac{m}{q}\left(\omega_x^2 + \omega_y^2 + \omega_z^2\right) = 0 \tag{2.3}$$

Confinement in the third direction is still possible, however, and requires either static magnetic fields or oscillating electric fields, which has been well developed as Penning traps and Paul traps, respectively. This thesis will only focus on Paul traps, and introduce a more specific 2D version used in many quantum computing experiments, known as a surface electrode trap.

2.1 RF Paul Traps

Paul traps, named after Nobel laureate Wolfgang Paul [57], confine ions using radio-frequency electric fields. The earliest rf Paul traps were based on a quadrupole electrode configuration (Fig 2-1), with an oscillating rf voltage applied on two of the electrodes (rf electrodes) and the other two held at rf-ground (control electrodes). Over the course of a single oscillation period, the rf electrodes will switch between a higher and lower potential compared to the control electrodes, and thus the ion will experience confinement in a different direction.

Intuitively, the ion can be analogously related to a marble on a saddle. A marble sitting on a saddle landscape that is concave in one direction and convex in another will roll down in the anti-confining direction under the force of gravity. If the saddle landscape rotates at a suitable frequency to prevent the marble from falling too far in the anti-confining direction, the marble can actually be held in equilibrium at the saddle point.

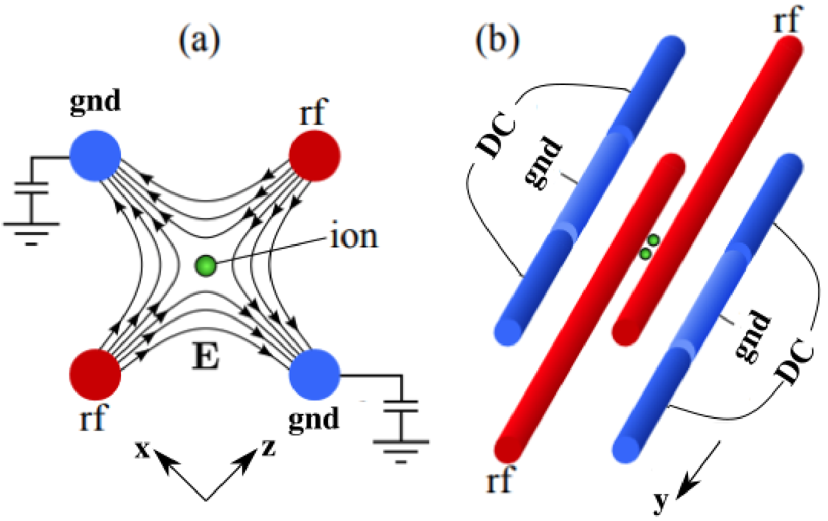

Figure 2-1: A diagram of a quadrupole trap adapted from [4]. (a) An oscillating voltage is applied to the rf electrodes while the other two are held at rf ground. The ion is located near the center of the trap, where the resulting electric field is zero (rf null). The field lines show the ion is confined in the radial ($\hat{x}$, $\hat{z}$) directions. (b) The four electrodes can be extended as rods in the axial ($\hat{y}$) direction. The rf ground can be segmented and a DC voltage can be applied, providing axial confinement to the two ions.

Similar physics allows ions to be confined in a quadrupole trap, however there are stability criteria on the voltage amplitude and frequency of the rf electrodes. Ions with smaller mass-to-charge ratios will experience a greater acceleration at the same voltage and thus require a higher oscillation frequency on the rf electrodes to remain stable. A full treatment of the dynamics of this Floquet (periodically driven) system has been well developed using Mathieu equations [44]. Solving these equations allows one to understand the complete ion motion in a quadrupole trap and is useful for determining the necessary parameters for stable ion trapping.

While the general Mathieu treatment leads to complete solutions of ion dynamics in Paul traps, we can simplify the problem using adiabatic approximations that are valid in a typical well-controlled quantum computing experiment. The adiabatic approximation holds when ions are stably confined near the center of the trap where there is no field, known as the "rf null" 2-1. The rf electrodes produce a field that oscillates at an appropriate frequency to ensure the ion does not move much during a single period. At any single point in time, the rf field strength varies over the length scale of the entire trap, but is roughly constant over the short distance scales of the ion's motion. We can then treat the oscillating rf electrodes as inducing a ponderomotive force. The resulting oscillating potential can be treated as a static "pseudopotential".

We start the derivation of the pseudopotential with the well-known electric potential of the quadrupole trap shown in Fig 2-1 [28].

$$\Phi_{\mathrm{rf}}(\vec{r},t) = \frac{\kappa}{2}\left(1+\frac{z^2-x^2}{R^2}\right) V_{\mathrm{rf}} \cos \Omega_{\mathrm{rf}} t \tag{2.4}$$

where V_{rf} and Ω_{rf} are the voltage amplitude and frequency on the rf electrodes, R is the distance from the quadrupole center to the electrodes, and κ is a geometric factor that depends on the shape and positioning of the electrodes. Note that I am only considering the radial directions of the trap, $\hat{x}$ and $\hat{z}$. The spatial and time dependence of the potential can be separated into $\tilde{\Phi}_{\mathrm{rf}}(\vec{r}) \cos \Omega_{\mathrm{rf}} t$.

Through the Lorentz force law we obtain that the ion experiences the following acceleration,

$$\ddot{\vec{r}} = -\frac{q}{m} \nabla \tilde{\Phi}_{\mathrm{rf}}(\vec{r}) \cos \Omega_{\mathrm{rf}} t = \frac{q}{m} \vec{E}_{\mathrm{rf}}(\vec{r}) \cos \Omega_{\mathrm{rf}} t \tag{2.5}$$

where $\vec{E}_{\mathrm{rf}}(\vec{r})$ is the rf electric field.

In a stable trapping configuration, the motion of the ion stays near the center of the trap, $|\vec{r}|$, while the spatial dependence of the rf electric field varies on the order of the trap size, R. Since $|\vec{r}| \ll R$ we can divide the motion into small and large length scales, and fast and slow time scales,

$$\vec{r} = \vec{r}_s + \vec{r}_\mu \tag{2.6}$$

$$\ddot{\vec{r}} = \ddot{\vec{r}}_s + \ddot{\vec{r}}_\mu = \frac{q}{m} \vec{E}_{\mathrm{rf}}(\vec{r}_s + \vec{r}_\mu) \cos \Omega_{\mathrm{rf}} t \tag{2.7}$$

where $\vec{r}_s$ is the slow, large amplitude (secular) motion and $\vec{r}_\mu$ is the fast, small amplitude (mirco)motion[1]. By definition $|\vec{r}_\mu| \ll |\vec{r}_s|$, and over the course of a single rf period the secular motion varies slowly, $|\ddot{\vec{r}}_s| \ll |\ddot{\vec{r}}_\mu|$.

We can thus Taylor expand the electric field around $\vec{r}_s$,

$$\vec{E}_{\mathrm{rf}}(\vec{r}_s + \vec{r}_\mu) \approx \vec{E}_{\mathrm{rf}}(\vec{r}_s) + \vec{r}_\mu \nabla \vec{E}_{\mathrm{rf}}(\vec{r}_s) \tag{2.8}$$

which we can plug back into eq (2.7) to obtain the following ion acceleration,

$$\ddot{\vec{r}}_s + \ddot{\vec{r}}_\mu = \frac{q}{m}\left(\vec{E}_{\mathrm{rf}}(\vec{r}_s) + \vec{r}_\mu \nabla \vec{E}_{\mathrm{rf}}(\vec{r}_s)\right)\cos\Omega_{\mathrm{rf}}t \tag{2.9}$$

In our adiabatic approximation we can safely say that $\ddot{\vec{r}}_\mu$ dominates the L.H.S. and $\vec{E}_{\mathrm{rf}}(\vec{r}_s)$ dominates the R.H.S. allowing us to split eq (2.17) into the following two contributions,

$$\ddot{\vec{r}}_\mu = \frac{q}{m}\vec{E}_{\mathrm{rf}}(\vec{r}_s)\cos\Omega_{\mathrm{rf}}t \tag{2.10}$$

$$\ddot{\vec{r}}_s = \frac{q}{m}\vec{r}_\mu \nabla \vec{E}_{\mathrm{rf}}(\vec{r}_s)\cos\Omega_{\mathrm{rf}}t \tag{2.11}$$

$\vec{E}_{\mathrm{rf}}(\vec{r}_s)$ essentially remains constant over one rf period, and we can time integrate eq (2.10) to obtain,

$$\vec{r}_\mu = -\frac{q}{m\Omega_{\mathrm{rf}}^2}\vec{E}_{\mathrm{rf}}(\vec{r}_s)\cos\Omega_{\mathrm{rf}}t \tag{2.12}$$

which we plug back into eq (2.11) to obtain the following secular acceleration,

$$\begin{aligned}\ddot{\vec{r}}_s &= -\frac{q^2}{m^2\Omega_{\mathrm{rf}}^2}\vec{E}_{\mathrm{rf}}(\vec{r}_s)\nabla\vec{E}_{\mathrm{rf}}(\vec{r}_s)\cos^2\Omega_{\mathrm{rf}}t \\ &= -\frac{q^2}{2m^2\Omega_{\mathrm{rf}}^2}\nabla\vec{E}_{\mathrm{rf}}^2(\vec{r}_s)\cos^2\Omega_{\mathrm{rf}}t \qquad (2.13) \\ \langle\ddot{\vec{r}}_s\rangle &= -\frac{q^2}{4m^2\Omega_{\mathrm{rf}}^2}\nabla\vec{E}_{\mathrm{rf}}^2(\vec{r}_s) \qquad (2.14)\end{aligned}$$

---

[1] secular motion and micromotion are the accepted terms and will be discussed in more detail later in this chapter

where we time-averaged over the rf period in the last step to get rid of the time dependence.

The time-averaged secular acceleration in (2.14) results from the standard ponderomotive force of oscillating electromagnetic fields. The electric potential gradient to create this ponderomotive force is what we call our pseuodopotential,

$$\Phi_{\text{ps}}(\vec{r}) = \frac{q}{4m\Omega_{\text{rf}}^2} \vec{E}_{\text{rf}}^2(\vec{r}_s) \tag{2.15}$$

Finally we can use the rf potential of a four-rod quadrupole trap we defined at the beginning of this section (2.4) to obtain the pseudopotential of the quadrupole in terms of rf voltage amplitude and rf frequency,

$$\Phi_{\text{ps}}(\vec{r}) = \frac{q\kappa^2 V_{\text{rf}}^2}{4m\Omega_{\text{rf}}^2 R^4} \left(x^2 + z^2\right) \tag{2.16}$$

Remarkably, we overcome Earnshaw's theorem and created a potential that is confining both the radial directions, $\hat{x}$ and $\hat{z}$. Modeling the pseudopotential in terms of a standard harmonic oscillator in the radial directions results in the following harmonic frequency,

$$\omega_{\text{rf}} = \frac{\kappa q V_{\text{rf}}}{\sqrt{2} m R^2 \Omega_{\text{rf}}} \tag{2.17}$$

We can now set the full electric potential as the sum of the pseudodopotential and static potentials, and also introduce the Hessian matrix of the energy potential, defined as a matrix of second derivatives,

$$\Phi_{\text{tot}}(\vec{r}) = \Phi_{\text{st}}(\vec{r}) + \Phi_{\text{ps}}(\vec{r}), \qquad \mathcal{H} \equiv q \begin{bmatrix} \frac{\partial^2}{\partial x^2} & \frac{\partial^2}{\partial x \partial y} & \frac{\partial^2}{\partial x \partial z} \\ \frac{\partial^2}{\partial y \partial x} & \frac{\partial^2}{\partial y^2} & \frac{\partial^2}{\partial y \partial z} \\ \frac{\partial^2}{\partial z \partial x} & \frac{\partial^2}{\partial z \partial y} & \frac{\partial^2}{\partial z^2} \end{bmatrix} \Phi(\vec{r}) \tag{2.18}$$

Recall that the second derivatives are often referred to as the "curvature" of the potential. For any arbitrary electric potential, one can discretize the values in

3D space and numerically calculate the Hessian matrix. The eigenvalues, λ_i, of the Hessian matrix can be used to find the principle frequencies, $\omega_i = \sqrt{\lambda_i/m}$, while the corresponding eigenvectors point in the direction of the principal axes of motion.

In our case, the full Hessian matrix can be expressed as follows,

$$\mathcal{H}_{\text{tot}} = m \begin{bmatrix} \omega_{\text{rf}}^2 + \omega_x^2 & 0 & 0 \\ 0 & \omega_y^2 & 0 \\ 0 & 0 & \omega_{\text{rf}}^2 + \omega_z^2 \end{bmatrix} \tag{2.19}$$

where the oscillating rf potential provides confinement in the radial ($\hat{x}$ and $\hat{z}$) directions with a curvature of $m\omega_{\text{rf}}^2$, and the static potential provides positive confinement in the axial ($\hat{y}$) direction and may be anti-confining in either of the radial directions.

As long as the pseudopotential curvature is larger than all the anti-confining force from the static potential, then the ion is confined in all three directions. For common trapped-ion quantum computing experiments, the axial frequency is on the order of 100 kHz to 1 MHz and the radial frequencies are typically 5-7 times larger.

The complete Hamiltonian of the ion in a rf Paul trap can now be described as

$$\hat{H} = \frac{\hat{p}^2}{2m} + \frac{1}{2}m\left[\left(\omega_{\text{rf}}^2 + \omega_x^2\right)\hat{x}^2 + \omega_y^2\hat{y}^2 + \left(\omega_{\text{rf}}^2 + \omega_z^2\right)\hat{z}^2\right] \tag{2.20}$$

2.1.1 Surface Electrode Trap

One can imagine taking the quadrupole ion trap we analyzed in the previous section and unfolding the electrodes onto a single plane (Fig 2-2). Ions are still trapped in the radial directions by the rf potential and are localized near the rf null, which is now approximately tens-to-hundreds of microns above the trap surface.

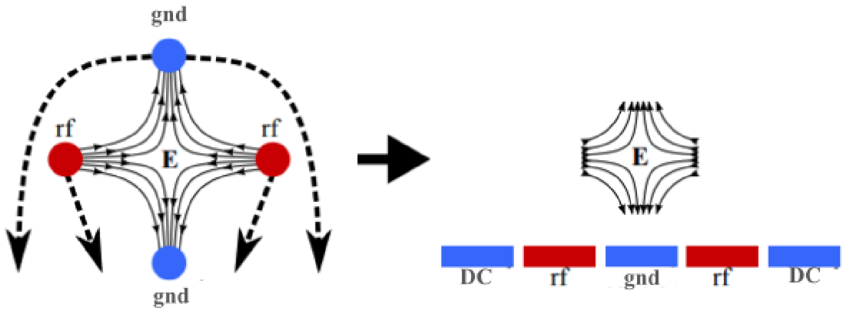

Figure 2-2: A schematic of the quadrupole trap being unfolded into a surface trap, adapted from [4]. The rf null is now above the plane of the trap. The rf ground electrodes can be segmented along the axial direction (into the page).

Surface Paul traps behave with the same physics as quadrupole Paul traps, but due to their broken symmetry, there is no longer a clean analytical derivation for the radio-frequency potential analogous to (2.4). For the plethora of possible surface electrode shapes and configurations, it is generally quite difficult to analytically solve for the resulting electric potential. Therefore it is convenient and accurate to use well-developed numerical simulations and boundary element methods as will be explained more in section 3.1.

Despite lacking an analytical description, there are many advantages to using a surface trap architecture with segmented electrodes. The core advantage is the ability to fabricate surface traps with state-of-the-art lithographic techniques. This has drastically improved scalability of ion traps because manufacturing with industrial lithographic processes and CMOS foundries is highly repeatable and has been well developed for the world's electronics. Another advantage of surface traps is that they have a smaller form factor, allowing for complex and customized electrode geometries. It is much easier for an ion trapper to fabricate an electrode array of trapping sites that could be used for parallel quantum operations using a surface trap architecture. Finally, there is ongoing work to integrate optical and electronic devices directly on-chip, with the hopes of matching the technology requirements to control more ion qubits [70, 68].

While surface electrode traps opens the door for new engineering innovations, there are some technical challenges worth mentioning here. The first is that the trap depth (how much energy an ion can gain before breaking out of the trap) of surface architectures are generally lower than 3D ion traps. This means that ions are more susceptible to background gas collisions and external noise sources[2]. Furthermore, compared to 3D quadrupole traps, the validity of the pseudopotential approximation on surface traps breaks down closer to the rf null and there are greater anharmonicities of trapping potentials. The fundamental reason for lower trap depths and greater anharmonicities is due to the fact that electrodes in a surface trap are constrained to lie in a single plane. These challenges are not deal-breakers, however, and can often be accounted for with careful simulations of trapped-ion experiments on surface traps.

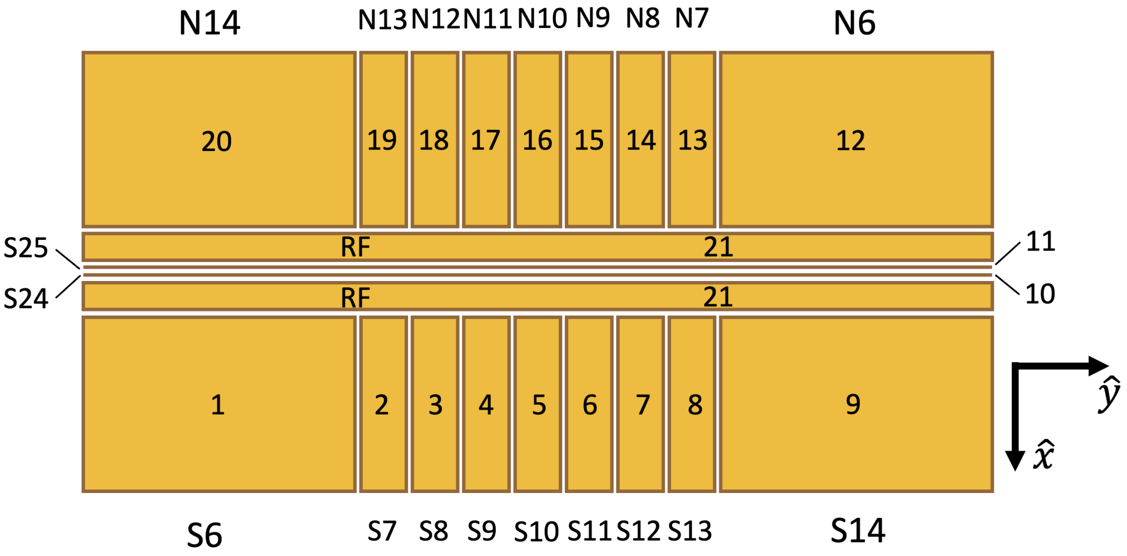

Figure 2-3: An diagram of the Standard Lincoln Trap. Each electrode has a name and corresponding number. The pitch of the DC electrodes 2–8, and 13–19 is 120 μm. Electrodes 10 and 11 serve to finely adjust the orientation of the ion's principle directions. $\hat{y}$ is the axial direction.

The DC electrodes of surface traps can be "inner segmented", meaning they lie between the rf electrodes, or "outer segmented", they lie outside the rf electrodes.

---

[2] although placing the trap in a cryogenic environment and high vacuum helps reduce ion heating

The Standard Lincoln Trap, shown in Fig 2-3, is an outer segmented trap, while the MaxBeta Trap, Fig 2-4, is an inner segmented trap. Ions are located closer to the DC electrodes on inner segmented traps, which means they are more sensitive to voltages applied on the electrodes. While this allows for large axial trapping potentials, the ions may be more sensitive to electric field noise. The MaxBeta Trap was optimally designed to be able to produce a large quartic confinement, which I will show to be useful for splitting ion chains [50].

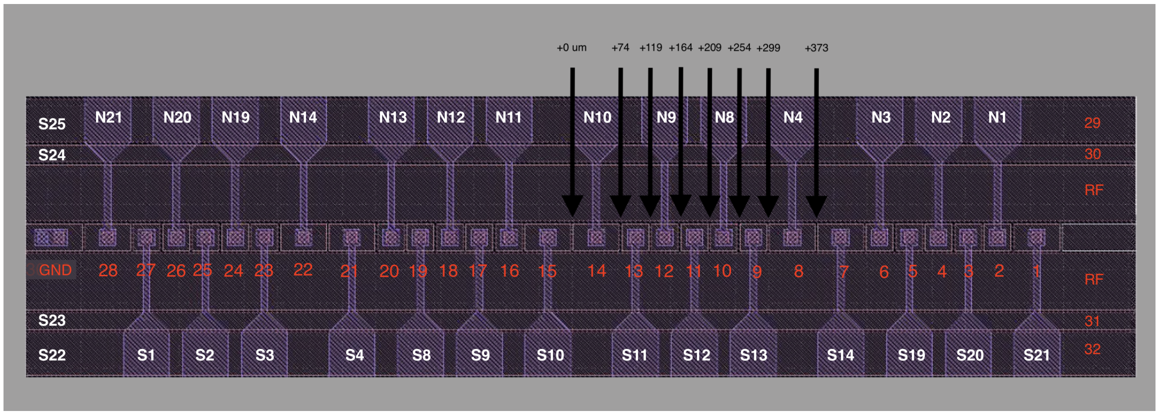
+0 um
+74
+119
+164
+209
+254
+299
+373
S25
N21
N20
N19
N14
N13
N12
N11
N10
N9
N8
N4
N3
N2
N1
29
S24
30
RF
GND
28 27 26 25 24 23 22 21 20 19 18 17 16 15 14 13 12 11 10 9 8 7 6 5 4 3 2 1
RF
S23
31
S22
S1
S2
S3
S4
S8
S9
S10
S11
S12
S13
S14
S19
S20
S21
32

Figure 2-4: A diagram of the MaxBeta trap. Same coordinate system as the SLT 2-3. Position $y = 0$ μm is right between electrodes S10 and N10. 45 μm pitch on the smaller electrodes, and 74 μm on the larger electrodes. The rf electrodes lie on the outside of the DC electrodes. Electrodes S22, S23, S24, S25 serve to tilt the ion's principle directions.

2.2 Motional Dynamics

We see from (2.6) in the previous section that the motion of an ion in a rf Paul trap can be split into two components: a small amplitude, fast oscillation at the rf frequency (known as micromotion), and a larger amplitude, slow oscillation resulting from time-averaging the rf potential (known as secular motion).

2.2.1 Micromotion

Let us briefly discuss micromotion, which can often be neglected in most trapped-ion quantum computing experiments, because it is in best interest of experimentalists to calibrate the trap to minimize the ion's micromotion. This process of micromotion compensation requires a precise cancellation of any stray fields that can force the ions away from the rf null [3]. The amplitude of the ion's micromotion grows with the distance away from the rf null. As the micromotion amplitude grows, the pseudopotential approximation breaks down, since the ion no longer experiences a spatially-constant force during a rf period. If the amplitude continues to grow, the ion will no longer satisfy the stability criteria predicted from the Mathieu equation, and can escape the trap. Thus, it is advantageous to compensate for micromotion at the start of any trapped-ion operation.

2.2.2 Secular Motion

When micromotion is well compensated, the resulting secular motion essentially behaves as a standard quantum harmonic oscillator, with angular frequencies given by the curvature in (2.19). The following form for a harmonic oscillator Hamiltonian and energy spectrum is very well known,

$$\hat{H} = \sum_i \left(\frac{\hat{p}_i^2}{2m} + \frac{1}{2} m\omega_i^2 \hat{q}_i^2 \right), \qquad E_n = \hbar\omega \left(n + \frac{1}{2} \right) \tag{2.21}$$

where n an integer representing number of excited states above the ground state. Since the energy spectrum is an equally-spaced ladder with separation $\hbar\omega$, we can conveniently work with the quantum states corresponding to each rung, $|n\rangle$. These set of states form a complete basis for the harmonic oscillator Hamiltonian and are known as Fock states.

We can introduce creation and annihilation operators that step from one Fock state to the next,

$$\hat{a} = \sqrt{\frac{m\omega}{2\hbar}} \left(\hat{q} + \frac{i}{m\omega} \hat{p} \right), \qquad \hat{a}^\dagger = \sqrt{\frac{m\omega}{2\hbar}} \left(\hat{q} - \frac{i}{m\omega} \hat{p} \right) \tag{2.22}$$

which act on the Fock basis in the following way,

$$\hat{a}\,|n\rangle = \sqrt{n}\,|n-1\rangle\,, \quad \hat{a}^\dagger\,|n\rangle = \sqrt{n+1}\,|n+1\rangle\,, \quad \hat{a}\,|0\rangle = 0 \tag{2.23}$$

There are a few states beyond the Fock state that are worth mentioning. The first is a coherent state. These states arise when the ground-state harmonic oscillator wavefunction is displaced from the trap minimum, described by the following displacement operator,

$$\hat{D}(\alpha) = \exp\left(\alpha\hat{a}^\dagger - \alpha^*\hat{a}\right), \qquad |\alpha\rangle = \hat{D}(\alpha)\,|n=0\rangle \tag{2.24}$$

where α is a complex number representing the location of the coherent state $|\alpha\rangle$ in (q, p)-phase space.

A coherent state is said to be most similar to a classical state because the position and momentum expectation values evolve as a classical particle would under a harmonic oscillator with frequency ω. We can thus describe the quantum dynamics of coherent states using the simpler language of classical mechanics. A coherent state is a delicate balance of Fock states, however, and the probability of measuring a coherent state in any single Fock state, $P_n = |\langle n|\alpha\rangle|^2$, is given by a Poisson distribution with mean value $\bar{n} = |\alpha|^2$,

$$\boxed{|\alpha\rangle = \sum_n \frac{\alpha^n}{\sqrt{n!}} e^{-|\alpha|^2/2}\,|n\rangle\,, \qquad P_n = \frac{|\alpha|^{2n}}{n!} e^{-|\alpha|^2} \qquad (2.25)}$$

The second state worth mentioning is a thermal state, which is an incoherent distribution of Fock states. An ion tends to fall into a thermal state after many random excitations from various noise sources; in other words the ion "heats up". We can say the ion is in equilibrium with a thermal reservoir at temperature T and will follow a Boltzmann distribution over the Fock states,

$$P_n = \frac{e^{-\beta E_n}}{Z} = \frac{e^{-\beta\hbar\omega\left(n+\frac{1}{2}\right)}}{Z} \tag{2.26}$$

where $\beta = 1/k_B T$, k_B is the Boltzmann constant, and Z is the partition function over all Fock states:

$$Z = \sum_{n=0}^{\infty} e^{-\beta\hbar\omega\left(n+\frac{1}{2}\right)} = \frac{e^{-\beta\hbar\omega/2}}{1 - e^{-\beta\hbar\omega}} \tag{2.27}$$

which simplifies (2.26) to,

$$P_n = e^{-\beta\hbar\omega n}\left(1 - e^{-\beta\hbar\omega}\right) = \frac{\bar{n}^n}{(\bar{n}+1)^{n+1}} \tag{2.28}$$

where $\bar{n}$ is the average number state given by,

$$\bar{n} = \sum_{n=0}^{\infty} nP_n = \frac{1}{e^{\beta\hbar\omega} - 1} \tag{2.29}$$

Finally, squeezed states are also interesting quantum states that have a variance of one variable reduced below the Heisenberg uncertainty limit, while the variance of the conjugate variable is expanded. I will not be using squeezed states in this thesis but they are being investigated in the context of continuous variable quantum computing with trapped-ions [45].

2.2.3 Normal Modes

So far we have only considered the dynamics of a single ion in an externally applied potential. To analyze a chain of N-ions in a Paul trap, we must also take into account their Coulomb interactions with all the other ions in the chain. For the j-th ion in the chain, we can write the Hamiltonian as follows,

$$\hat{H}_j = \frac{p_j^2}{2m_j} + \Phi_{\text{tot}}(\vec{r}_j) + \frac{1}{4\pi\epsilon_0}\sum_{i\neq j}\frac{q_i q_j}{|\vec{r}_i - \vec{r}_j|} \tag{2.30}$$

where Φ_{tot} is the sum of static and pseudopotentials in the Paul trap (2.18). This gives us a new effective potential for each ion that includes all $N-1$ Coulomb interactions,

$$\Phi_{\text{eff}}^{(j)} = \Phi_{\text{tot}}(\vec{r}_j) + \frac{1}{4\pi\epsilon_0}\sum_{i\neq j}\frac{q_i q_j}{|\vec{r}_i - \vec{r}_j|} \tag{2.31}$$

Analytically solving for all N Hamiltonians is quite difficult but we can work in the limit of small oscillations around the chain equilibrium. In this limit, all N ions are close to their effective potential minimum. The gradient of effective potential on each ion vanishes and the effective potential is approximately harmonic, allowing us to define our Hessian curvature matrix as we did in (2.19), except this time $\mathcal{H}$ is a $3N \times 3N$ matrix. If N is large, we might be inclined to numerically determine each effective potential, $\Phi_{\text{eff}}^{(j)}$, populate the Hessian matrix, and numerically find the eigenvalues and eigenvectors.

For N ions, there will be N modes in each principal direction for a total of $N_{\text{mode}} = 3N$ modes. Note that we are free to analyze each principal direction individually, with the axial mode being the simplest choice because ion crystals are usually linear in the axial direction. For two identical ions, the two axial modes are typically called the "COM" and "stretch" modes. In an axial harmonic potential with frequency ω_0, the two mode frequencies are $\omega_{\text{COM}} = \omega_0$ and $\omega_{\text{str}} = \sqrt{3}\omega_0$. Analytical calculation for longer ion chains become more intense, but has been done for a three-ion mixed-species chain [11]. In general, numerical simulations are significantly simpler.

2.3 Electrical Controls

The electrical control system provides proper voltages to our electrodes and consists of a combination of custom-built electronics and commercially available hardware.

Voltages applied to the DC electrodes provide the electrostatic confinement in the axial direction. The Advanced Real-Time Infrastructure for Quantum physics (ARTIQ) hardware system developed by M-Labs provide the gate control signals to our digital-to-analog converters (DACs). Currently, our system runs M-Labs's Sinara 5632 DAC, affectionately named "Fastino", which has 32 16-bit channels with an update rate of 2Mbps. The Fastino outputs a voltage range of ±10 V, with a settling time of 1 μs, and a slew rate of 17 V/μs.

The next stage after the Fastino is a custom-built high-voltage amplifier with a DC gain of 4 and a cutoff frequency around 1 MHz with a roll-off of around 27 dB per decade[3]. The high-voltage amplifier is designed around the LTC6090-5 op-amp which has a 21 V/μs slew rate.

After the x4 amplification, the voltage signals are sent through two low-pass filter stages. We low-pass filter our control electronics to avoid high frequency electrical noise that can induce motional excitation to the ion. A recent standard for an acceptable noise level at the ion's secular frequency is less than 1 nV/$\sqrt{\text{Hz}}$ [68]. The first stage is a third-order Butterworth PI filter with a cutoff frequency of 100 kHz. The second stage occurs after routing to an Octagon board and is a simple RC filter with a cutoff of 89 kHz.

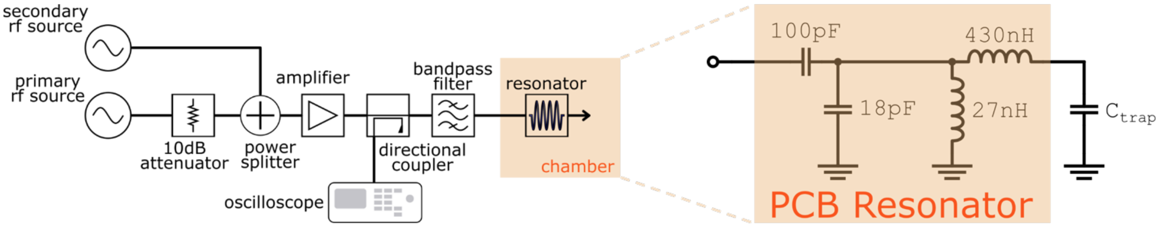
secondary
rf source
primary
rf source
10dB
attenuator
power
splitter
amplifier
directional
coupler
bandpass
filter
oscilloscope
resonator
chamber
100pF
430nH
18pF
27nH
C_{trap}
PCB Resonator

Figure 2-5: A schematic of the rf amplification circuitry, created by Mr. Jules Stuart.

The voltage control system to the rf electrodes is shown in Fig 2-5. The rf signal source is provided by a digital synthesizer, which then gets amplified and sent to the rf resonator for large amplification before getting sent to the rf electrodes on the trap. We typically drive our rf electrodes at 50 MHz and 70 V to trap ^{40}Ca ions.

---

[3] designed and sent for manufacturing by Mr. Jules Stuart

Chapter 3

Numerical Simulation Pipeline

We model each step of an ion shuttling experiment using numerical simulation tools written in Python and SPICE [48].

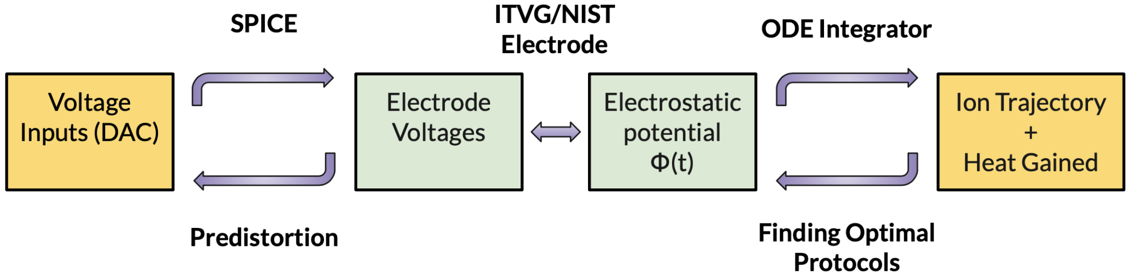
SPICE
ITVG/NIST
Electrode
ODE Integrator
Voltage
Inputs (DAC)
Electrode
Voltages
Electrostatic
potential
Φ(t)
Ion Trajectory
+
Heat Gained
Predistortion
Finding Optimal
Protocols

Figure 3-1: An diagram of the ion motion experiment process. The gold boxes denote the input and output of our system. We care about finding the best voltage inputs to shuttle ions optimally.

The boxes in Fig 3-1 denote the physical steps of shuttling ions while the arrows denote our software tools to model each stage. Our electrode controls start with our input digital-to-analog converters (DACs), which gets low pass filtered and amplified by our electrode circuitry, resulting in an electrode voltage response. We simulate this response using an integration software package LT-Spice. The electrode voltages on our surface trap then generates an electrostatic potential the depends on the size and shape of each electrode. We use our custom written potential solver called Ion Trap Voltage Generation (ITVG) to solve for 3D potential from electrode voltages and vice versa. Finally, I have written an differential equation solver using the Python packages NumPy and SciPy that can solve for the ion's dynamics in a time-dependent electric potential [24, 74].

3.1 Modelling the Surface Electrode Trap

A crucial component to simulating the time-dependent 3D potentials on an surface electrode trap is creating an accurate model of the trap electrodes. Typically, one is interested in the unit potentials of each electrode—in other words, what is resulting 3D electric potential after applying 1V to a single electrode while grounding all the other electrodes? Because our ion traps have length scales of hundreds of microns to millimeters and there are a finite number of electrodes, it is convenient to discretize the electrostatic unit potential $\tilde{\phi}_i(\vec{r})$ into a 3D grid, which we save as a "grid file".

There are multiple methods to accurately simulate these grid files, including proprietary multiphysics software such as COMSOL, boundary element methods, and the Biot-Savart law for electrostatics [71]. These methods do indeed lead to comparable unit potentials if done carefully. Mr. Jules Stuart used finite element methods in COMSOL to simulate the grid files for both the Standard Lincoln Trap and the MaxBeta trap, which have been depicted in 2-3, 2-4. I should note that the process of solving for unit potentials, $\tilde{\phi}_i(\vec{r})$, on the DC electrodes must also be extended to the rf electrodes, $\tilde{\phi_{\text{rf}}}(\vec{r})$, because the geometry of surface traps no longer allow a clean analytical solution for the rf potential (2.4).

The rf potential now is the product of the rf voltage and the rf unit potential,

$$\Phi_{\text{rf}}(\vec{r},t) = V_{\text{rf}}\ \tilde{\phi_{\text{rf}}}(\vec{r}) \tag{3.1}$$

Apply the pseudopotential approximation for a general rf potential (2.15) leads to the following rf pseudopotential,

$$\Phi_{\text{ps}}(\vec{r}) = \frac{q}{4m\Omega_{\text{rf}}^2}\left(V_{\text{rf}}\ \nabla\tilde{\phi_{\text{rf}}}(\vec{r})\right)^2 \tag{3.2}$$

Once all the trap electrode grid files have been created, solving for the total applied potential is simply a superposition of the static electrode grid files plus the pseudopotential from the rf electrode grid file (3.2),

$$\Phi_{\text{tot}}(\vec{r},t) = \sum_{i}^{N} V_i(t)\ \tilde{\varphi}_i(\vec{r}) + \Phi_{\text{ps}}(\vec{r}) \tag{3.3}$$

where $V_i(t)$ is the voltage on the i-th electrode, and N total DC electrodes.

Note that the time dependence of our total applied potential (3.3) comes not from the rf electrodes, but from the changing voltages applied to the DC electrodes. The set of electrode voltages $V_i(t)$ are called "waveforms" and they must be delicately choreographed to perform optimal ion shuttling operations.

3.2 Solving for Voltage Waveforms

In ion shuttling experiments, we typically start with a carefully designed electrostatic potential $\Phi_{\text{tot}}(\vec{r},t)$[1] and work backwards to solve for suitable electrode waveforms $V_i(t)$ to achieve such a potential. The process of solving for N waveforms from a single target potential is an ill-posed inverse problem as there is no guarantee of a unique optimal solution. To narrow down this inverse problem one can add constraints and assumptions, in a process called regularization, to reflect what we observe experimentally, such as electrode voltage bounds and waveform smoothness.

We can formulate the constraints and degrees of freedom into the language of matrices. It is convenient to define a voltage vector and unit potential vector as such,

---

[1] Techniques for designing optimal shuttling protocols will be discussed in chapter 4

$$\boldsymbol{V}^{\mathrm{T}} \equiv \begin{bmatrix} V_1(t) & V_2(t) & \dots & V_N(t) \end{bmatrix} \tag{3.4}$$

$$\boldsymbol{\phi}^{\mathrm{T}} \equiv \begin{bmatrix} \tilde{\phi_1}(\vec{r}) & \tilde{\phi_2}(\vec{r}) & \dots & \tilde{\phi_N}(\vec{r}) \end{bmatrix} \tag{3.5}$$

It follows that the electrostatic part of the total applied potential is the dot product of our voltage and unit potential vectors

$$\Phi_{\mathrm{st}}(\vec{r}, t) = \boldsymbol{\phi}^{\mathrm{T}} \cdot \boldsymbol{V} \tag{3.6}$$

$\boldsymbol{\phi}$ is well known from our trap electrode simulations but it is difficult to solve for voltages $\boldsymbol{V}$ as (3.6) is currently underdetermined—there is one target potential $\Phi_{\mathrm{tot}}(\vec{r}, t)$ but N degrees of freedom in $\boldsymbol{V}$. To better constrain our inverse problem, we may Taylor expand our desired electric potential around some defined expansion point, $\vec{r}_0$. While we can expand the applied potential at any point near the trap, it is convenient to do so at the rf null.

Once we have chosen a suitable expansion point, we may begin writing down the Taylor coefficients of our target potential Φ_{tot}. Let us declare, without loss of generality, that our expansion point is also the location of the confined ion. In this case, the ion should experience zero electric force and the three first derivatives of our potential, Φ_{tot}, should be zero,

$$\nabla \Phi_{\mathrm{tot}}(\vec{r}_0) \doteq 0 \tag{3.7}$$

where we have used $\doteq$ to denote a constrained equality, rather that a natural equality resulting from physics.

Next, we may constrain the nine second derivatives of the Hessian matrix (2.18). However, only six of those constrains are independent because the second derivatives of the potential commute (i.e. $\frac{\partial^2}{\partial x \partial y} = \frac{\partial^2}{\partial y \partial x}$). Since the Hessian matrix is populated with second derivatives of $\hat{x}$, $\hat{y}$, and $\hat{z}$, there is an implicit coordinate system defined in which to evaluate these derivatives. If one chooses to constrain the off-diagonal derivatives to be zero, as such,

$$\mathcal{H}(\vec{r}_0) \doteq m \begin{bmatrix} \tilde{\omega}_x^2 & 0 & 0 \\ 0 & \tilde{\omega}_y^2 & 0 \\ 0 & 0 & \tilde{\omega}_z^2 \end{bmatrix} \tag{3.8}$$

then the principle axes that confine the ion are aligned with the coordinate system of the Hessian.

If one wanted to confine the ion along different principle axes (e.g. to rotate the ion's radial directions by some defined tilt angle), they may simply constrain the off-diagonal derivatives to the proper non-zero value. The Hessian matrix can always be diagonalized to find the curvatures (eigenvalues) and principle axes (eigenvectors).

Higher order derivatives of the potential can also be constrained[2], and in general the only limit to the number of constraints is the number of degrees of freedom in our system, which is set by the number of electrodes whose voltages we can vary. In order to conveniently formulate all these derivatives into a single, $k \times 1$, constraint vector, $\boldsymbol{C}$, we must introduce an operator to take the derivatives we want to constrain,

$$\mathcal{P}^{\mathrm{T}} \equiv \begin{bmatrix} \frac{\partial}{\partial x} & \frac{\partial}{\partial y} & \frac{\partial}{\partial z} & \frac{\partial^2}{\partial x^2} & \frac{\partial^2}{\partial x \partial y} & \frac{\partial^2}{\partial x \partial z} & \frac{\partial^2}{\partial y^2} & \frac{\partial^2}{\partial y \partial z} & \frac{\partial^2}{\partial z^2} & \dots \end{bmatrix} \tag{3.9}$$

where $\mathcal{P}$ is a $k \times 1$ vector, and k represents the number of desired constraints. To get the contribution of every electrode potential to each constraint, we must apply the derivatives in $\mathcal{P}$ (3.9) to the unit potentials (3.5) and multiply by the electrode voltage (3.4). Our constrain vector is the sum of all electrode contributions for each derivative constraint. We can formalize this using the following outer product with our unit potential vector (3.5),

---

[2] it will be advantageous to do so in the case of splitting, as we shall see in 4.2

$$\mathcal{P} \otimes \boldsymbol{\phi}^{\mathrm{T}}(\vec{r}_0) = \begin{bmatrix} \frac{\partial \tilde{\phi}_1(\vec{r}_0)}{\partial x} & \frac{\partial \tilde{\phi}_2(\vec{r}_0)}{\partial x} & \cdots \\ \frac{\partial \tilde{\phi}_1(\vec{r}_0)}{\partial y} & \frac{\partial \tilde{\phi}_1(\vec{r}_0)}{\partial y} & \cdots \\ \vdots & \vdots & \ddots \end{bmatrix} \tag{3.10}$$

where the tensor product leads to a $k \times N$ matrix and all derivatives are evaluated at the expansion point, $\vec{r}_0$.

Finally, our constraint vector is the sum of all the derivative contributions from the DC electrodes *and* the rf electrodes (3.2),

$$\left(\mathcal{P} \otimes \boldsymbol{\phi}^{\mathrm{T}}(\vec{r}_0)\right) \cdot \boldsymbol{V} + \mathcal{P}\Phi_{\mathrm{ps}}(\vec{r}_0) = \boldsymbol{C} \tag{3.11}$$

Equation (3.11) is the ultimate formalism of the inverse problem. $\mathcal{P}$, $\boldsymbol{\phi}^{\mathrm{T}}$, and Φ_{ps} are well known, and $\boldsymbol{C}$ is defined by the experimentalist to according to their desired target potential, $\Phi_{\mathrm{tot}}(\vec{r}, t)$. We must now invert the problem to solve for the waveforms $\boldsymbol{V}$.

There are two closely related methods for solving this formulation of the inverse problem: singular value decomposition (SVD) and linear least-squares optimization (LLS). While the SVD method applied on a perfectly-matched problem (number of constraints equals the degrees of freedom) may result in voltage sets that exactly achieve the target potential, additional constraints such as voltage limits are unable to be included.

While SVD attempts to be an exact process, it can easily be "poorly conditioned". LLS seeks to find a locally optimum $\boldsymbol{V}$ that minimizes the error in $\boldsymbol{C}$. Because this method is attempting to minimize a cost function, LLS allows the user to add constraints that are more practical rather than necessitated by physics, but can greatly improve the resulting waveforms. Such extra constraints includes voltages stay within a specified bound (we are limited to ±40 V by our electronics), voltages vary smoothly for nearby trapping positions, voltages are not extraneously large, and a weighting factor to bring out the importance of select constraints (e.g. axial frequency ω_y). Although we are usually guaranteed to get a reasonable voltage set using the LLS method, it is not guaranteed that the voltage set is the globally optimal set to achieve the target potential. It may be a locally optimal set given the constraints we have decided to implement in our cost function. Therefore it is important to run simulations of the waveforms through the rest of my numerical pipeline to understand the errors in the resulting potential Φ_{tot}.

With all these considerations LLS has been the preferred voltage solving method in this thesis.

3.2.1 Ion Trap Voltage Generation

The formulation above is implemented numerically in Python in our Ion Trap Voltage Generation (ITVG) script. At its very core, ITVG maps between electrode voltages and electrostatic potential in both the forwards ($\boldsymbol{V} \mapsto \Phi_{\text{tot}}$) direction according to (3.3), and backwards ($\Phi_{\text{tot}} \mapsto \boldsymbol{V}$) direction according to (3.11).

3.2.1.1 Calculating Potentials

In the forwards direction, one can simply superpose electrode voltages with unit potentials according to (3.3) to obtain the full electrostatic potential in position space. It is worth noting however that the resolution of the electrostatic potential is limited by the resolution of the system's grid files since we can calculate the full potential only at the positions that we've modeled the electrode potentials. Usually the electrostatic potential does not vary faster than the grid file resolution so it is safe to spline interpolate between the calculated positions.

A second method of calculating the full potential in the forwards direction is to use the coefficient formalism (3.11) but solve for $\boldsymbol{C}$ given $\boldsymbol{V}$, rather than inverting the problem[3]. Often times in ion shuttling experiments, one prefers to describe the full potential by the trajectory of a selected subset of coefficients in

---

[3] I call this the "forward ITVG" method

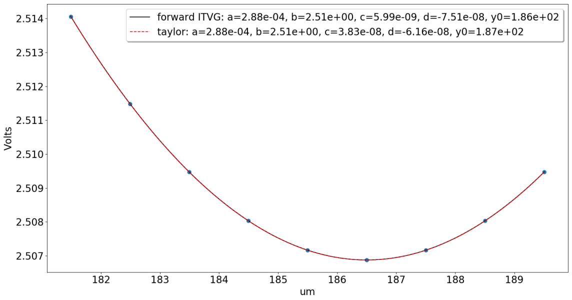

Figure 3-2: A harmonic potential on the MaxBeta trap at 186.5 μm. Grid file resolution is 1 μm. A quadratic potential is taylor fitted (red) on the potential calculated with superposition (blue dots). The potential is also calculated through coefficient expansion, with great agreement.

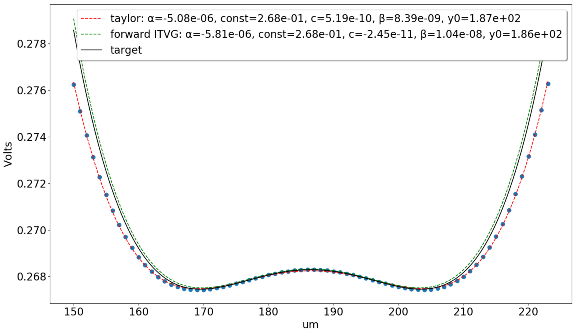

Figure 3-3: A double well potential centered at 186.5 μm. The superposed potential (blue dots) and coefficient expansion potential (dashed green) differ further from the expansion point. The coefficients from forward ITVG and taylor fitting the superposed potential (dashed red) differ by 12%.

parameter space[4]. Thus this method has the advantage of directly solving for potential coefficients and allows one to avoid numerical interpolation.

However this coefficient expansion method also has a disadvantage of being sensitive to the expansion point. Taylor expansions work well locally to a given point but becomes less accurate further out. This usually is not an issue with harmonic potentials, where the ion are located near the potential minimum, but becomes a consideration with anharmonic potentials such as those used in splitting ion chains. The splitting potential shown in Fig 1-4 can be described by a fourth order potential at the center of the ion chain. As the potential becomes a double well and the ions are split apart, the accuracy of the Taylor expansion suffers and the ions can experience a potential that is different from our simulation.

We can compare these two potential solving methods for a single harmonic well and a quartic, double well configuration shown in Figs 3-2, 3-3. For both potentials, the expansion point for the coefficient potential solver was at an axial position $y = 186.5$ μm. In the single harmonic potential 3-2, the discretized potential and the coefficient expansion potential are equivalent. In the double well potential 3-3, the agreement is strong near the expansion point but starts to fall off around 15 μm away.

---

[4] The trajectories of potential coefficients are typically referred to as a "protocol" or "profile"

Choosing between these two potential solving methods make no difference when calculating transport potentials because purely harmonic potentials can be expanded at the potential minimum, where the ions are localized. However, this choice will have an impact on calculating splitting potentials. As ions in a double well configuration become more separated from the expansion point, the coefficients from forward ITVG become less accurate in describing the potential near the actual positions of the ion. To more accurately solve for the electric potential during a split, I recommend using the superposition method and spline interpolating between the points of calculated potential.

3.2.1.2 Calculating Voltages

For the backwards problem, ITVG uses linear least-squares optimization to solve the inverse matrix equation (3.11). More specifically, ITVG implements a Sequential Least Squares Programming (SLSQP) algorithm written in SciPy [34]. There are two main considerations when solving for voltages, which are especially important for shuttling waveforms that should be smooth throughout the trap: hyperparameters and heuristics.

Hyperparameters are additional, tunable inputs to improve the performance of the optimization cycle. A summary of hyperparameters and their functions can be seen in Table 3.1. All the hyperaparameters and heuristics in this section are implemented specifically in ITVG.

Since the inverse problem of determining voltages is ill-posed, there may be multiple voltage sets that generate an equally desirable potential. If the optimizer has a difficult time choosing between these degenerate solutions, the resulting waveform may look like it is jumping between two possible solution sets, shown in 3-4. I have found that the `eps` and `ftol` values have a large effect on resulting waveforms. Decreasing `eps` allows for a finer search in voltage space. SLSQP sequentially changes each component of $\boldsymbol{V}$ by the `eps` value and evaluates the

Name	Typical Value	Function
`eps`	1×10^{-12}	Step size used for numerical approximation of the Jacobian.
`ftol`	1×10^{-27}	Precision goal for the value of f in the stopping criterion.
`bounds`	±40	Search space bounds (limited by our system's voltage range).
`norm`	`np.ones(k)`	A weighting vector for the k constraints.
`fit_range`	$(5, 10, 5) \cdot 1\times10^{-6}$	(x, y, z) range for calculating the potential coefficients.

Table 3.1: A summary of hyperparameters for voltage solving.

resulting cost function to determine gradients using finite differences. The gradients of each component are then used to update the voltage $\boldsymbol{V}$ values and the process iterates again. This is a standard practice of gradient descent algorithms. Increasing or decreasing the `ftol` parameter by a few orders of magnitude may help choose one degenerate set over the other.

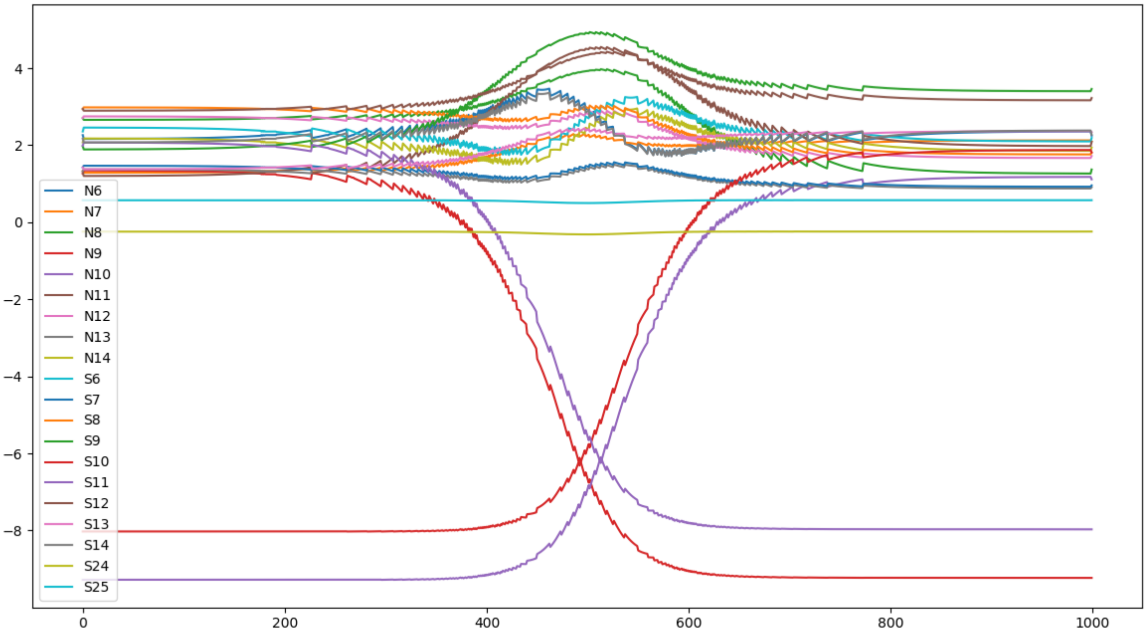

Figure 3-4: Transport waveforms on the SLT. The voltages ocassionally hop between two solution sets that have similar cost function values.

The weighting of constraints, `norm`, is by default a $k \times 1$ unit vector and gets multiplied by the constraint error in the cost function evaluation. We are free to change specific components of the weighting vector to increase or decrease their relative importance. I have found that weighting the axial coefficients $\frac{\partial}{\partial y}$ and $\frac{\partial^2}{\partial y^2}$ by 10 or 100 has helped nail down the axial confinement of the transport potentials.

Finally, ITVG uses a fit range parameter to calculate derivative matrix (3.10). Decreasing this parameter allows for a more accurate potential calculation near the expansion point, while increasing the parameter allows the potential to be less accurate locally, but more accurate over a longer spatial range.

Heuristics are the ways in which we set up our optimization problem. We may choose to initialize the starting point of the SLSQP algorithm with the previously calculated voltage set (by setting `independence` to `True`). This is a decent assumption for shuttling waveforms where we expect electric potentials that are close to each other in space to be created by similar voltages.

For constrained inverse problems, the best performance occurs when we are perfectly constrained the number of constrains is close to the number of degrees of freedom. We have the option of choosing both the constraints on our potentials and the electrodes that will be supplying the potential. I have found the best results from when the number of constraints is equal to or slightly larger than the number of free electrodes (slightly overdetermined regime). We may choose the free electrodes to be the ones closest to the ion's position along the trap.

All these hyperparameters and heuristics require a moderate amount of trial and error to perform. In general solving for waveforms has many approaches and a tight loop to evaluate the resulting waveforms in simulations—or even in experiments if possible—leads to faster feedback and a better understanding of optimal waveforms.

3.3 Electrode Circuit Simulation

Another stage of the simulation pipeline is the simulation of the electrode circuitry, shown as the first leg in Fig 3-1. This stage is essential because the low pass filtering on the ion trap system distorts inputs such that the electrode voltages **V** is no longer what we apply. Our simulation is done in LTSpice using a model for the Fastino and the high-voltage amplifier designed by Mr. Jules Stuart. Our inputs are discrete voltage steps on our DACs, which are modelled as piece-wise linear functions.

It is quite important to be able to invert this filtering process in order to find the proper voltage inputs to achieve a target $\boldsymbol{V}$. The process for this inversion is called "predistortion" and is detailed in chapter 5. Especially with fast input waveforms, it is important to have an accurate model of the filtering amplification in order to confidently predistort voltages. We have collected data to accurately determine our amplifier and filtering system, and will be discussed in section 6.1.

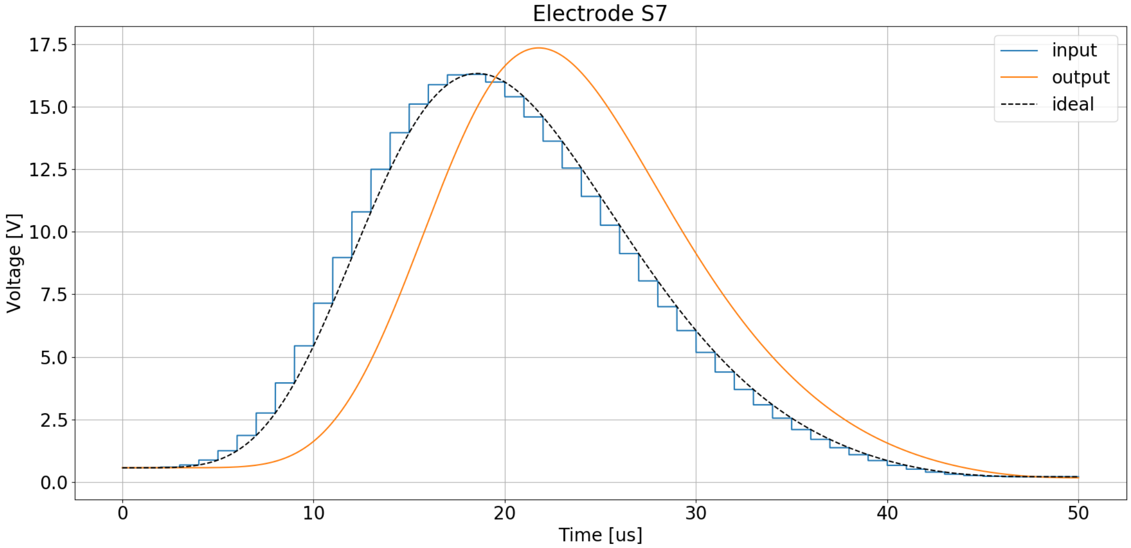

Figure 3-5: An example of a time-domain simulation of electrode filtering with LTSpice. The input signal is shown as piece-wise linear discrete step function (blue). The circuit output is shown in orange. The dashed black line shows a target waveform for this electrode.

3.4 ODE Solver

Finally, the last stage of the simulation pipeline is a classical ion trajectory simulator. I wrote in Python an initial value problem solver that can determine the trajectory of multiple ions in a time-dependent electric potential. This solver uses the Runge-Kutta method of order 5 [17] to integrate the following equation of motion,

$$\ddot{y}_i = \frac{q_i}{m_i}\left[-\frac{\partial}{\partial y}\Phi_{\text{tot}} + \frac{1}{4\pi\epsilon_0}\sum_{j\neq i}\frac{q_j}{|y_j - y_i|^3}(y_j - y_i)\right] \tag{3.12}$$

where y_i, q_i, m_i are the axial position, charge, and mass of the i-th ion, and Φ_{tot} is is given by (3.3). Note that my simulation uses the pseudopotential approximation for Φ_{tot} and does not take into account the radial modes. This means I only solve for the dynamics of the ion's secular motion in the axial direction, an example of which is shown in Fig 3-6.

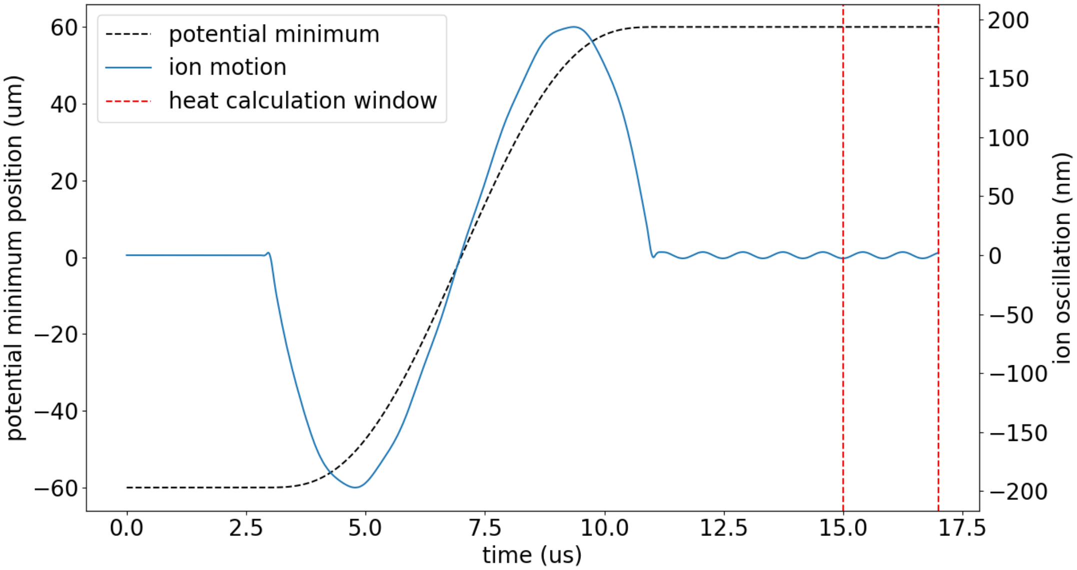

Figure 3-6: Simulation of the trajectory of ^{88}Sr under a harmonic oscillator moving with protocol shown in dashed black. Ion position relative to the potential minimum shown in blue and uses the right-hand y-axis scale. The ion's motion during the "heat calculation window" is used to determine the motional excitation after transport

Also note that this calculation is a classical treatment of the ion's dynamics. It has been accepted throughout literature that the classical and quantum dynamics in time-dependent shuttling Hamiltonians are the same [27, 60]. We care about the motional excitation of the ions after shuttling operations, and thus we can quote the classical energy gained after shuttling by analyzing the ion's oscillation at the end of shuttling,

$$\bar{n}\hbar\omega(T) = \frac{1}{2}m\omega(T)^2 A^2 \tag{3.13}$$

where $\bar{n}$ is the excitation of the ion in the quanta of harmonic oscillator energies, $\omega(T)$ is the axial frequency at the end of transport, and A is the amplitude of oscillation. For shuttling operations on a N-ion chain, there may be N axial modes that are excited. To determine the motional excitation of any single mode, I Fourier transform the ion's ending motion, bandpass filter around the mode frequency, Fourier transform back to the time domain, and apply (3.13) on the resulting mode oscillation.

I actually implement two types of simulation that use different methods for calculating $\Phi_{\text{tot}}(y, t)$. The first method uses a Taylor expansion for $\Phi_{\text{tot}}(y)$, with coefficients that are spline interpolated in time and calculated using "forward ITVG". This assumes an analytical form of $\Phi_{\text{tot}}(y)$. The second method uses $\Phi_{\text{tot}}(y)$ calculated by superpositions of electrode voltages, which I then spline interpolate along the axial direction as well as in time. This method is better suited for handling non-harmonic potentials, like those found in splitting operatinos. Both methods use a central difference formula to calculate $\frac{\partial}{\partial y}\Phi_{\text{tot}}$. My ODE solver allows us to analyze arbitrary potentials, find the dynamics of ion chains of arbitrary length and species, and serve as a baseline for ion motion experiments.

My numerical tools also allow one to calculate dynamics for which analytical solutions are difficult to find. One example is motional dynamics of long ion chains. Analytically calculating the normal modes for N-ions is difficult in general but using numerical integration and Fourier transformations it becomes a breeze. The three mode frequencies in the axial direction have been analytically solved for a linear chain consisting of ^{43}Ca–^{86}Sr–^{43}Ca[5] [11]. The in-phase, stretch, and alternating modes are 1.209×, 2.449×, and 2.818× the frequency of the middle ^{86}Sr ion.

To numerically simulate this system, I calculate the potential curvature needed to keep ^{86}Sr confined at 1 MHz, according to,

---

[5] This choice of ion species was somewhat arbitrary. I wanted to choose a chain not often seen experimentally.

$$\frac{\partial^2}{\partial y^2}\Phi_{\text{tot}} = \alpha = \frac{m\omega_0^2}{2q} \tag{3.14}$$

Once α is determined, I place the three ions in a harmonic potential given by,

$$\Phi_{\text{tot}} = \alpha y^2 \tag{3.15}$$

and minimize the total energy of the three ions to find their equilibrium position. I shift the ions away from the equilibrium position by a few percent and then run my ODE solver. I then Fourier transform the resulting motion, shown in Fig 3-7.

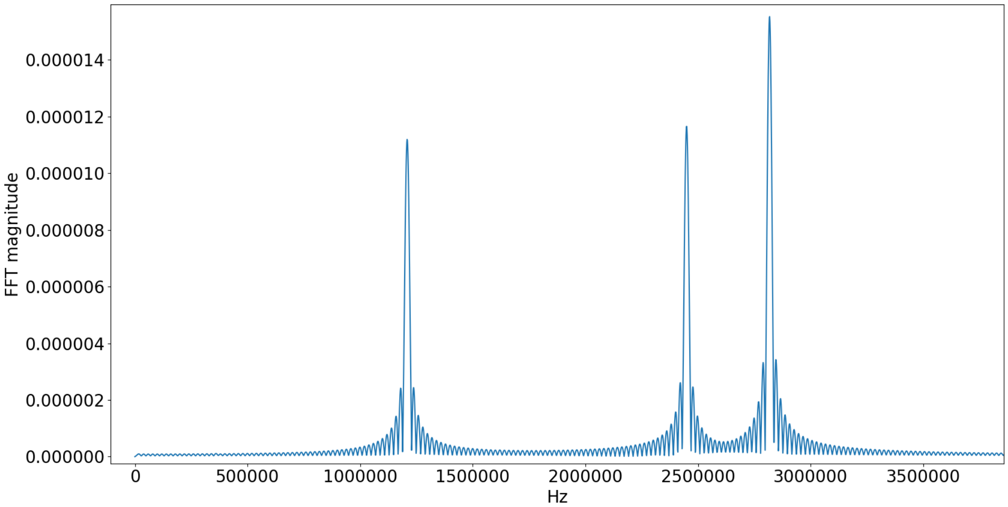

Figure 3-7: An FFT of the ^{43}Ca ion located an a harmonic potential and interacting with a ^{43}Ca and ^{86}Sr ions.

The location of the peaks occur at 1.208 MHz, 2.449 MHz, 2.818 MHz, which is within 1 kHz of the analytically calculated frequencies. While my integration can be painlessly extended to longer ion chains, it is not so obvious how to scale analytical solutions.

Chapter 4

Optimal Ion Shuttling

There are an infinite number of trajectories by which an ion trapper could vary a time-dependent electric field, but in this chapter I present theories to find trajectories that lead to optimal ion shuttling.

In the most basic sense, optimal shuttling operations are fast and cold. Shuttling operations should not excite the motional state of the ion qubit to protect the fidelities of subsequent quantum gates. Operations that add more than a single quanta of motional energy will require laser cooling, which is slow and can destroy the ion's qubit if performed incorrectly. We would like shuttling operations to be as fast as possible, but our speed is limited by the update rate of our voltage input system (2 Mbps). The axial frequency of ions in surface electrode traps is comparable with the frequency of an average digital-to-analog converter ($\sim$1 MHz). Thus, shuttling operations that use a few update rates will lead to times of just a few oscillation periods, well within the diabatic regime of the ion. We can more rigorously declare that optimal shuttling operations are to be performed by a few voltage commands while not exciting the motion of ions.

The theory for optimal ion transport and splitting has been well laid out. However, robustness against electric field noise, electrode filtering, and anharmonic trapping potentials must also be a consideration when implementing optimal shuttling techniques on surface traps.

4.1 Transport Profiles

We now begin designing the transport profiles, $q_0(t)$, introduced earlier (1.1). Although the classical and quantum dynamics of ion motion under certain transport protocols has been well developed, numerical simulations allow for the evaluation and optimization of any arbitrary profile [27, 64, 61]. Without loss of generality we can analyze transport from 0 to d with a transport time of T and thus constrain the ends of transport.

$$q_0(t \leq 0) = 0, \qquad q_0(t \geq T) = d \tag{4.1}$$

Common transport protocols include linear, sinusoidal, hyperbolic tangent, which are formulated in (4.2a), (4.2b), (4.2c) respectively.

$$q_0(t) = d\,\frac{t}{T} \tag{4.2a}$$

$$q_0(t) = \frac{d}{2}\left(1 - \cos\left(\pi \frac{t}{T}\right)\right) \tag{4.2b}$$

$$q_0(t) = \frac{d}{2}\,\frac{\tanh\left(N\,\frac{2t-T}{T} + \tanh N\right)}{\tanh N} \tag{4.2c}$$

where N is a parameter that controls how smooth the beginning and ends of transport are. The larger the N value, the more the acceleration is concentrated in the middle of transport. These profiles are shown in Fig 4-1.

We observe from Fig 4-1 that linear and sinusoidal transport have acceleration kicks at the beginning and end of transport, while most of the acceleration for the hyperbolic tangent transport occurs in the middle. It is possible to take advantage of the acceleration kicks by perfectly timing the transport time such that the ending kick removes the motional excitation incurred from the starting kick. This happens at every odd half-periods of the harmonic trap period,

$$T = \frac{2\pi}{\omega_0}\left(n + \frac{1}{2}\right) \tag{4.3}$$

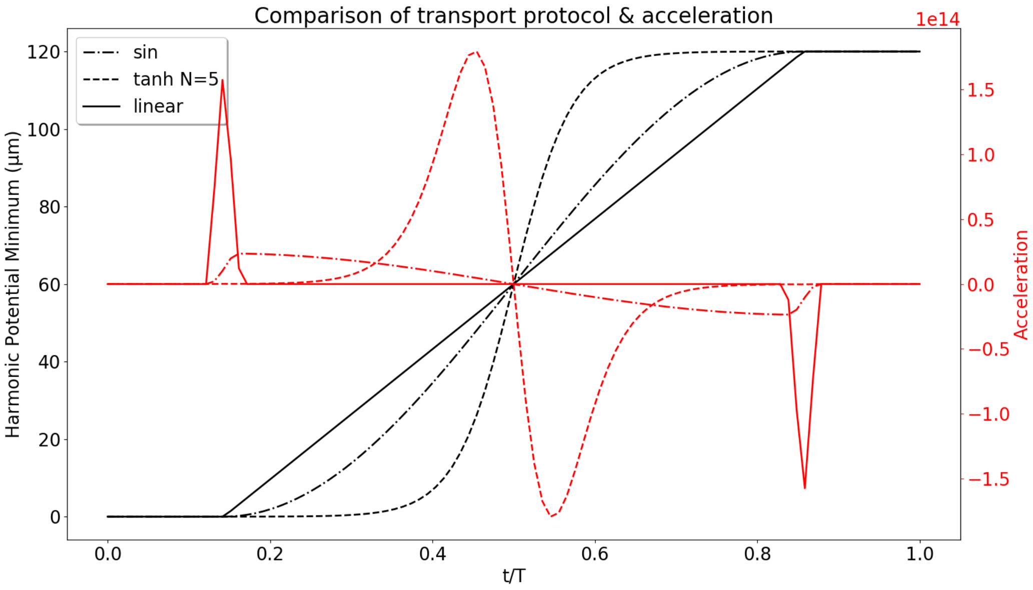

Figure 4-1: Various transport profiles plotted in black. Acceleration determined using numerical derivatives, plotted in red and using the right-hand scale.

where n is a natural number. Indeed, we observe periodic transport times where linear and sinusoidal transport leads to low motional excitation 4-2.

While taking advantage of this "kicking effect" to achieve cold transport on fast timescales has been experimentally demonstrated [76, 32], it requires precision timing on the order of the trap frequency in order to be implemented robustly. As seen in Fig 4-2, missing the timing by half a trap period, which can be on the order of 500 ns, can be disastrous for the ion.

Of the transport profiles detailed above (4.2), the hyperbolic tangent is the only profile thus far that has zero acceleration kicks at the ends of transport. Since the acceleration is smooth throughout transport, tanh reliably reaches a motional excitation below 1 quanta without any dips at the fastest time scales 4-2. This suggests that the smoothness of the acceleration profile is important for achieving cold transport without being overly sensitive to timing.

It is a helpful reminder that while we analyze transport profiles in one dimension, the potential is actually harmonic along the axial direction. We can more concretely visualize the time-dependent potential changes during ion transport

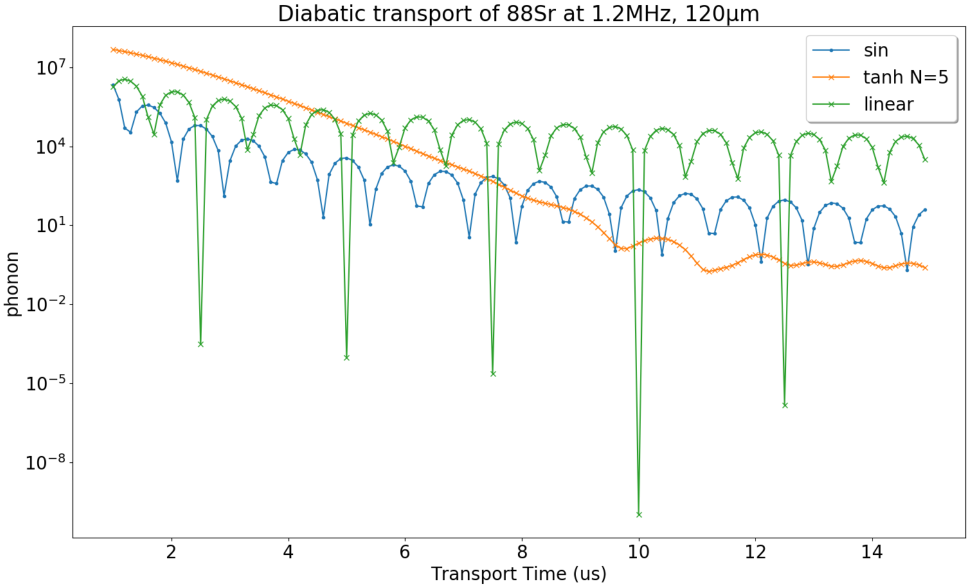

Figure 4-2: Motional excitation calculated by determining the classical energy of the ion's motion at the end of transport. The trajectory of ^{88}Sr in a rigid 1.2 MHz trap under the various transport profiles is calculated with my ODE solver.

by plotting both the time and spatial dependence of the potential in Fig 4-3.

4.1.1 Shortcuts-to-Adiabaticity

Within the past decade, a new formalism has been developed to cleverly control quantum systems and achieve adiabatic dynamics on diabatic timescales [22]. There are a family of techniques that fall under the scope of STA methods to design these special control trajectories. While STA concepts extend beyond the quantum world and into any system with adiabatic regime, there has been extensive literature on applying STA techniques for shuttling ions [56].

One specific technique used for transporting trapped-ions uses Invariant-Based Inverse Engineering, which centers around dynamical invariants of the ion's time-dependent Hamiltonian. The eigenstates of the dynamical invariant are related to the solutions of the Schrödinger equation for time-dependent Hamiltonians [36]. In general, finding solutions to the time-dependent Schrödinger equation (TDSE) may prove to be difficult, whereas finding the eigenstates to dynamical invariants

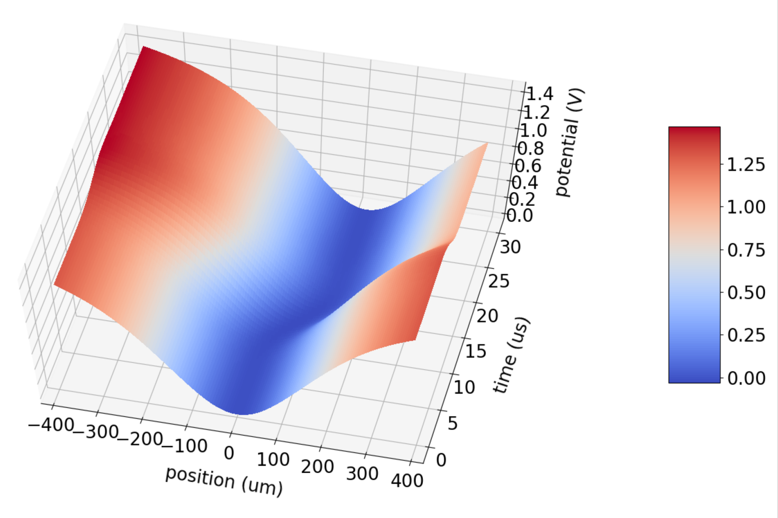

Figure 4-3: A 3D representation of the tanh transport profile. The electric potential (V) is plotted along the z axis. $\hat{y}$-position and time plotted in the x and y axis. This particular transport is from 0 μm to 120 μm.

is a simpler task.

For a time-dependent harmonic oscillator, there exists a well known invariant operator that is quadratic in momentum [37, 16]. This Lewis dynamical invariant has the following form,

$$\hat{I}(t) = \frac{1}{2m}\left[\rho(\hat{p} - m\dot{a} - m\dot{\rho}(\hat{q} - a)\right]^2 + \frac{1}{2}m\omega_0^2\left(\frac{\hat{q}-a}{\rho}\right)^2 + U\left[\frac{\hat{q}-a}{\rho}\right] \tag{4.4}$$

where $\hat{p}$, $\hat{q}$ are the position, momentum operators, U is an arbitrary function of its argument, ρ and a are functions of time, and ω_0 is a constant harmonic frequency. The operator $\hat{I}(t)$ is an invariant for the following general harmonic Hamiltonian in 1D,

$$\hat{H}(t) = \frac{\hat{p}^2}{2m} + V(\hat{q}, t) \tag{4.5}$$

$$V(\hat{q}, t) = -F(t)\hat{q} + \frac{1}{2}m\omega^2(t)\hat{q}^2 + \frac{1}{\rho(t)^2}U\left[\frac{\hat{q} - a(t)}{\rho(t)}\right] \tag{4.6}$$

where ρ, a, ω, and F are function of time that satisfy the following auxiliary equations [37],

$$\ddot{\rho} + \omega^2(t)\rho = \frac{\omega_0^2}{\rho^3} \tag{4.7}$$

$$\ddot{a} + \omega^2(t)a = F(t)/m \tag{4.8}$$

By construction the invariant operator does not change over time, and thus the time-dependent Hamiltonian and corresponding invariant satisfy,

$$\frac{\mathrm{d}\hat{I}(t)}{\mathrm{d}t} \equiv \frac{\partial \hat{I}(t)}{\partial t} + \frac{1}{i\hbar}\left[\hat{I}(t), \hat{H}(t)\right] = 0 \tag{4.9}$$

(4.9) can be combined with Ehrenfest's theorem [23] to derive that the expectation value of the invariant across any solution, $\psi(t)$, of the TDSE remains constant throughout transport,

$$\frac{\mathrm{d}}{\mathrm{d}t}\langle \psi(t)|\hat{I}|\psi(t)\rangle = 0 \tag{4.10}$$

We may choose to expand the time-dependent Hamiltonian wavefunction, $\psi(t)$, in the basis of the eigenstates ψ_n of $\hat{I}$,

$$\psi(\hat{q}, t) = \sum_n c_n \psi_n(\hat{q}, t) \tag{4.11}$$

where c_n are complex coefficients, $\hat{I}\psi_n = \lambda_n \psi_n$, and λ_n are time-independent eigenvalues.

Combining (4.10) and (4.11), we see that the coefficients, c_n, are actually constant in time, which allows us to solve the TDSE using eigenstates of the invariant operator. These eigenstates are well-known and can be easier to solve than the general solution to the TDSE, $\psi(t)$. The eigenstates, ψ_n, have the following form [16],

$$\psi_n(\hat{q},t) = \frac{1}{\sqrt{\rho}}\phi_n\left(\frac{\hat{q}-a}{\rho}\right), \qquad \sigma \equiv \frac{\hat{q}-a}{\rho} \tag{4.12}$$

$$\left[-\frac{\hbar^2}{2m}\frac{\partial^2}{\partial\sigma^2} + \frac{1}{2}m\omega_0^2\sigma^2 + U(\sigma)\right]\phi_n = \lambda_n\phi_n \tag{4.13}$$

where ρ, a, U are the same variables from (4.4), (4.5), (4.6)[1].

Remarkably we have found a relation between wavefunctions of the time-dependent transport Hamiltonian and solutions, ϕ_n of the stationary Schrödinger equation in σ space. While we have the tools to solve general harmonic Hamiltonian problems, most ion transport Hamiltonians are "rigid", meaning that the potential curvature remains constant throughout transport. This simplifies our auxiliary equations considerably.

In the case of rigid transport along a profile, $q_0(t)$, our auxiliary functions become,

$$\omega(t) = \omega_0, \qquad U = 0, \qquad \rho = 1, \qquad F(t) = m\omega_0^2 q_0(t) \tag{4.14}$$

$$\ddot{a} + \omega_0^2(a - q_0(t)) = 0 \tag{4.15}$$

$$\psi_n(\hat{q},t) = \phi_n\left(\hat{q} - a(t)\right), \qquad \lambda_n = E_n = (n + 1/2)\hbar\omega_0 \tag{4.16}$$

where $a(t)$ has remarkably become equivalent to the classical trajectory under Newton's second law in (4.15). Using these values, the transport Hamiltonian (4.5) and dynamical invariant (4.4) of the ion during rigid transport simply reduce to,

$$\hat{H}(t) = \frac{\hat{p}^2}{2m} + \frac{1}{2}m\omega_0^2\left(\hat{q} - q_0(t)\right)^2 \tag{4.17}$$

$$\hat{I}(t) = \frac{\left(\hat{p} - m\dot{a}(t)\right)}{2m} + \frac{1}{2}m\omega_0^2\left(\hat{q} - a(t)\right)^2 \tag{4.18}$$

---

[1] I have chosen to neglect the phase factor of ψ_n in (4.12)

The most straightforward way to ensure that the wavefunction of the transport Hamiltonian at the intial and final times are equal is to have the wavefunction coincide with an eigenvector, ψ_n, of the invariant operator. This is equivalent to ensuring that $\hat{H}(t)$ and $\hat{I}(t)$ commute at the boundary times, $t_b = \{0, T\}$,

$$\left[\hat{H}(t_b), \hat{I}(t_b)\right] = 0 \tag{4.19}$$

From (4.17) and (4.18), we see that commutation is guaranteed when $\dot{a}(t) = 0$ and $a(t) = q_0(t)$. Physically, this means transport with no excitation requires the ion's classical position to coincide with the potential minimum and the ion's classical velocity to be zero at the ends of transport.

A slew of boundary conditions on the ion's classical trajectory may now arise from enforcing commutation. Once the classical trajectory, $a(t)$, has been identified, we use (4.15) to solve for the transport profile, $q_0(t) = \ddot{a}(t)/\omega_0^2 + a(t)$.

$$a(0) = q_0(0) = 0, \qquad \dot{a}(0) = 0, \qquad \ddot{a}(0) = 0 \tag{4.20}$$

$$a(T) = q_0(T) = d, \qquad \dot{a}(T) = 0, \qquad \ddot{a}(T) = 0 \tag{4.21}$$

There are many possible of choices for $a(t)$ and $q_0(t)$ that satisfy these boundary conditions. It is helpful to work with trajectory ansatzes that have some degrees of freedom, such as polynomials, $a(s)/d = \sum_n b_n s^n$, or trigonometric functions, $a(s)/d = c_n \cos \pi n s$, where $s = t/T$ [72, 41, 38].

The following three trajectories are among the STA protocols that I have investigated and can also be found in the following works [54, 51, 38].

$$q_0(t) = d\left[\frac{60s - 180s^2 + 120s^3}{T\omega_0^2} + 10s^3 + 15s^4 + 6s^5\right] \tag{4.22}$$

$$\begin{aligned} q_0(t) = d\Bigg[&\frac{2520s^3 - 12600s^4 + 22680s^5 - 17640s^6 + 5040s^7}{T\omega_0^2} \\ &+ 126s^5 - 420s^6 + 540s^7 - 315s^8 + 70s^9\Bigg] \end{aligned} \tag{4.23}$$

$$\begin{aligned} q_0(t) = d\Bigg[&\frac{1}{2} + \left(-\frac{9}{16} + 2b_3 + 5b_4\right)\cos \pi s \\ &+ \frac{1}{16}\left(1 - 48b_3 - 96b_4\right)\cos 3\pi s \\ &+ b_3 \cos 5\pi s + b_4 \cos 7\pi s\Bigg] \end{aligned} \tag{4.24}$$

where $s = \frac{t}{T}$, $b_3 = -\frac{49(3T^2\omega_0^2 - 25\pi^2)(T^2\omega_0^2 - 25\pi^2)}{6144T^4\omega_0^4}$, $b_4 = \frac{5(3T^2\omega_0^2 - 49\pi^2)(T^2\omega_0^2 - 49\pi)}{6144T^4\omega_0^4}$.

These three protocols (4.22), (4.23), (4.24) are shown in Fig 4-4 and are labeled as "5th order", "9th order", and "trig", respectively. These ansatzes represent only a small fraction of the possible STA trajectories. The freedom to choose STA trajectories allows one to find trajectories that will best be implemented in a surface trap.

One important consideration that can help narrow down the possibilities of STA profiles is robustness. Optimal transport trajectories should also be robust against realistic trap errors, such as variations in trap position, $q_0(t)$, and trap frequency, $\omega(t)$.

4.1.2 Fourier Excitation

We now have a strong understanding of the characteristics that lead to optimal ion transport. As exemplified by the tanh profile, smoothly varying trajectories, especially near the ends of transport, leads to cold transport that is also robust to the operation time. Under the STA framework, zero motional excitation after

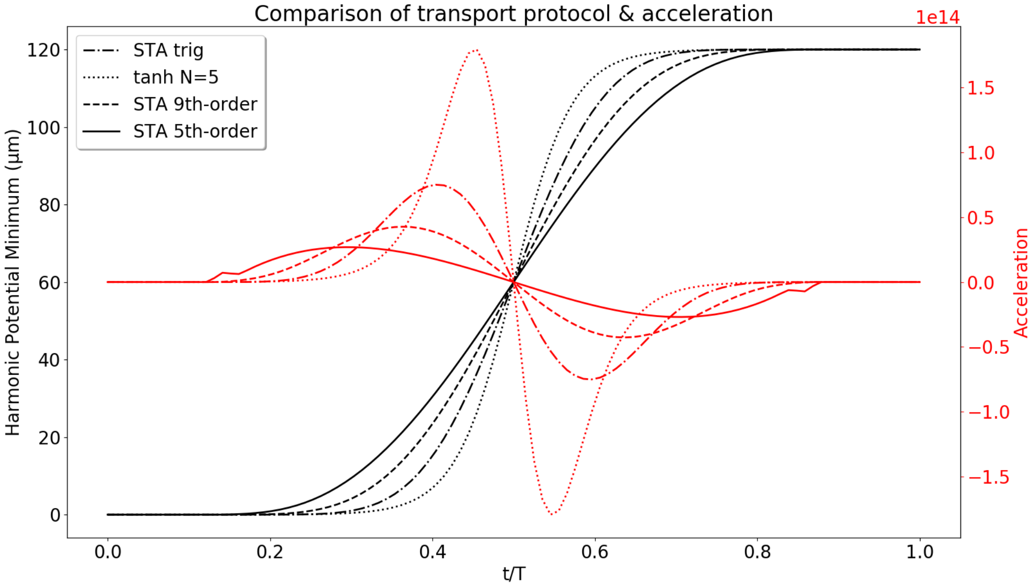

Figure 4-4: Profiles in time of various STA trajectories and hyperbolic tangent.

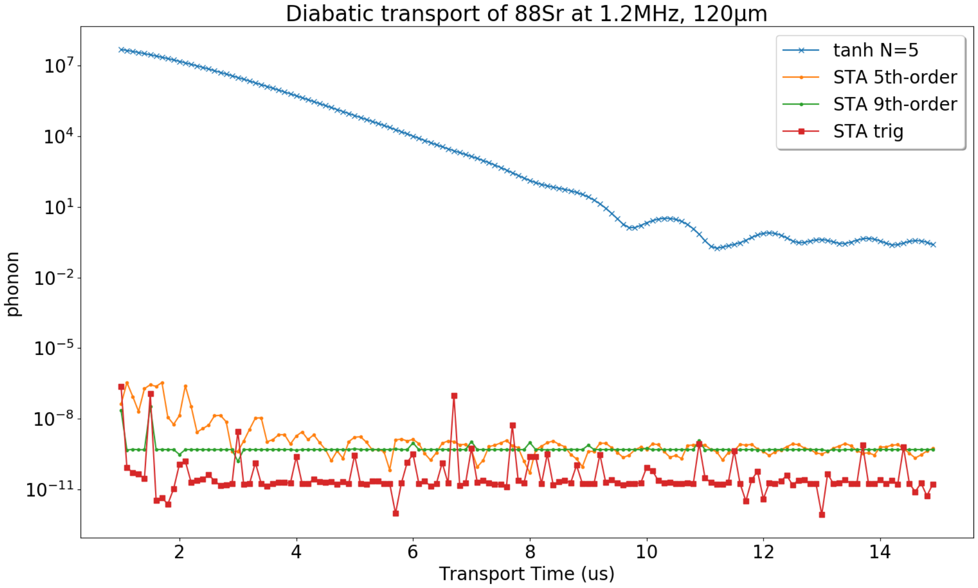

Figure 4-5: Same excitation plot as Fig 4-2 but with more simulated STA trajectories. The quantized excitation from all three STA protocols is synonymous with zero.

transport can be guaranteed by inverse engineering profiles that satisfy a special set of boundary conditions. These trajectories, if perfectly implemented, will lead to no motional excitation even at very fast transport times.

While we understand how the choice of $q_0(t)$ excites the ion during transport, what about the choice of axial frequency ω_0? Are there optimal values of ω_0 and do these values depend on the specific choice of trajectory?[2]. To answer this question we reconsider ion transport as a driven, stationary harmonic oscillator, rather than a moving harmonic oscillator, by transforming coordinates from the laboratory frame to the frame of the harmonic minimum. Since the harmonic minimum undergoes an acceleration $\ddot{q}_0(t)$, this frame is not inertial and thus the ions will experience a driving force.

To derive this driving term, we can rewrite our transport Hamiltonian (4.17) using the classical equation of motion for ions in a harmonic trap (4.15). The ion's harmonic motion in a rigid trap is proportional to $e^{-i\omega_0 t}$ and thus the acceleration of the trap minimum is given by $\ddot{q}_0(t) = -(\ddot{a} + \omega_0^2 a)$. We then rewrite the transport Hamiltonian as,

$$\hat{H}(t) = \frac{p^2}{2m} + \frac{1}{2}m\omega_0^2 q^2 + m\ddot{q}_0 q \tag{4.25}$$

which looks like a normal harmonic oscillator Hamiltonian but with an additional inertial force, $F_{\text{inertial}}(t) = -m\ddot{q}_0(t)$. Therefore, an ion in the harmonic potential reference frame experience a driving force that is proportional to the acceleration of the transport profile. As is well-known with driven harmonic systems, the ion will become excited if the inertial driving force is resonant with the trap frequency, ω_0.

To analyze the spectral components of this driving force for several well-known transport profiles, I plot the Fourier Transform (FFT) of each profile's acceleration as I vary the transport time. The "spectrograms" of each profile is plotted with transport time (μs) along the x-axis and FFT frequency (Hz) along the y-axis, Figs 4-6, 4-7, 4-8, 4-9. The log magnitude of each profile's FFT is indicated by the heat bar to the right. Note that while the transport profiles, $q_0(t)$, for sin and tanh transport are independent of the choice of axial frequency, ω_0, the STA protocol in (4.23) actually depends on the axial frequency, which I asserted to be 1.2 MHz in my simulations.

---

[2] keep in mind that we are only focusing on rigid transport, where ω_0 is constant

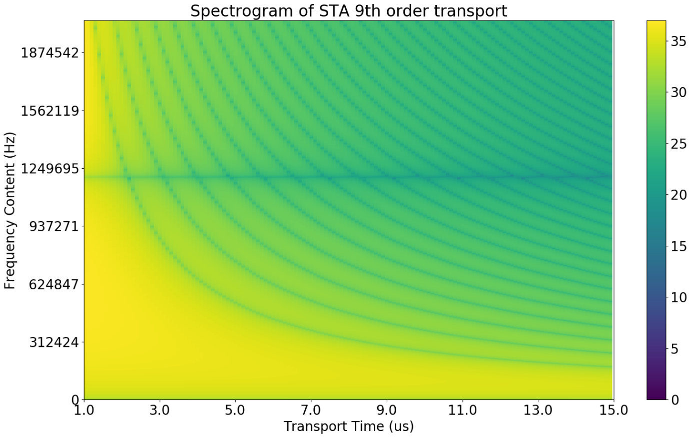
Spectrogram of STA 9th order transport

Figure 4-6: STA 9th order polynomial.

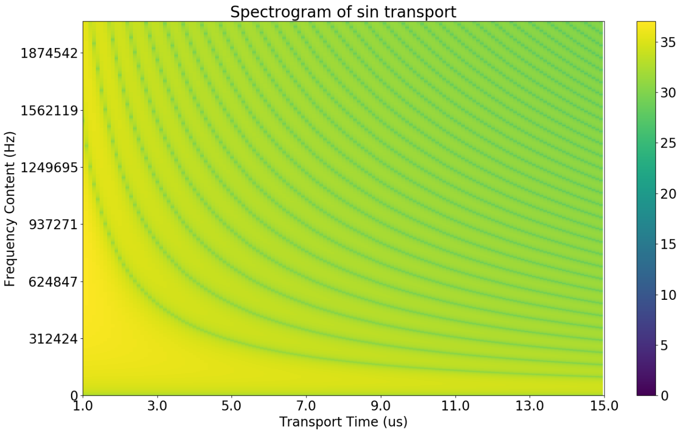
Spectrogram of sin transport

Figure 4-7: Sinusoidal transport

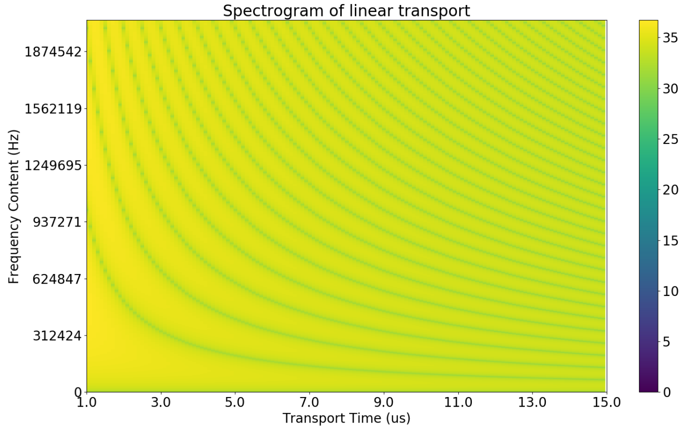
Spectrogram of linear transport

Figure 4-8: Linear transport

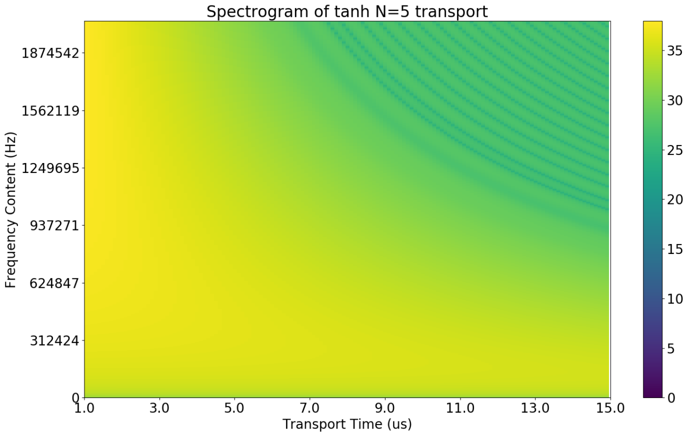
Spectrogram of tanh N=5 transport

Figure 4-9: Hyperbolic tangent, $N = 5$

From spectrogram of STA transport, we can immediately notice a horizontal notch right at the ion's axial frequency 4-6. This means that the inertial force the ion experiences will not resonantly excite the ion's motion, no matter the transport time. Next, we observe that the magnitude of the spectrogram of sin and linear transport is quite large at 1.2 MHz but occasionally dips at certain transport times 4-7 4-8. The magnitude of the frequency content for tanh, $N = 5$

transport remains quite large at 1.2 MHz until the transport time reaches around 11 μs, after which the magnitude dips significantly and stays down 4-9.

We can take a horizontal "slice" of each transport protocol's spectrogram at the ion's axial frequency. For every transport time along the x-axis, we plot the log magnitude of the FFT component at 1.2 MHz in Fig 4-10.

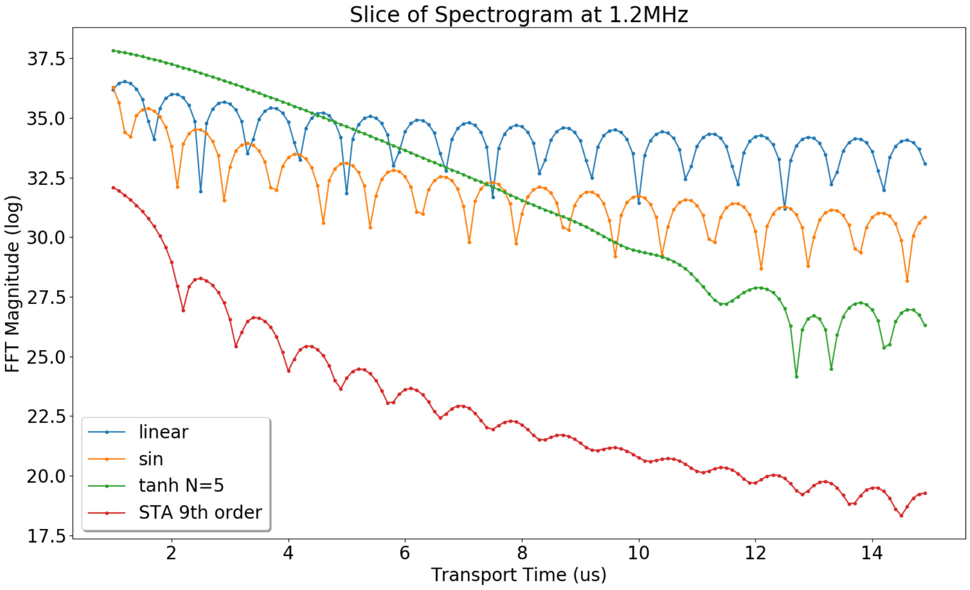

Figure 4-10: Slice of spectrograms at the 1.2 MHz axial frequency.

Notice how well plot 4-10 corresponds with the motional excitation plot in 4-2, implying that there exists a correlation between the spectral density of the driving force at the ion's trap frequency and the motional excitation after transport. While this correlation is purely qualitative, it suggests the excitation after transport is proportional to the trap acceleration at the axial frequency,

$$\bar{n} \propto \int_0^T e^{-i\omega_0 t} \ddot{q}_0(t) dt \tag{4.26}$$

where $\bar{n}$ is the quantized motional energy gained by the ion after transport. We can actually compare this relation to analytical calculations of rigid transport using generating functions and propagators [27],

$$\bar{n}(T) = \frac{m}{2\hbar\omega_0}\left(\omega_0^2\xi(T,0)^2 + \dot{\xi}(T,0)^2\right) \tag{4.27a}$$

$$\xi(T,0) = -\frac{1}{\omega_0}\int_0^T \sin\big(\omega_0(T-t')\big)\ddot{q}_0(t')dt' \tag{4.27b}$$

$$\dot{\xi}(T,0) = -\int_0^T \cos\big(\omega_0(T-t')\big)\ddot{q}_0(t')dt' \tag{4.27c}$$

where ξ is defined as the classical position of the ion relative to the moving potential minimum. ξ and $\dot{\xi}$ can be seen as the convolution of the trap acceleration with sin and cos, resulting in $\bar{n}(T)$ being proportional to the Fourier Transform of the trap acceleration squared, $\ddot{q}_0^2(t)$.

Using this spectrogram perspective, we can now understand how our choice of axial frequency ω_0 affects transport results. For example, if we wanted to transport an ion with a tanh, $N = 5$ protocol (Fig 4-9) over 10 μs, we should confine the ion at a frequency of at least 1.5 MHz. Confining the ion at less than 1 MHz, would land us in a yellow region instead, and we would expect the ion to be greatly excited. Assuming we are able to perfectly achieve the transport profile $q_0(t)$ on our surface traps, these spectrograms can inform our choice of both transport time, T, and axial frequency, ω_0.

Furthermore, keeping the Fourier picture in mind can also help us in designing transport protocols, $q_0(t)$. We saw previously that smoother choices of $q_0(t)$, such as tanh, leads to hot transport at fast transport times, but consistently cold transport after an intermediate transport time. This cutoff transport time signifies the transition from the diabatic to adiabatic regime. Because the trap acceleration varies smoothly for tanh (compared to the acceleration kicks in the linear and sin profile), the spectral density of the trap acceleration remains localized around frequencies corresponding to the transport time ($1/T$). Conversely, transport profiles with discontinuous trap accelerations will have higher frequency harmonics, leading to a spectral density spaced out over a wider frequency range, with interspersed frequency regions that have little spectral content.

Note also, that all the STA transport protocols (4.22), (4.23), (4.24), utilize the axial frequency ω_0 in the profile. This is not a coincidence, as these protocols are specially designed to cancel any trap acceleration at the axial frequency for all possible transport times.

For rigid ion transport in general, the larger the axial frequency, the less the ion's motion will get excited for a given trap acceleration, $q_0(t)$. This is consistent with the criteria for adiabatic changes, $\frac{1}{\omega^2}\frac{\mathrm{d}\omega}{\mathrm{d}t} \ll 1$. The higher the trap frequency, the less the potential will change during a single trap period, and thereby the onset of adiabaticity will appear faster.

We have now seen that optimal transport can be done with STA protocols at arbitrarily fast speeds (not considering the speed limits of our ion trap control system). The higher the axial frequency ω_0 and the more rigid it is during transport will allow one to transport ions faster while being confident that they will gain minimal excitation. Although it is advantageous to transport at as high of an axial frequency as possible given the surface trap's voltage bounds and electrode layout, too high of an axial frequency can actually weaken the radial confinement.

4.2 Splitting Profiles

Using the quartic axial potential to split an ion chain, as described in (1.3), we can now engineer profiles for our control coefficients, $\alpha(t)$ and $\beta(t)$. The dynamics for two ions in a fourth-order potential has been well known [26]. We can describe the 1D Hamiltonian in the axial ($\hat{y}$) direction as follows,

$$H = \frac{p_y^2}{2m} + V(y,t) \tag{4.28}$$

$$V(y,t) = q\left(\alpha(t)y^2 + \beta(t)y^4\right) = q\phi(y,t) \tag{4.29}$$

where q and m are the charge and mass of the ion, respectively. Note that we have constructed the electric potential ϕ to be symmetric in the axial direction. This is not always true, as there can exist some surface charges on the trap electrodes that add a stray field: $\phi(y) = \gamma y + \alpha y^2 + \beta y^4$. However, the anharmonicity due to a cubic term in the potential can be safely neglected due to small contribution in surface traps [31].

For two ions of the same mass and charge, the equilibrium positions in a symmetric ($\gamma = 0$) quartic potential are $y = \pm d/2$, where, d, the separation of the two ions, is given by,

$$\beta d^5 + 2\alpha d^3 = \frac{q}{2\pi\epsilon_0} \tag{4.30}$$

Note that α, β, and d are all implicit functions of time, and q is the charge of the ion species.

In a two-ion chain, there will be two normal modes in the axial direction: a symmetric, center of mass oscillation and antisymmetric, stretch oscillation. The COM and stretch frequencies, $\omega_1(t)$ and $\omega_2(t)$, are given by,

$$\omega_1^2 = \frac{q}{m}\left(2\alpha + 3\beta d^2\right) \tag{4.31}$$

$$\omega_2^2 = \omega_1^2\left(1 + \tilde{\epsilon}\right) \tag{4.32}$$

where $\tilde{\epsilon} = \frac{q^2}{\pi\epsilon_0 m\omega_1^2 d^3}$.

Intuitively, the COM frequency results from locally approximating the quartic electric potential $\phi(y)$ with a harmonic potential. The stretch frequency is larger than the COM frequency by a factor of $\sqrt{1+\tilde{\epsilon}}$, where $\tilde{\epsilon}$ is the ratio of the Coulomb force to a harmonic restoring force with frequency ω_1.

We can analyze the mode frequencies in the three cases of interest (1-2, 1-3, 1-4). In a purely harmonic well, $\alpha > 0$; $\beta = 0$; $\tilde{\epsilon} = 2$; and $\omega_2 = \sqrt{3}\omega_1$, consistent with the discussion in 2.2.3.

At the critical point $\alpha = 0$; $\beta > 0$; $\tilde{\epsilon} = 2/3$; the ions are separated by a distance,

$$d_{\text{cp}} = \left(\frac{q}{2\pi\epsilon_0\beta}\right)^{1/5} \tag{4.33}$$

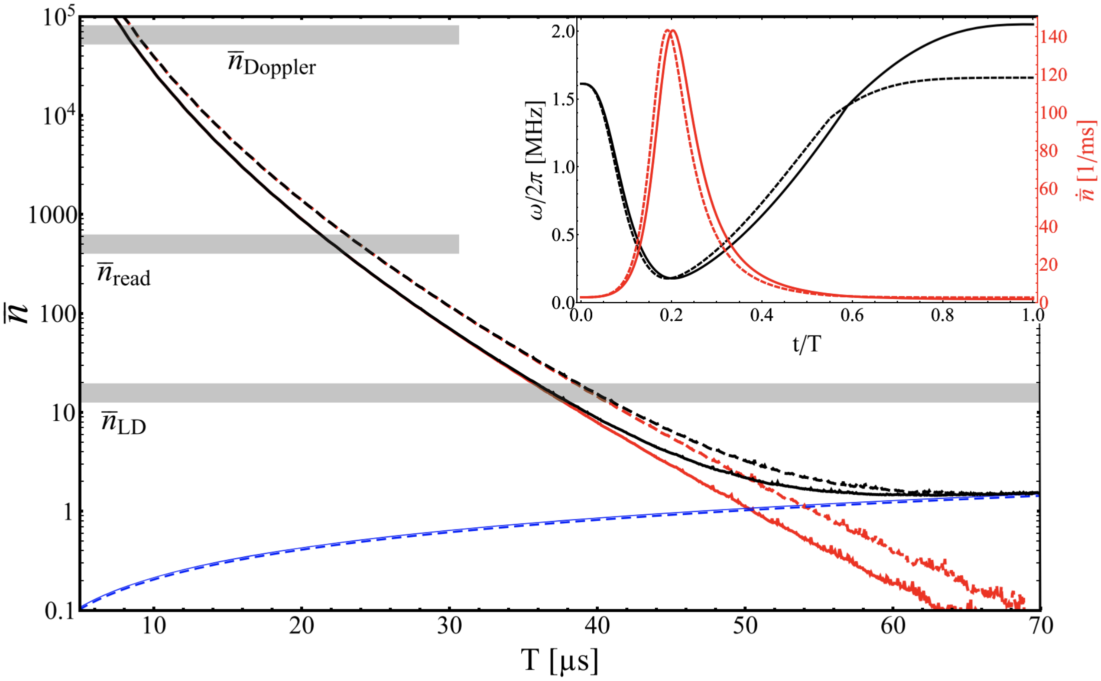

Figure 4-11: A typical splitting profile from [31]. Motional excitation from splitting (red), thermal excitation from electric field noise (blue), and total energy transfer (black). The top right inset shows the axial frequency (black) and heating rate (red) during transport.

and the COM frequency is,

$$\omega_{1\ \text{cp}} = \left(\frac{q}{2\pi\epsilon_0}\right)^{0.2} (\beta)^{0.3} \left(\frac{3q}{m}\right)^{0.5} \propto \beta^{0.3} \tag{4.34}$$

From (4.34) we can see that the frequency at the critical point scales unfavorably with β. Thus a much larger β value is needed to keep the COM frequency at typical axial frequencies levels (∼1 MHz).

Finally, in a double well configuration 1-4, when the two ions are sufficiently separated such that the Coulomb interaction is negligible, $\tilde{\epsilon} \ll 1$. The two mode frequencies are both about equal to the oscillation frequency of a single ion in either trap, $\omega_1 \approx \omega_2$.

In summary, there are four parameters of interest during a splitting operation: $\alpha(t)$, $\beta(t)$, $d(t)$, and $\omega_1(t)$, with their relationships given by (4.30), (4.31), (4.32).

In a typical splitting experiment, one chooses an appropriate trajectory for the separation of two ions, $d(t)$ [31]. Because the axial mode frequencies naturally drop near the critical point, it is advantageous to slow down voltage changes to avoid diabatically exciting the ions in the weak confinement. The maximum quartic confinement β_{max} at the critical point is determined by the voltages that can be applied to the electrodes, as well as the electrode size, layout, and distance away from the ions. Voltages are then smoothly changed from the critical point configuration to a double well ($\alpha < 0$), where the ions are sufficiently separated.

Since the axial frequencies change during splitting, we are no longer in the regime of rigid shuttling operations, as in the case of transport. As seen in Fig 4-11, the motional excitation for splits faster than 40 μs would actually bring the ions out of the Lamb-Dicke regime. The drop in axial frequency near the critical point dramatically increases the heating rate. Ions during slower splitting times are subjected to more thermal excitation from trap effects. Thus fast splitting below 1 quanta has proven to be quite difficult on surface electrode traps.

4.2.1 Shortcuts-to-Adiabaticity

Invariant-Based Inverse Engineering has also been applied to the problem of fast ion crystal splitting [53]. The splitting Hamiltonian (4.28) was transformed into coordinates of the dynamical normal modes $q_\pm$, $p_\pm$ corresponding the same frequencies $\Omega_- = \omega_1$, $\Omega_+ = \omega_2$ in (4.31), (4.32) [39].

The Hamiltonian under these coordinates can be written as the sum of the Hamiltonian in each normal mode, $H = H_+ + H_-$. The two Hamiltonians have a dynamical invariant of the form [53],

$$I_\pm = \frac{1}{2}\left[\rho_\pm(p_\pm - \dot{x}_\pm - \dot{\rho}_\pm(q_\pm - x_\pm)\right]^2 + \frac{1}{2}\Omega_\pm^2(0)\left(\frac{q_\pm - x_\pm}{p_\pm}\right)^2 \tag{4.35}$$

where the auxiliary functions $\rho_{\pm}$ and x_{+} satisfy,

$$\ddot{\rho}_{\pm} + \Omega_{\pm}^{2}\rho_{\pm} = \frac{\Omega_{\pm}^{2}(0)}{\rho_{\pm}^{3}} \tag{4.36}$$

$$\ddot{x}_{+} + \Omega_{+}^{2}x_{+} = -\sqrt{\frac{m}{2}}\ddot{d} \tag{4.37}$$

Note that $x_{\pm}$ are the normal mode centers in the dynamical mode coordinates $q_{\pm}$, $p_{\pm}$. By symmetry, $x_{-} = 0$.

Analogous to STA transport, ensuring that the splitting Hamiltonian commutes with the dynamical invariants lead to the following set of 14 boundary conditions at the boundary times $t_b = \{0, T\}$,

$$\rho_{\pm}(0) = 1, \qquad \rho_{\pm}(T) = \sqrt{\frac{\Omega_{\pm}(0)}{\Omega_{\pm}(T)}}, \tag{4.38}$$

$$\dot{\rho}_{\pm}(t_b) = \ddot{\rho}_{\pm}(t_b) = \dddot{\rho}_{\pm}(t_b) = \ddddot{\rho}_{\pm}(t_b) = 0, \tag{4.39}$$

$$x_{+}(t_b) = \dot{x}_{+}(t_b) = 0 \tag{4.40}$$

A 9th- and 11th-degree polynomial ansatz is used for ρ_{-} and ρ_{+}. To satisfy these boundary conditions, the coefficients of $\rho_{\pm}$ depend only on the ratio of the starting to ending axial mode frequencies $\sqrt{\frac{\Omega_{\pm}(0)}{\Omega_{\pm}(T)}}$.

We start the split with a single well: $\Omega_{-}(0) = \omega_0$ and $\Omega_{+}(0) = \sqrt{3}\omega_0$. We end the split by choosing an target separation distance and determining the modes frequencies based on (4.31), (4.32). Note that we constrain the final COM frequency to be the same as the starting COM frequency, $\Omega_{-}(T) = \omega_0$. This is crucial as it allows us to solve for splitting profiles that keep a constant COM frequency throughout the operation.

Once we have fixed our target mode frequencies at the initial and final times of the split operation, we solve for the auxiliary function $\rho_{\pm}(t)$ throughout the entire split. From this we obtain the mode frequencies throughout the entire split, $\Omega_{\pm}(t)$ according to the auxiliary function (4.36).

When the two axial mode frequencies are fully determined, we can rearrange the relationships in (4.30), (4.31), (4.32) to obtain the following relations,

$$d(t) = \left(\frac{q}{m\pi\epsilon_0(\omega_2^2 - \omega_1^2)} \right)^{1/3} \tag{4.41}$$

$$\alpha(t) = \frac{1}{8}m\left(3\omega_2^2 - 5\omega_1^2\right) \tag{4.42}$$

$$\beta(t) = \frac{q}{2\pi\epsilon_0 d^5(t)} - \frac{2\alpha(t)}{d^2(t)} \tag{4.43}$$

The α, β, ω_1, and ω_2 parameters for this STA split are plotted in 4-12.

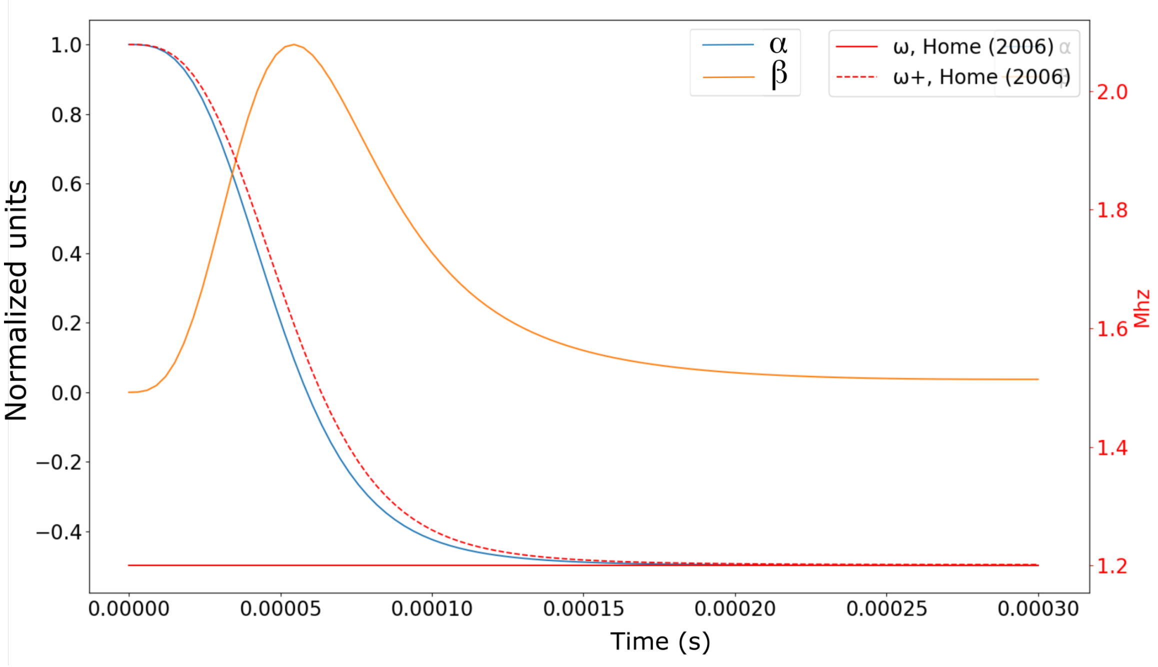

Figure 4-12: STA splitting profile with a flat COM frequency (solid red). The stretch frequency (dashed red) starts off at $\sqrt{3}$ and ramps down to almost be equal to the COM frequency. The quadratic, α, coefficient ramps down to -0.5 its initial value (blue). The quartic, β, term reaches a maximum value at the critical point (orange).

Note that in order to achieve STA splitting we must be able to create a large enough beta value on our trap to provide the necessary axial frequency at the critical point. According to (4.34), to trap two ^{40}Ca ions at 1.3 MHz during the critical point, we need a β value of 2×10^{-7} V/m^4, which is just what the MaxBeta trap can provide with a ±40 V range applied to the electrodes. By comparison, the maximum β achievable on the SLT trap with a ±40 V range is 4×10^{-10} V/m^4,

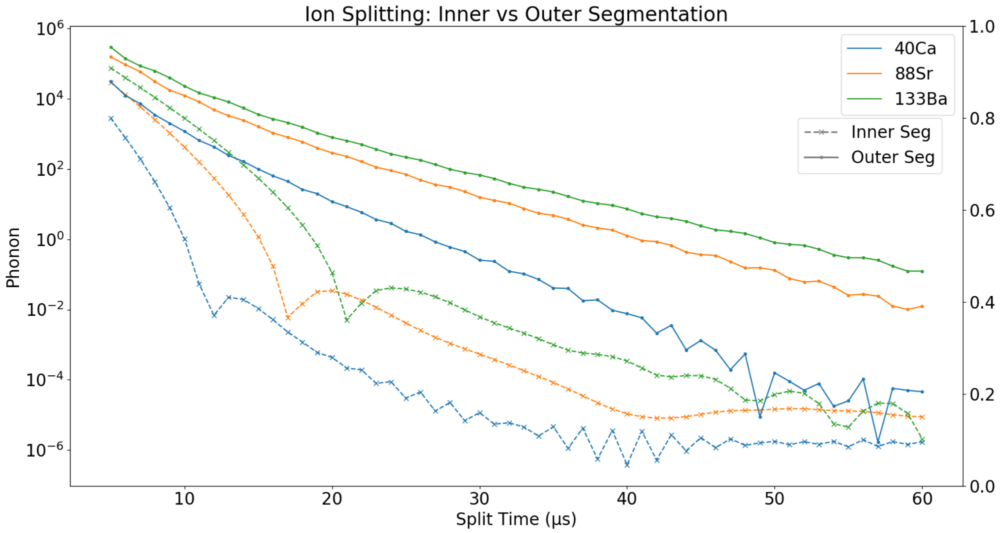

Figure 4-13: Motional excitation in quanta of the common mode oscillation after two types of splitting profiles. Thermal heating from the trap has not been simulated.

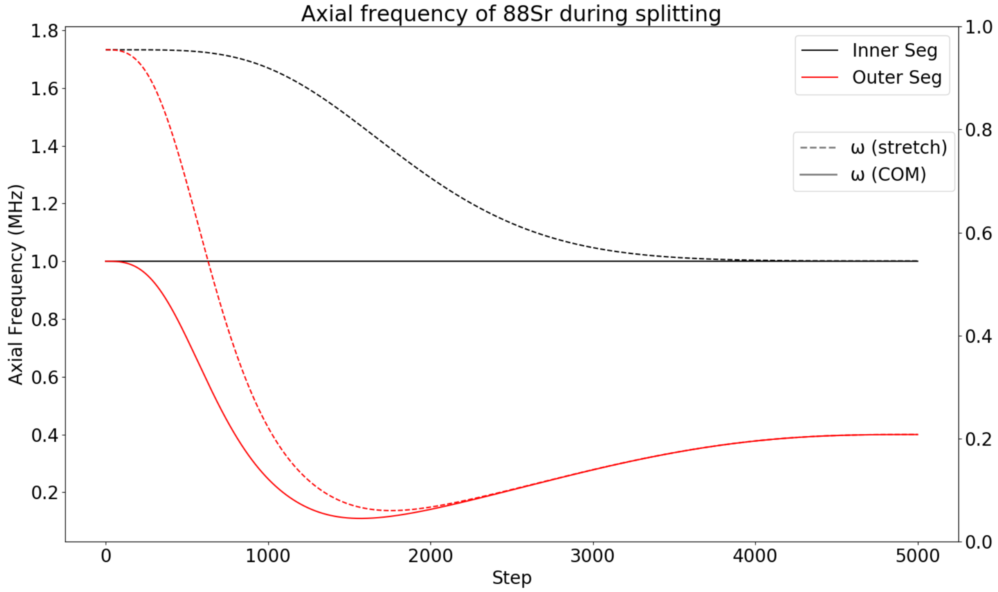

Figure 4-14: Axial frequency modes during the two methods of splitting.

which results in a 200 kHz axial frequency of two ^{40}Ca ions.

I've simulated both the traditional splitting method[3] and STA splitting method

---

[3] I call this the "Kaufmann" method

with realistic parameters for three different ion species: ^{133}Ba, ^{88}Sr, and ^{40}Ca. I plot the motional excitation in the common mode as a function of splitting time in Fig 4-13. Since the Kaufmann splitting method we analyzed for an outer segmented trap, which has a lower maximum β value compared to inner segmented electrodes, the motional excitation and axial frequency from the Kaufmann method is labelled as "Outer Seg" in 4-13, 4-14.

We can see that heavier ions consistently become more excited after the split, most likely due to the lower confinement from the same applied voltages. With the traditional splitting method, ^{40}Ca reaches an excitation below 1 quanta at around 25 μs. Note that this is faster than the 48 μs simulated in 4-11 because my voltage bounds were ±40 V while the bounds in [31] were ±10 V.

I also plot the simulated axial frequency modes for a single splitting operation of ^{88}Sr in 4-14. With these considerations, we can conclude that inner segmented electrode traps are more suited to achieve optimal ion splitting. Note how the COM frequency stays constant for an STA split. This proves to be advantageous as we shall see in the next section.

4.2.2 Fourier Excitation

In the case of STA splitting, where the common mode frequency of the two ions stays constant during the split, we may use the same spectral analysis that I discussed previously for transport operations. When the COM mode stays flat at $\omega_1 = \omega_0$, we can consider the operation to be "rigid" with respect to the COM frequency.

Analogously, I plot FFT the acceleration of a single ion's position $\ddot{d}_0(t)/2$ during the splitting operation as a function of splitting time. The spectrogram shown in 4-15 shows the magnitude of the ion's acceleration at various split times and frequencies. The axial confinement scales inversely with the mass of the ion, $\omega \propto \sqrt{1/m}$, and thus a 1.2 MHz COM frqeuency for ^{40}Ca leads to a 800 kHz and 658 kHz confinement for ^{88}Sr and ^{133}Ba, respectively.

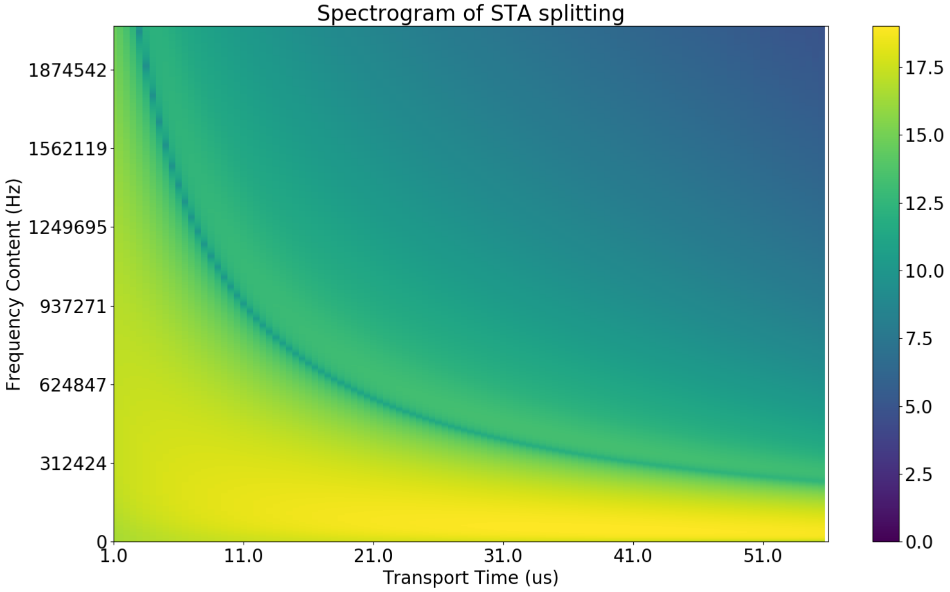

Figure 4-15: Spectrogram of STA splitting. The common mode frequency is set to be 1.2 MHz for ^{40}Ca, and scales inversely with the mass for higher-mass ions.

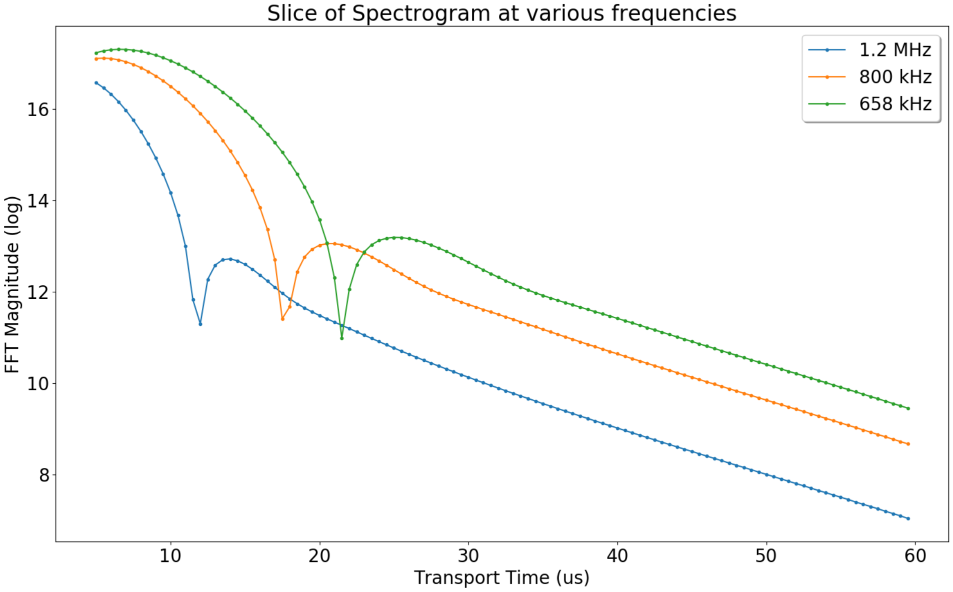

Figure 4-16: Slice of the STA splitting spectrogram at the various axial frequencies corresponding to the ion's mass.

Taking a horizontal slice of the spectrogram at those three frequencies leads to the plot in 4-16. Note that the sharp dip for each ion species occurs at the same

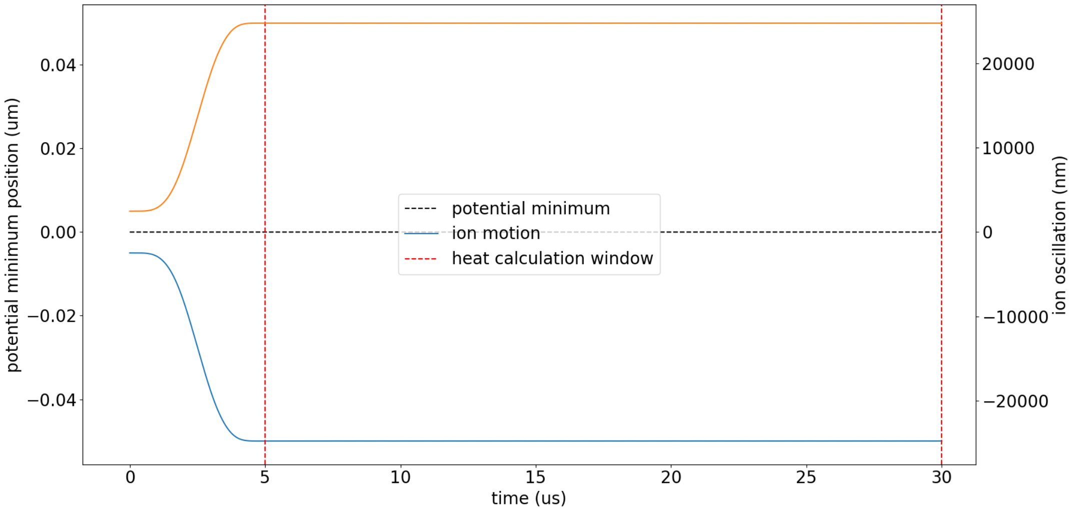

Figure 4-17: Simulation of two ^{40}Ca ions with my splitting profile. $d(t)$ is given by an STA solution (4.23). The ions get separated $\times 10$ their starting distance. Note how the ions follow an STA profile during the 5 μs split.

splitting times as the simulation based on the ion motional dynamics 4-13. While the agreement is again purely qualitative, this points to the fact that lighter mass ions are easier to split [7, 63] and the capability to create a high β confinement with the surface electrode trap may lead to colder and faster split operations. This Fourier analysis of splitting only exists for "rigid" splitting and will not work for the traditional splitting method where the axial frequencies change over time.

We may actually take advantage of what we have learned from STA transport and apply it to STA splitting. The previous method for achieving STA splitting protocols imposed boundary conditions on auxiliary functions, and then solving for the control parameters $\alpha(t)$, $\beta(t)$, leading to a unique separation profile $d(t)$ with a spectrogram 4-15.

It would be more advantageous if we instead first constrain $d(t)$ to be an optimal transport profile, such as (4.23), and constrain the common mode frequency to be constant, $\omega_1(t) = \omega_0$. We can then solve for the stretch mode frequency according to (4.32). Once we have both our mode frequencies as a function of time, we can solve for the control parameters using (4.42), (4.43).

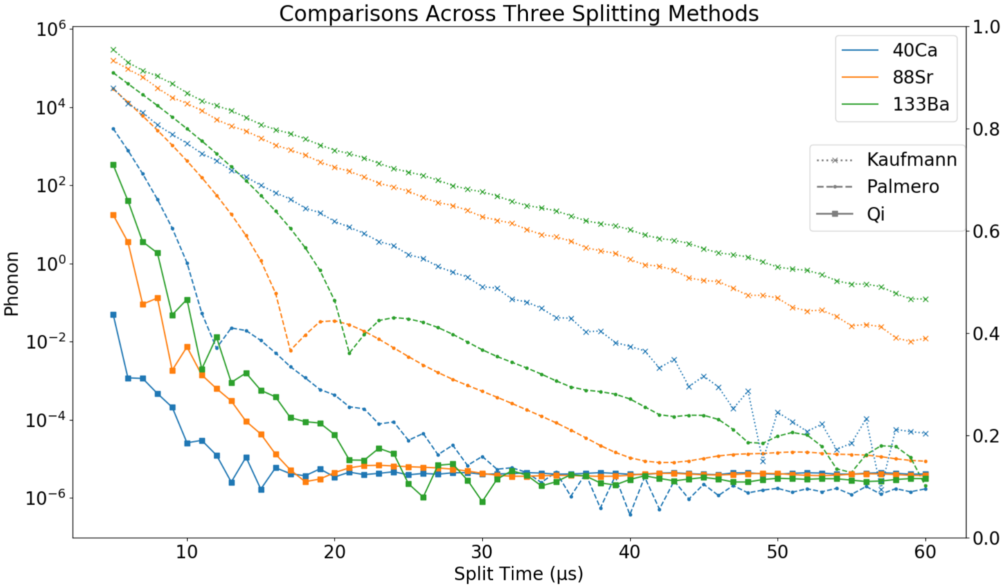

Figure 4-18: Comparisons of my splitting profile with the same two in Fig 4-13. The quanta plotted is the excitation in the common mode.

An example of the ion's trajectory during my splitting protocol is simulated and shown in Fig 4-17. The total split time was 5 μs with the COM frequency held at 1.2 MHz. At the maximum beta configuration, $\beta = 1.56\times10^{-7}$ for this axial frequency. This value of maximum beta confinement is achievable in our MaxBeta trap.

The motional excitation from my split is simulated for the same three ion species and varied over split time. This is plotted together with the excitation in 4-13 to obtain the following excitation plot, Fig 4-17. This suggests that if we are able to perfectly find the voltage waveforms to achieve such a splitting profile, we can split even ^{133}Ba below 1 quanta in under 10 μs.

The spectrogram for this split will be the same as Fig 4-9 because my implementation of $d(t)$ follows the 9th order STA polynomial for ion transport (4.23). Note that with my paradigm, other possible separation distance profiles are possible. The main difference now is that we are operating under "rigid" splitting, where we can keep the COM frequency at a constant value.

This is a new technique for designing optimal splitting protocols for two ions that combines STA techniques with Fourier analysis. Experimental success is thus predicted to be contingent on precision of electrode controls and a trap geometry that can provide a large β value.

4.3 Robustness

In designing optimal shuttling protocols, robustness to systematic errors must be considered since the ion shuttling process is open loop and lacks real-time feedback. Because of this, our best estimates for how the system will behave for any given voltage waveform comes from simulations with as accurate models as possible. For example, our method for predistorting waveforms, detailed in Chapter 5, uses a SPICE model of our electrode filtering in the cost function, and there is no guarantee of the accuracy of the SPICE model without making measurements of the system itself.

While the open-loop system makes predistortion challenging, we may find target protocols that do not require as tightly-bounded voltage waveforms. Such a protocol is said to be robust with respect to a certain deviation. The deviations in ion shuttling experiments can be categorized as positional errors, δq, or trap frequency errors, $\delta\omega$. These errors can in general be time-independent or time-dependent.

It turns out that the excitation sensitivity to positional errors in the transport trajectory $\delta q(t)$ can only be mitigated by decreasing the magnitude of the error and/or decreasing the transport time [43]. In other words, there are no choices of trajectories within the family of STA solutions that will be less sensitive to errors in the trajectory itself. However, at a high enough trap frequency, under the Fourier picture, any additional trap position errors δq will add an extra driving force proportional to $\frac{\mathrm{d}^2}{\mathrm{d}t^2}\delta q$. As long as the spectral density of the trap position error has no frequency components that is resonant with the ion's axial frequency, the additional excitation should be minimal. This can be more confidently guaranteed when the trap frequency ω_0 is high.

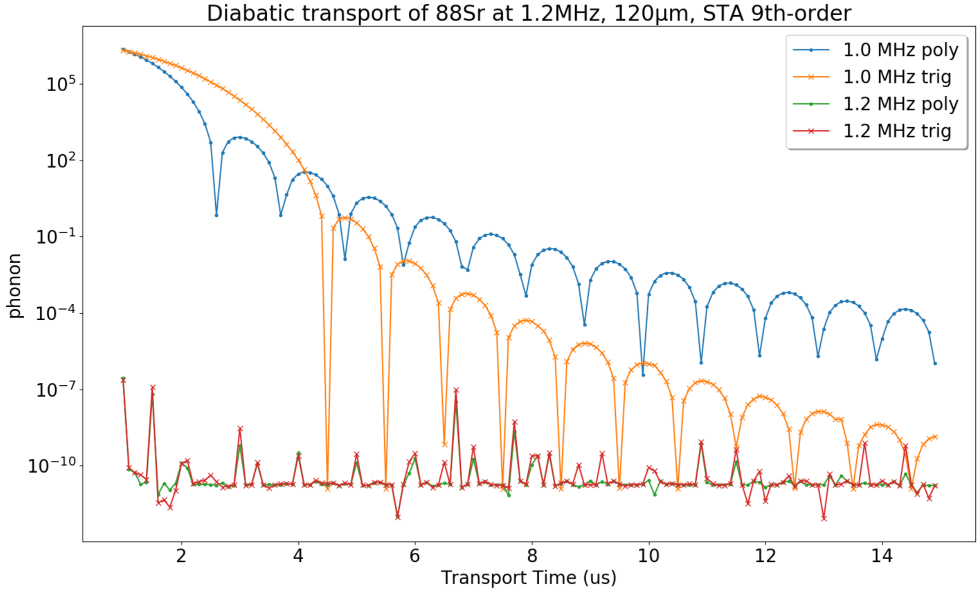

Figure 4-19: Transporting a single ^{88}Sr ion with the polynomial STA (4.23) and the trigonometric STA (4.24). The correct axial frequency for transport is 1.2 MHz, but transport with a frequency of 1.0 MHz has also been simulated.

In the case of time-independent trap frequency errors, there are various protocols within the family of STA trajectories that are robust. Such examples are the N-point protocols and trigonometric ansatz detailed here [81, 40, 42, 43, 21, 41, 38]. Note that there is no free lunch, however. By choosing a protocol that is more robust to time-independent trap frequency errors, the trajectory of the protocol may have oscillations that make them more difficult to implement. The transient excitation of the ions under this trajectory may actually be larger as well. In other words there are always trade-offs to consider when designing these robust protocols [60].

The trigonometric STA transport profile in (4.24) has been shown to be more robust to a time-independent trap frequency error than the polynomial ansatzes. This robustness can be seen numerically in Fig 4-19. The polynomial and trigonometry ansatz were solved with a target trap frequency of 1.2 MHz, and when ^{88}Sr was transport at that trap frequency, we do observe essentially no motional excitation for all transport times. However, if we introduce a 200 kHz trap frequency offset, so we are now transporting ^{88}Sr with the same profile but trapped at 1.0 MHz instead, we see much more motional excitation. However, for the trigonometric STA profile, the excitation is consistently lower starting at around 5 μs.

For the case of a time-dependent trap frequency error, $\delta\omega(t)$, it is not well known how to analytically find shuttling protocols that are robust. This problem is even more complex when there are both time-dependent trap frequency errors and positional errors. Thus, finding trajectories that are robust to time-dependent trap frequency errors is an open research question in the field of robust quantum particle shuttling.

4.3.1 Experimental Non-Idealities

In trapped-ion systems, we may typically see both trap position and trap frequency errors that arise from a variety of sources. The first type of noise source results from imperfect voltage controls. If predistortion is not perfect, the resulting waveforms can lead to both time-dependent trap frequency errors and positional errors. Also, there can be errors that arise from solving for voltage waveforms as detailed in section 3.2.1.2. In general it is not yet known if any arbitrary shuttling profile has exact waveform solutions and even so, it is not guarenteed that those waveforms can be sufficiently predistorted and applied to the trap. However, using waveform solving techniques and the predistortion method in Chapters 3 and 5, we may try our best to find close to optimal waveforms which would mitigate the trap position and trap frequency errors from imperfect controls.

Perhaps more concerning, are the other sources of noise that we have less control over. For example, the trap frequency may vary across a surface trap by more than 5%, due to local trap imperfections, patches of charged insulator or adsorbate, and/or stray fields [60]. Furthermore, gain and calibration errors in our DACs, as well as some crosstalk effects between different channels on the hardware system can also contribute to both trap position and trap frequency errors. It may be difficult to "predistort" for these errors because, unlike with the circuit filtering, these noise characteristics are only estimated and may change over time. Therefore, our trap frequency may end up varying during the shuttling operation even with perfectly predistorted waveforms. We can numerically simulate these voltage errors with my numerical pipeline using estimates for gain, calibration offset, and crosstalk effects, but ultimately the best probe on these errors is the ion itself.

To summarize, we can optimize our voltage inputs to reduce the trap position and trap frequency errors as much as possible. However there will still be unaccounted effects from surface charging to crosstalk errors that will introduce some nonzero amount of trap position and trap frequency errors. While it is possible to design shuttling protocols that are robust to time-independent trap frequency errors, it is impossible to be robust against trap position errors. The only ways to reduce the sensitivity to trap position errors, is to perform the shuttling operation at a faster speed and/or increase the trap frequency. However, this might not be experimentally possible without introducing more trap position or trap frequency errors.

Future work remains to be done towards quantifying the bounds on the contribution of surface noises to trap position and frequency errors using known characteristics of modern surface electrode traps.

4.4 Summary

This chapter has presented state-of-the-art theories validated by simulations for optimal shuttling operations. A Fourier analysis perspective has been detailed that helps crystallize the core requirement for shuttling operations to be optimal: a tight and rigid axial confinement.

For ion transport, it is experimentally easier to meet both the tight and rigid trapping requirements. The inner segmented layout of our MaxBeta trap allows for ^{40}Ca to be easily trapped at 4 MHz with an 8 V control range. Ensuring rigidity during transport is less straightforward, and requires precise simulation of electric potentials during the operation. Ultimately, one may choose to accurately model the electrode circuitry and use my predistortion method detailed in the next chapter to optimize the voltage inputs.

For ion splitting, both the tight and rigid requirements are more challenging to satisfy. As will be discussed in Chapter 6, our work on the MaxBeta trap is a first step towards tight and rigid splitting.

Robustness shuttling trajectories may help relax the tight and rigid requirements. While the requirement for tight confinement is largely dependent on the surface trap layout, the rigid requirement requires strong voltage controls. The design of shuttling trajectories that are robust to trap frequency errors—especially time-dependent trap frequency errors—may help ease the need for precise voltage controls and is an active area of investigation.

Chapter 5

Voltage Optimization

While finding optimal control potentials is one challenge, actually implementing them on our surface traps is a separate challenge. Due to our system filtering, we have imperfect control over electrode voltages. Diabatic shuttling times on the order of 1-10 μs require voltage waveforms that must vary on the order of 100 kHz - 1 MHz, which is beyond the low pass filter cutoff. Therefore I will demonstrate the need for predistortion and outline my method in this chapter.

Using the methods described in the previous chapter, we have identified candidate profiles for optimal ion transport and ion shuttling. We solve for the voltage waveforms we should apply to our MaxBeta trap in order to achieve these optimal protocols, shown in 5-1, 5-2.

We can predict the waveform distortion by our electrode circuitry using time-domain simulations with SPICE. The naïve method for waveform generation is to sample the target waveform at the update rate limited by our DAC. Running the DAC input through our SPICE simulator, we are able to see the distorted waveforms and compare with the targeted waveform 5-3.

The digital input from our digital-to-analog converter is modelled as a piecewise linear voltage source, with a slew rate and update rate shown in Fig 5-3. While the electrode output is quite delayed, the shape of the waveform also becomes distorted. There are also small oscillations towards the end of the analog output.

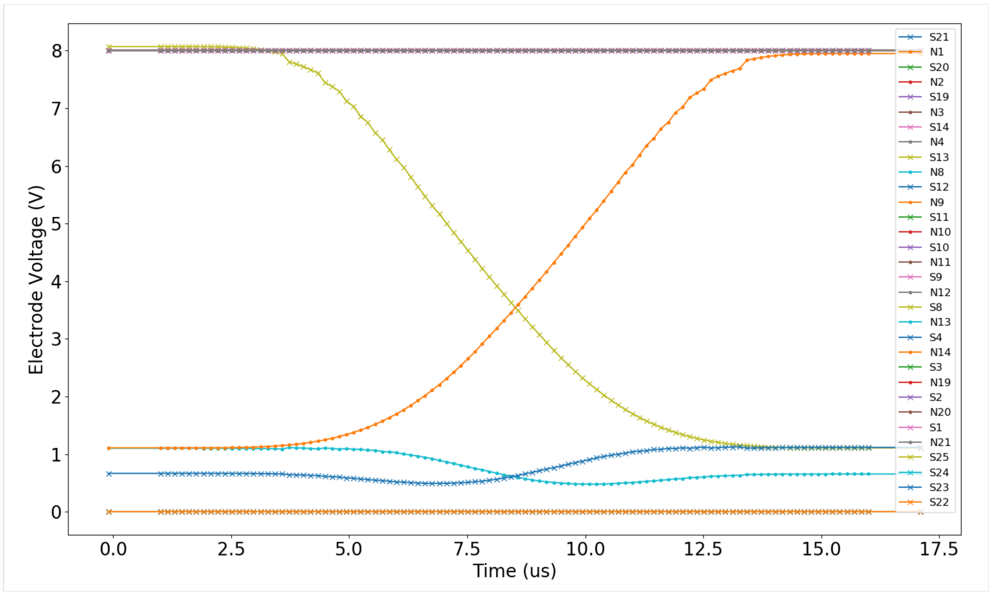

Figure 5-1: Ion transport waveforms on the MaxBeta trap. Transporting ^{40}Ca according to an STA polynomial protocol (4.23), over a distance of 45 μm in 15 μs. The axial frequency is 4 MHz.

We can imagine that the optimal inputs to achieve the target waveforms will have to occur before the waveforms. To account for the low-pass filtering, we expect to have to drive our inputs with larger voltages than the target waveforms. Because we have limited resolution on our inputs (16-bit 0-5V), there are a large but finite number of possible voltage inputs to the electrodes. Furthermore we are able to create a cost function by quantifying the error, ϵ resulting from the distortion using a sum of squares difference

$$\epsilon = \int_0^T |V_i(t) - \hat{V}_i(t)|^2 dt \tag{5.1}$$

where $V_i(t)$ and $\hat{V}_i(t)$ are our achieved and target waveforms, and T is the shuttling operation time.

This allows us to transform the problem of finding optimal voltage controls into a global search over a large parameter space. With 2^{16} possible voltage levels per inputs, x inputs per waveform, and N electrode waveforms per shuttling op-

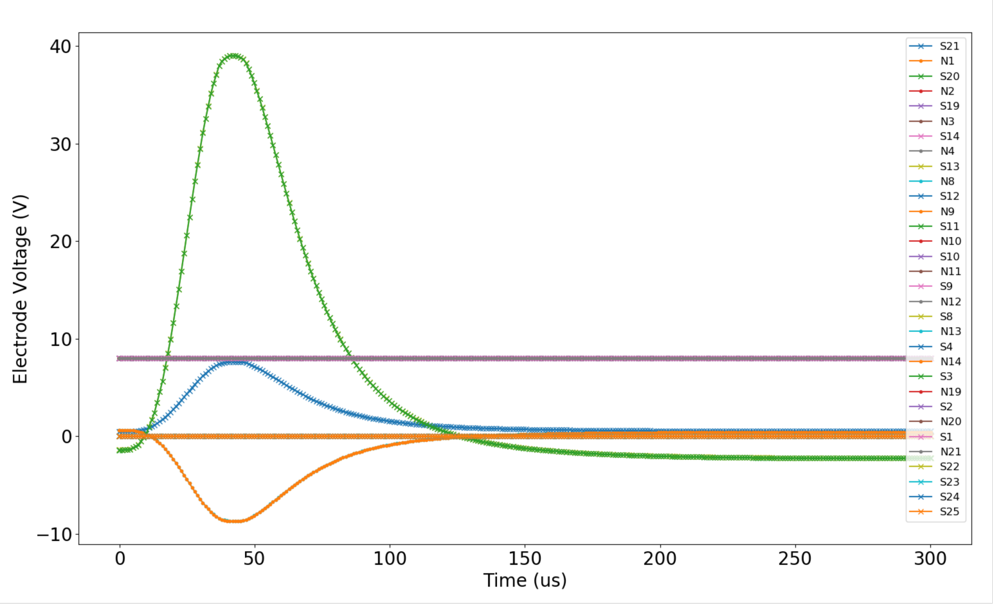

Figure 5-2: Splitting waveforms on the MaxBeta trap. Splitting two ^{40}Ca according to my developed method in chapter 4. $d(t)$ according to (4.23), COM frequency of 1.2 MHz. Final ion separation of 90 μm.

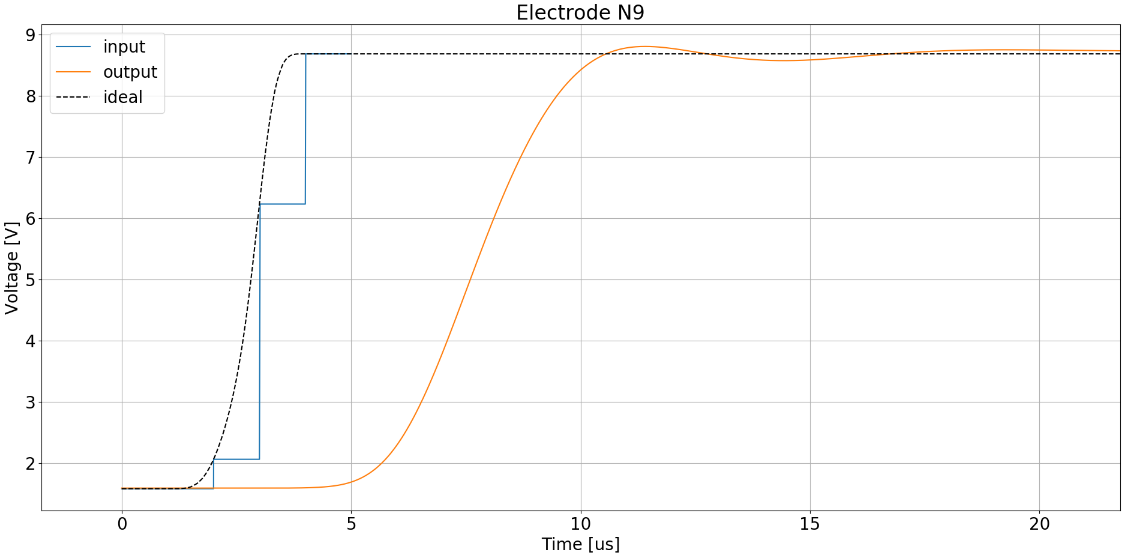

Figure 5-3: DAC input voltages modelled with a piece-wise linear function (blue). Analog output simulated with SPICE (orange). The target waveform is what we want to apply to the trap electrodes (dashed black).

eration, searching over the entire input space quickly becomes computationally expensive. One SPICE simulation takes around 2 seconds, so 2^{16} SPICE simulations will take 36 hours. A more sophisticated method for predistortion is to analyze waveforms in the frequency domain.

5.1 Spectral Content of Voltage Waveforms

The Fourier transform of voltage waveforms allows one to observe the required frequencies in achieve such a waveform. Waveforms with extensive high frequency content will naturally be distorted more than lower frequency waveforms.

In the diabatic transport voltages 5-1, only four electrodes change: S13, N8, S13, N9. The rest are held constant at 8 V. I allowed only these four electrodes to change because they were the closest to the ion's position and I only constrained six coefficients: $\left[\frac{\partial}{\partial x}, \frac{\mathrm{d}}{\mathrm{d}y}, \frac{\partial}{\partial z}, \frac{\partial^2}{\partial y^2}, \frac{\partial^2}{\partial x \partial y}, \frac{\partial^2}{\partial y \partial z}\right]$.

The Fourier transform of the four electrode waveforms is shown in 5-4. The inputs to the system had a update rate of 800ns, with 5 total inputs, the target waveforms lasted 4 μs. The y-axis is the magnitude of the FFT on a dB scale. The waveforms reach a value of -20 dB as low as 150 kHz.

For lower frequency waveforms, filtering may effectively just time delay the waveform, while maintaining the overall shape. There is a greater need for predistortion when our filtering changes the shape of our waveform.

By naïvely sampling our target waveforms, we can see unequal distortion. The shape of the output waveforms for electrodes N8 and S12 are more distorted than electrodes N9 and S13. This is because of the dip in the target waveforms of electrodes N8 and N9. Note that all the electrode outputs seem to be delayed in time by similar amounts, suggesting that the various target waveforms undergo similar group delay effects from our electrode circuitry. Also note that since the target waveforms 5-1 are symmetric in time (electrode N8 and S12 are time-inverses, as are N9 and S13), the naively sampled waveforms can be run forward and backwards.

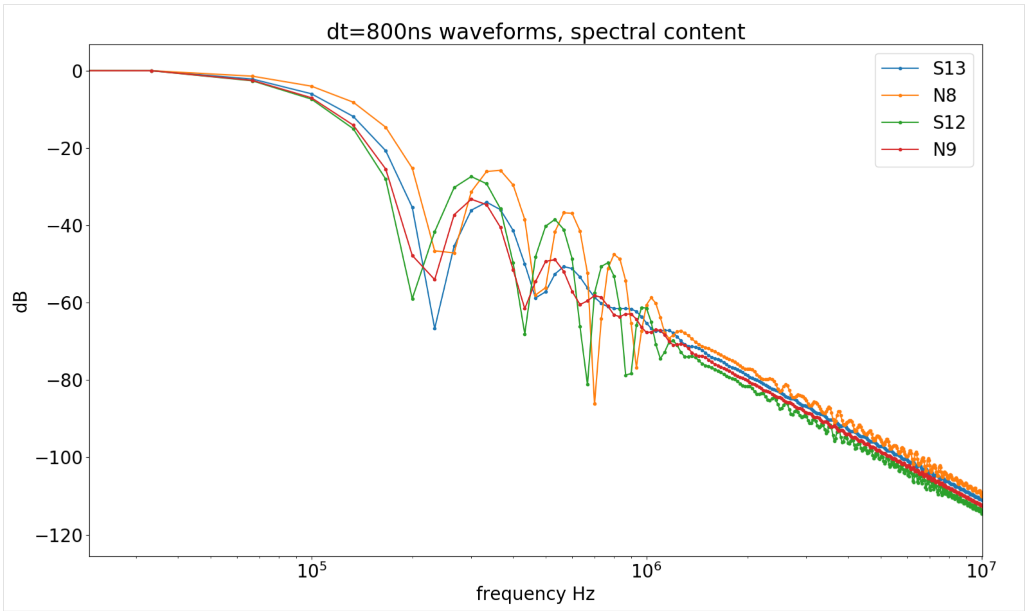

Figure 5-4: Spectral content of diabatic transport voltages. The total transport time is 4 μs.

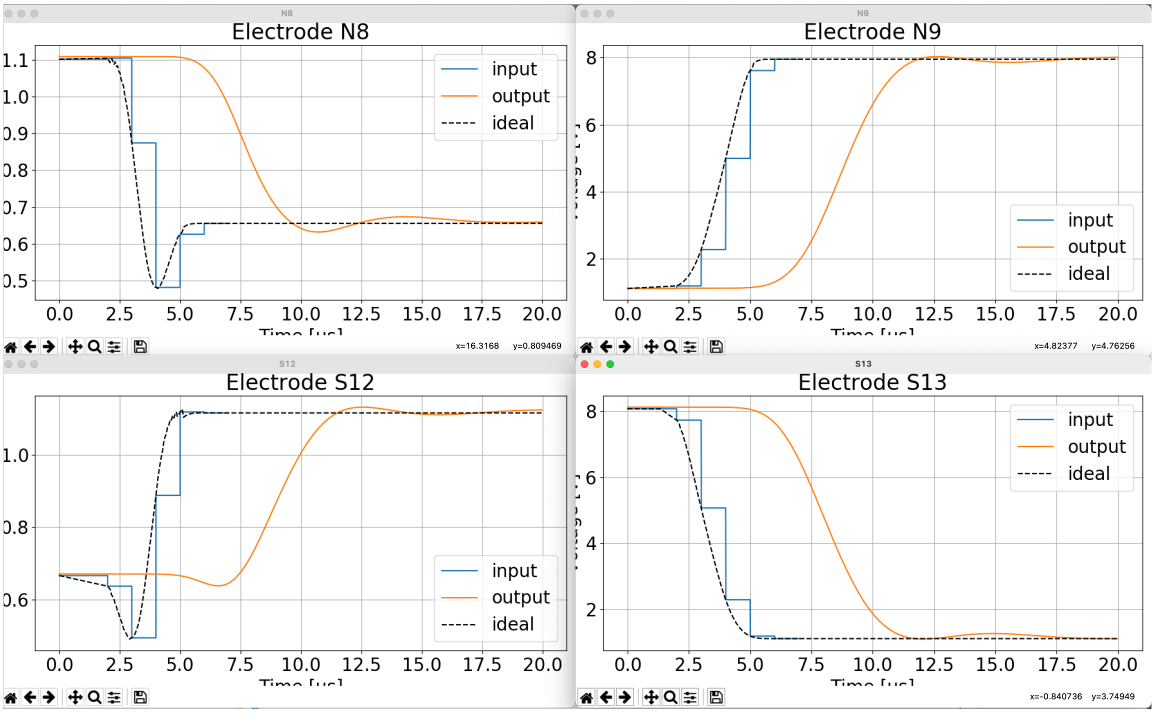

Figure 5-5: Naively sampled voltages. DAC update rate of 1000ns.

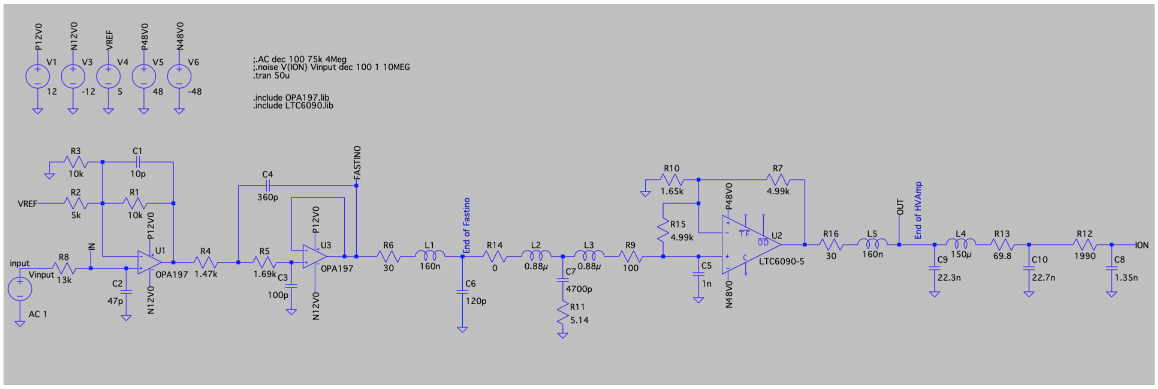

```
;.AC dec 100 75k 4Meg
;.noise V(ION) Vinput dec 100 1 10MEG
.tran 50u

.include OPA197.lib
.include LTC6090.lib
```

P12V0
N12V0
VREF
P48V0
N48V0
V1
12
V3
-12
V4
5
V5
48
V6
-48
R3
10k
C1
10p
R2
5k
R1
10k
VREF
IN
input
Vinput
R8
13k
AC 1
C2
47p
U1
OPA197
R4
1.47k
C4
360p
FASTINO
R5
1.69k
C3
100p
U3
OPA197
R6
30
L1
160n
End of Fastino
C6
120p
R14
0
L2
0.88μ
C7
4700p
R11
5.14
L3
0.88μ
R9
100
R10
1.65k
R15
4.99k
C5
1n
R7
4.99k
U2
TF
OD
C
LTC6090-5
R16
30
L5
160n
OUT
End of HVAmp
C9
22.3n
L4
150μ
R13
69.8
C10
22.7n
R12
1990
C8
1.35n
ION

Figure 5-6: Schematic of our circuitry in LTSpice. Our DAC inputs are modelled as piecewise linear functions applied at "Vinput". The stages "End of Fastino" and "End of HVamp" and labeled. The voltage output at "ION" is our expected electrode voltage.

5.2 Deconvolution

We have a comprehensive of our system's circuitry 5-6, and thus we should be able to find close to optimal inputs to achieve the target waveforms. I simulate a step response of our circuit by applying a 0 V to 1 V input from our DAC model. The derivative of the output step response is the impulse response of our circuit, shown in 5-7.

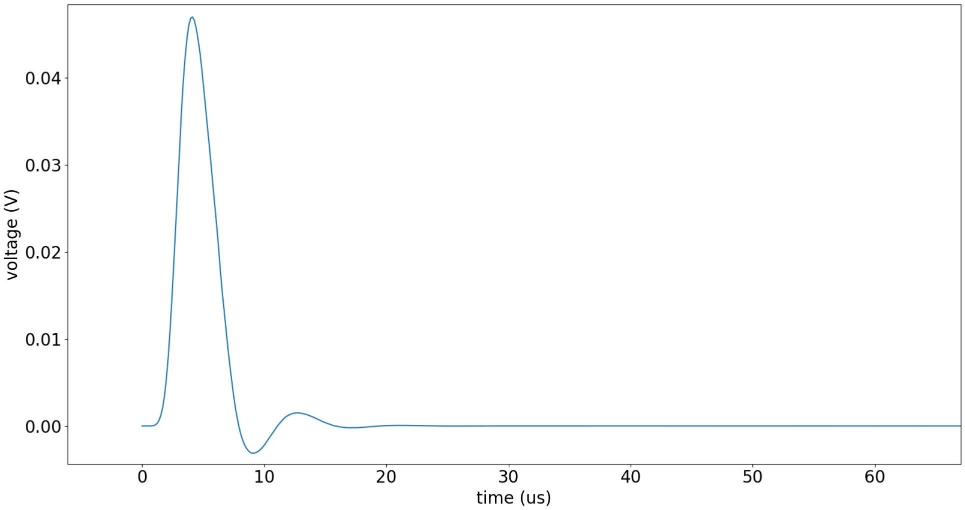

Figure 5-7: Impulse response of our electrode circuitry.

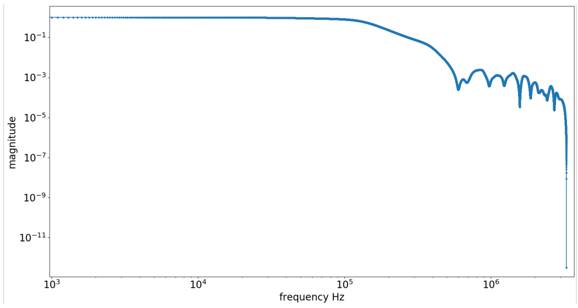

Figure 5-8: Magnitude of the transfer function

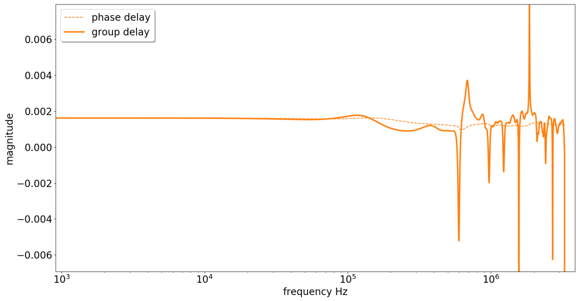

Figure 5-9: Phase of the transfer function. Phase delay: $\frac{\phi}{f}$. Group delay: $\frac{\mathrm{d}\phi}{\mathrm{d}f}$

I then calculate the FFT of the impulse response, to get the system's transfer function. The magnitude of the transfer function is shown in 5-8 and the phase delay and group delay are shown in 5-9. The transfer function calculated from the impulse has been compared with the transfer function obtained from a SPICE .AC analysis, with great agreement.

Using our electrode circuit transfer function, shown in 5-8, we can deconvolve the spectra of our target waveform $Y(f)$ with our system transfer function $H(f)$ using Wiener deconvolution,

$$\hat{X}(f) = \frac{1}{H(f)} \left[\frac{1}{1 + \frac{1}{|H(f)|^2 \, \mathrm{SNR}(f)}} \right] Y(f) \tag{5.2}$$

where $\hat{X}(f)$ is the Fourier transform of our desired input signal, and $\mathrm{SNR}(f) = S(f)/N(f)$ is the signal-to-noise ratio of the original signal $\hat{X}(f)$.

$H(f)$ becomes quite small at high frequencies (∼1 MHz), which can lead to the deconvolved input being dominated by high frequency oscillations. To protect $\hat{X}(f)$ from blowing up at higher frequencies, we introduce the $\mathrm{SNR}(f)$ term in the denominator to increase $H(f)$ when it is small. $\mathrm{SNR}(f)$ of our input waveform is realistically large at small frequencies, allowing the denominator of (5.2) to be dominated by $H(f)$. At higher frequencies, we expect that both $H(f)$ and $\mathrm{SNR}(f)$ decrease, regulating the denominator at reasonable levels. Currently, I heuristically estimate SNR(f) to be three different values,

$$\begin{cases} 1\times10^6 & f \leq 120\text{kHz} \\ 500 & 120\text{kHz} < f \leq 360\text{kHz} \\ 10 & 360\text{kHz} < f \end{cases} \tag{5.3}$$

The target waveform for electrode N9 in 5-3 is deconvolved with the circuit transfer function 5-8 using Wiener deconvolution (5.2) and plotted in Fig 5-10. Note that since the target waveform only lasts 5 μs, I have chosen to mirror the signal and add a 300 μs buffer at the beginning and ends, in order to extend the waveform signal and make it periodic, with the goal of increasing the resolution of its Fourier transform.

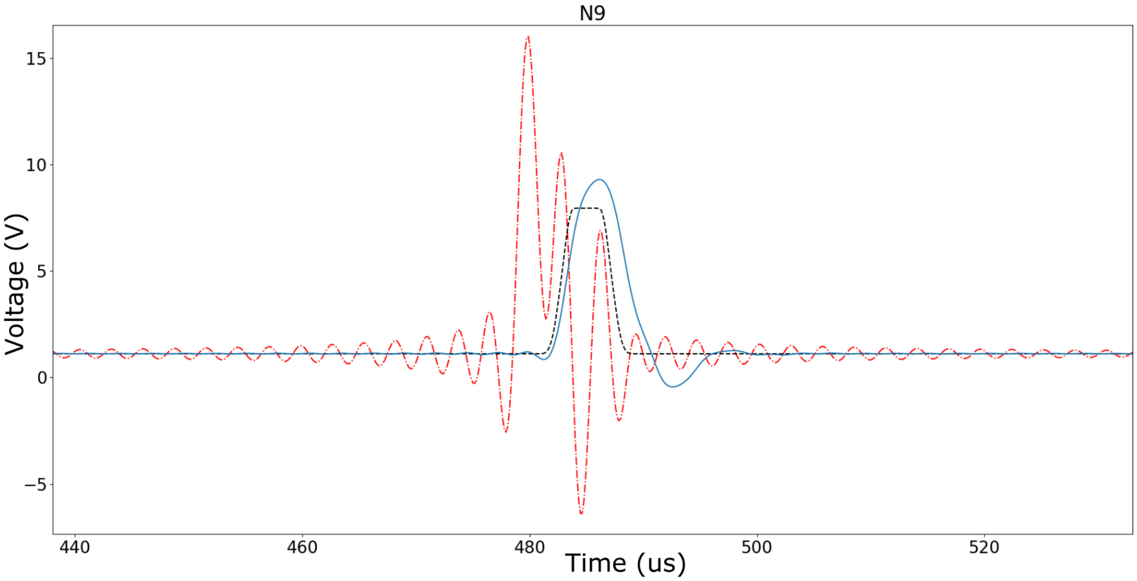

Figure 5-10: Deconvolved signal (red) of the target waveform for electrode N9 (black). The analog output of the deconvolved signal is simulated in SPICE (blue).

The deconvolved signal is a larger amplitude pulse that occurs before the signal, which is what we were expecting. However, running the deconvolved signal through SPICE gives an output that does not completely match the target waveform. I have found that time-domain simulations in SPICE do not perfectly match multiplication in frequency domain when non-linear components are involved (such as the op-amps in our high-voltage amplifier). Otherwise, with purely passive RLC components, I have found time-domain simulations to strongly agree with transfer function convolution.

Perhaps a more robust estimate of our input signal-to-noise-ratio SNR(f) would lead to better results in deconvolution. However, it is not a deal-breaker that the deconvolved signal is not perfect, because we would not be able to input such an analog signal to our system anyway.

5.3 Local Minimization

Once again, we are limited by the update rate of our DACs and thus must sample the deconvolved signal. Naturally this will introduce more errors in our waveforms. However if we assume the deconvolved signal is close enough to the globally optimal input waveform, then sampling the deconvolved signal should still get us closer to the optimal inputs compared to sampling the target waveform. A local optimization cycle may be enough to get us within the basin of the global minimum.

As compared to sampling the target waveform, which distorts and delays the voltage signals, sampling the deconvolved waveform removes the time delay but still results in a distorted waveforms, usually showing up as an oscillation towards the end 5-11.

We then wrap the waveform error into a cost function [1] and run a local optimization cycle based on SciPy's Sequential Least Squares Quadratic Programming algorithm to better match the target waveforms.

The initial guess to the optimization cycle is the sampled deconvolved signal (shown in blue in Fig 5-11, which I believe to be close enough to the globally optimal input waveform that a local minimization will find these optimal inputs. The optimization cycle takes on average a couple hours to run, finishing with

---

[1] Cost function engineering is a future path line of work. There are various things you can put in this cost function.

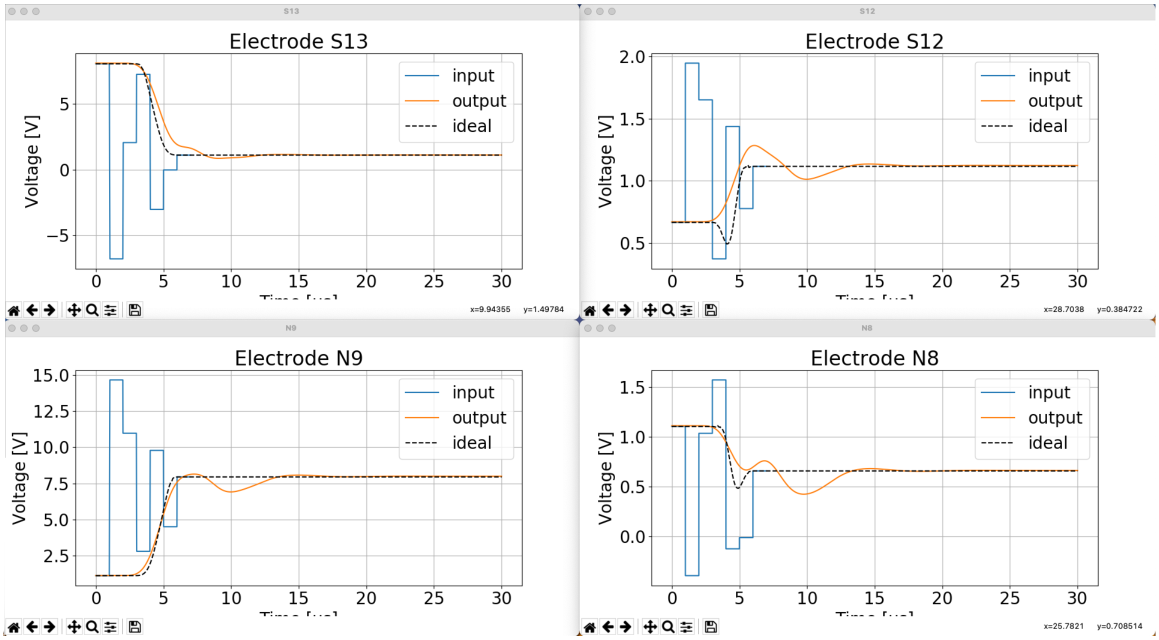

Figure 5-11: Sampling the deconvolved signal. Time (μs) plotted on the x-axis. The timing of the voltages are better than the naive voltages, but there's uncontrolled oscillations at the end.

around a couple thousand SPICE simulations to evaluate the cost function.

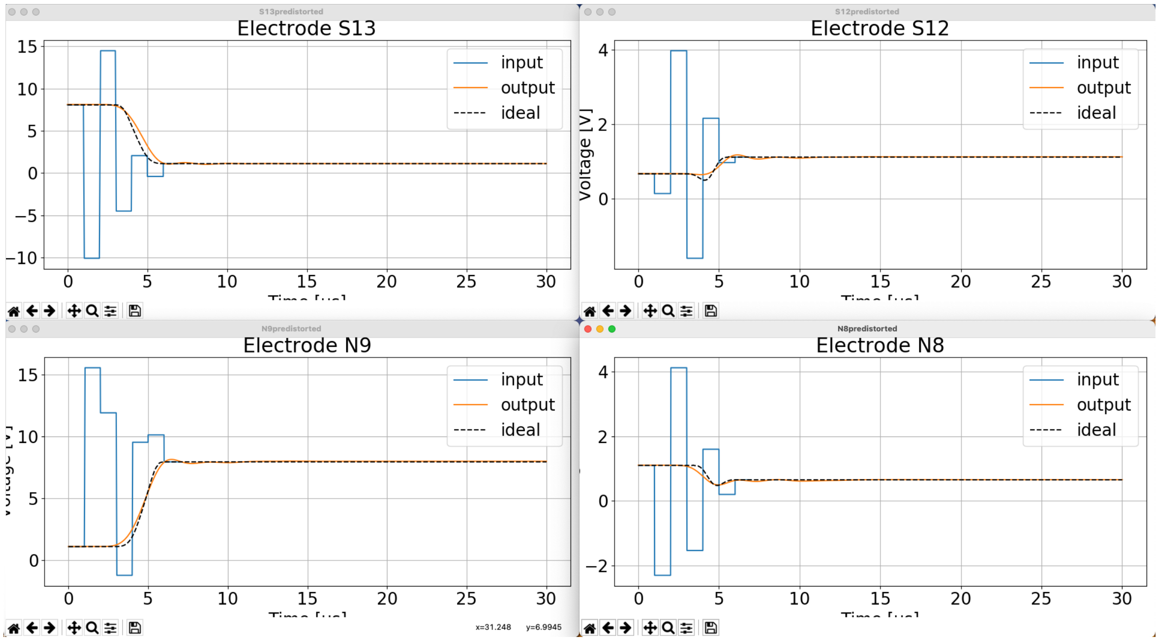

Figure 5-12: After an optimization cycle. Time (μs) plotted on the x-axis. Smooths out the ending oscillations to better match the target waveform.

The output of the optimization cycle is shown in 5-12. Compared with the sampled deconovlved signal, output waveforms from the optimized inputs do not have large oscillations at the end. The optimal inputs are highly variable and larger in amplitude than the target waveform, with multiple swings between positive and negative voltages. This is intuitively reasonable since we must really drive our circuitry to overcome the low-pass filtering effects. It is previously thought that bang-bang protocols (using only two voltage sets: one at the first position, and the second at the ending position) are the fastest we can run ion transport [19]. However voltage waveforms for a bang-bang would be heavily filtered, regardless of how fast the DAC update rate is, and end up at the mercy of the circuit's natural step response. Thus we see here that my method of predistortion leads to large driving inputs that allow us to actually achieve waveforms that are faster than bang-bang protocols.

A couple remarks about this predistortion method. Because we are predistorting in the time-domain, rather than using analytical transfer functions, we need to be sure that our SPICE model matches our physical circuit as accurately as possible. Our predistorted inputs tend to drive our circuit extra hard, meaning that we are more sensitive to inaccuracies in our circuit modelling. There is no other way to ensure this besides making measurements of the predistorted waveforms and comparing with simulations.

While this deconvolution plus local optimization technique can bring us closer to the ideal inputs than just deconvolution or local optimization alone, there is still no guarantee that the predistorted inputs are globally optimal. Future optimization techniques could include more powerful global optimization algorithms (e.g. genetic algorithms, basin hopping), training a neural network to learn the system's dynamics, and cost function engineering. While our evaluations of our cost functions are purely done in simulation, having the ability to incorporate experimentally measured data (e.g. voltage measurements or even ion motion experimental measurements) may prove to result in waveforms that are inherently robust to experimental noise sources that are not included in simulation [73].

Chapter 6

Experimental Results

In this chapter I will present the experimental efforts on the trapped-ion apparatus at both the MIT Research Lab of Electronics and MIT Lincoln Laboratory. First, I characterize our electrode circuitry by systematically measuring the step response of each stage and compare with our model simulated in SPICE. Then, I present successful diabatic ion transport on the MaxBeta trap and compare the measured predistorted waveforms with my simulations. Next I discuss the spectroscopy data of two ^{40}Ca ions taken during the splitting waveforms 5-2, applied frame by frame. Finally, I detail a potential advantage of our MaxBeta trap for precisely controlling the positions of ions in a chain. These efforts to comprehensively characterize electrode circuitry, evaluate applied voltages for optimal transport and splitting, and simulating precise potentials on the MaxBeta trap are all necessary steps towards achieving rigorous voltage control of trapped-ions. Further work remains to be done in this direction in order to reliably achieve optimal shuttling on surface electrode traps.

6.1 Electrode Circuitry Characterization

An accurate model of our system's electrode circuitry is necessary when applying voltage waveforms that push the speed of our DACs and amplifiers. Our method for predistorting waveforms to account for filtering uses many time-domain sim-

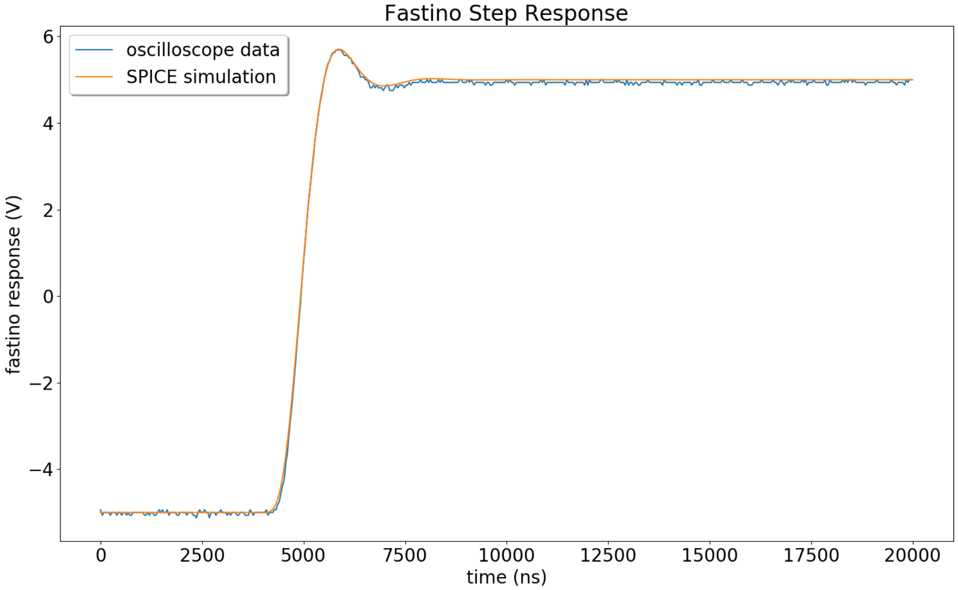

Figure 6-1: The output of the Fastino with a 0 to 2.5 V step input. The cable from the HD68 Fastino connector and the oscilloscope was modelled as a 100 pF parasitic capacitor.

ulations of our circuit modelled in SPICE. Certainly the better our SPICE model predicts voltage outputs, the more confidence we can have that our predisorted inputs will act favorably on our ions. From SPICE libraries, we have imported the models for all the integrated circuits (ICs) in our system and have simulated all the stages from the discrete inputs into the Fastino to the DB25 connectors that feed into the trap electrodes.

The last requirement is to compare our SPICE simulations with voltage responses measured in the lab, which we have done stage by stage. The first stage of our electrode circuitry is the Fastino circuit that amplifies the DAC inputs to a ±10 V output. We measure the Fastino output after applying a step input from the DAC and compare with the predicted step response from our SPICE model 6-1. The data and simulation match well and we move onto the next stage, which is the high-voltage amplifier.

Then we connect the high-voltage amplifier to the Fastino and measure a step response in a similar fashion 6-2.

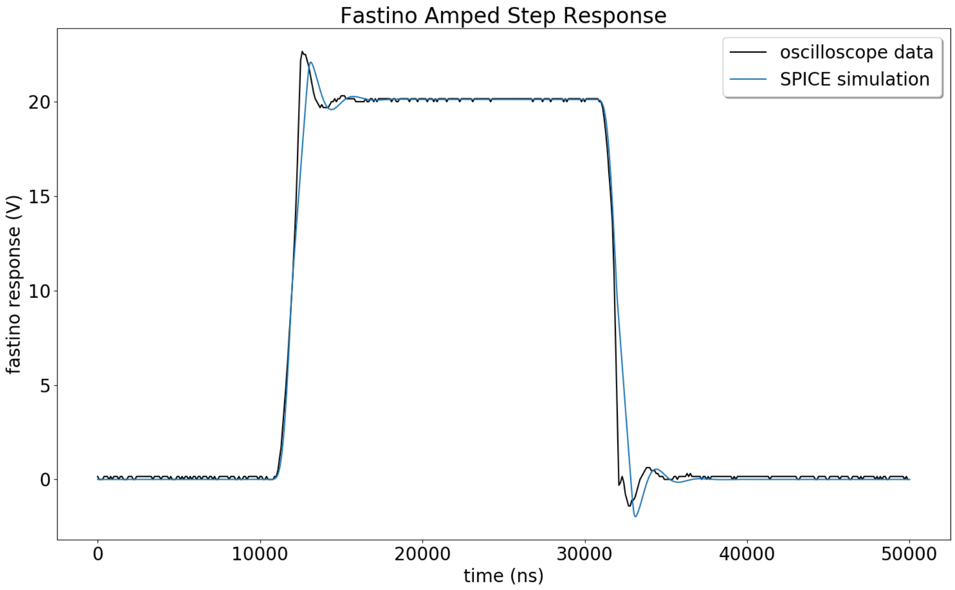

Figure 6-2: Fastino + HVamp output with 2.5 to 5 V and 5 to 2.5 V input steps.

From the measured data, we observe that the amplifier circuit actually had a higher slew than rate than predicted from the SPICE model. To account for this extra slew, a small change was needed in the model of the LTC6090-5 op amp in the high-voltage amplifier circuit. Increasing the transconductance parameter, Kp, of two vertical double diffused power MOSFETs by 100 mA/V^2 in the LTC6090-5 model accounted for this increase in slew.

The rest of the stages of the circuit consists of two passive low-pass filters built with linear R, L, C components only. Most of the components are well-known, except for the NFE61PT472C1H9L electromagnetic interference (EMI) filter. This component is listed as a third-order T-type low-pass filter with capacitance of 4.7 nF and two inductors of an unspecified value 6-3. To determine these values, I powered EMI filter component by itself with a Agilent 33250A function generator and measured the transfer function with a Tektronix TDS 2024C oscilloscope. Since the transfer function of this filter topology is analytically well-known, I was able to fit the analytical transfer function to the measured data to determine an inductance of $L = 0.878 \pm 0.005\ \mu$H and a resistance of $R = 5.14 \pm 0.10\Omega$ 6-4.

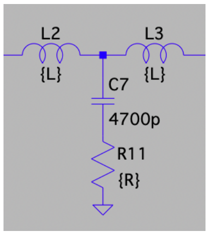

Figure 6-3: Circuit model for the EMI filter.

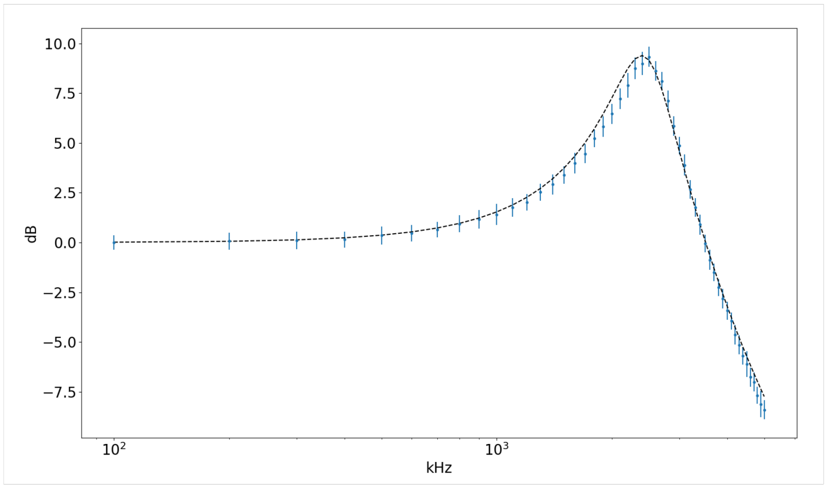

Figure 6-4: The fitted transfer function is shown in dotted black and the measured data points is shown in blue. The χ^2-probability is 98%.

The final step response of the entire circuit with our modified values is shown in Fig 6-5.

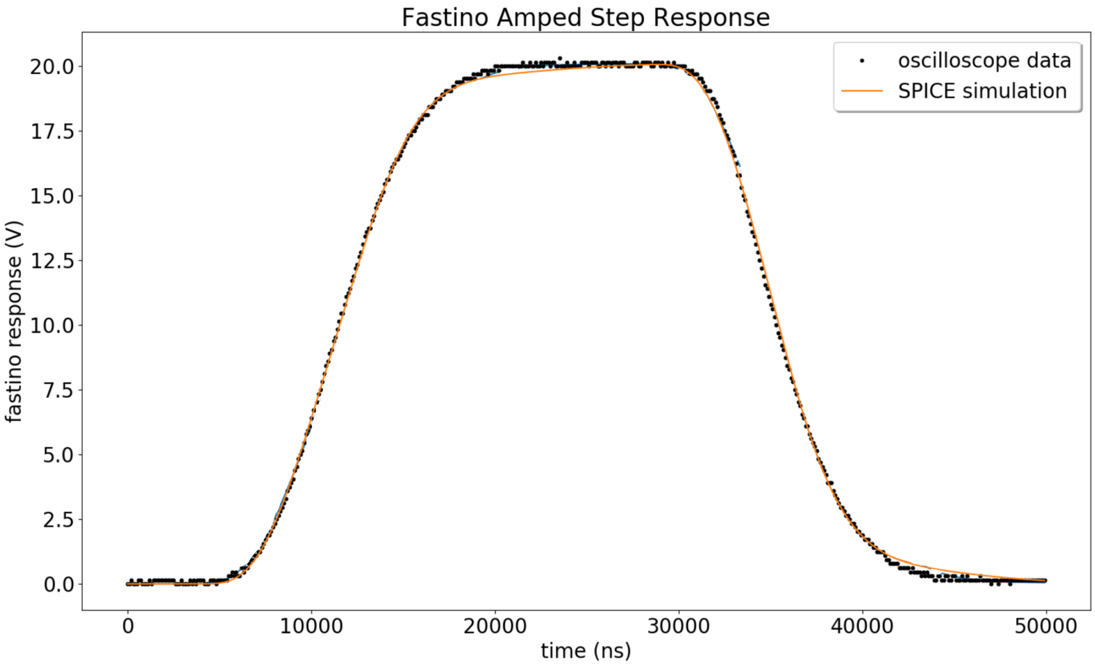

Figure 6-5: Full circuit output with output with 2.5 to 5 V and 5 to 2.5 V input steps.

6.2 Diabatic Ion Transport

We now investigate diabatic transport on the MaxBeta trap. Due to the inner segmented electrode geometry, the MaxBeta trap can easily provide a strong axial confinement, which we have shown to be quite advantageous for fast ion transport in chapter 4.

We courageously try a bang-bang protocol by very coarsely sampling the transport waveforms in Fig 5-1. We start the ^{40}Ca ion at the center of electrode S12 (corresponding to an axial position of 186.5 μm (2-4)) using the first voltage set. Then we apply the very last voltage set, corresponding to harmonic trap at the center of the next electrode (231.5 μm), and let the electrode filters + ion do its thing. We then transport the ion back to the starting position using slower transport waveforms that we have tested to lead to no motional excitation.

Remarkably, measuring the ion's motion with sideband spectroscopy after transport resulted in a motional excitation that is consistent with zero quanta[1]. This bang-bang transport demonstration shows that our ion is protected by electrode filtering and a high axial frequency. The filtering allows voltage waveforms to respond smoothly and the high axial confinement keeps the imperfect controls from exciting the ion. The transport trajectory certainly did not follow the intended STA protocol ((4.23)) because we let the electrode filters respond naturally, but the deviation in transport, δq, was not large enough to excite the ion. With a DAC update rate of $dt = 1000$ ns, we would hope that a bang-bang protocol would finish in 2 μs. However, with Mr. Jules Stuart's transport verification scheme, we were able to observe that it took around 15 μs for the ion to be transported, which is reasonable given our low-pass filtering.

In hopes of transporting faster than the natural step response of our circuitry, we predistort the transport waveforms 5-1 using my predistortion method described in chapter 5. We also push Fastino to its speed limit by finding predistorted inputs for update rates of 1000 ns, 800 ns, and 600 ns. Stuart measured the

---

[1] The smallest nonzero excitation we can measure is actually 0.2 quanta

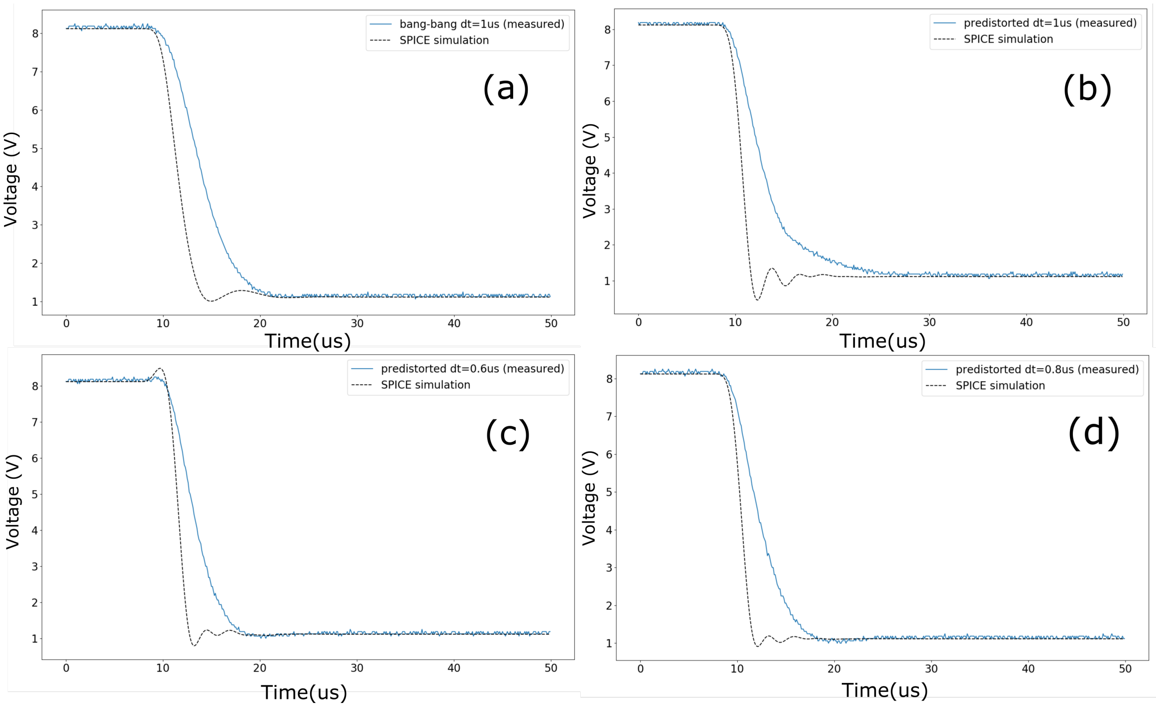

Figure 6-6: Measurements of S13 waveform (blue) and simulated waveform (dashed black). (a) bang-bang (b) predistorted dt = 1000 ns (c) predistorted dt = 600 ns (d) predistorted dt = 800 ns.

resulting waveforms with an oscilloscope and observed timing issues that lead to inconsistent triggering. These timing issues are believed to be caused by a bug in the ARTIQ system and will be investigated further. Although the ion appeared to have been successfully transported, it is hard to make any strong claims to the transport excitation due to the inconsistent timing.

Mr. Jules Stuart was able to measure the waveform on electrode S13 for the three update rates despite the timing issues and I compare them with the expected waveform simulated in SPICE, shown in Fig 6-6. Turns out that the measured waveforms were significantly slower than expected. Parasitic capacitance from cabling and measuring apparatuses were added to the model but no change in the linear RLC components could account for a discrepancy this large.

Since the waveforms had timing issues, I decided instead to analyze the model of our DAC inputs. The specifications of the AD5542 IC in the Fastino model report a 1 μs settling time and an output impedance of 6.25 kΩ. We've previously

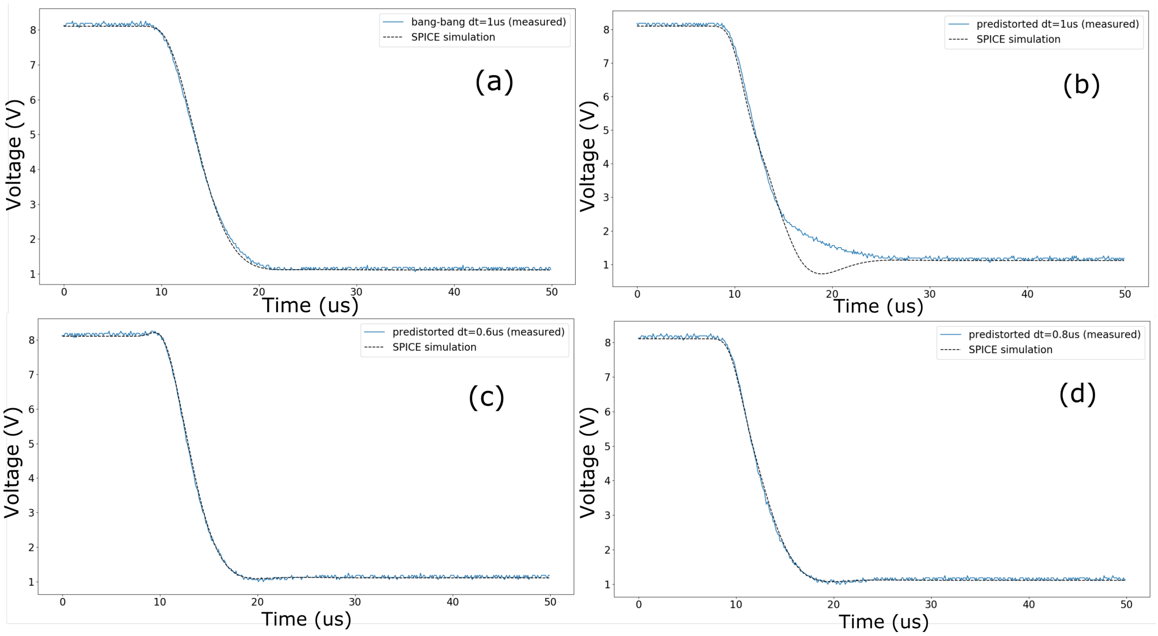

Figure 6-7: Measured waveform (blue) and simulated waveform (dashed black) for electrode S13 with an adjusted DAC model. (a) bang-bang (b) predistorted dt = 1000 ns (c) predistorted dt = 600 ns (d) predistorted dt = 800 ns.

modelled this chip as a piece-wise linear input, `Vinput`, in series with a 6.25 kΩ resistor, `R8`, 5-6. Due to fast update rates below 1 μs and the observed timing issues, both the piece-wise linear model and the value of `R8` could be off.

I doubled the value of `R8` to 13 kΩ, which led to a much stronger agreement between simulated and measured waveforms in Fig 6-7. Note that the agreement for the predistorted waveform with $dt = 1000$ ns is great up until a point 6-7(b). I was able to explain this behavior by simulating a large 40 V glitch at the beginning of sixth voltage update. Also, to get the agreement between simulation and measurement for bang-bang waveform, 6-7(a), I had to change the value of `R8` to 25 kΩ instead.

This characterization of diabatic transport waveforms suggests that a stronger model of our DACs is needed. While our previous characterization of our circuit used a single step response, we are now driving our DACs essentially at their speed limit, and our waveform outputs have shown to be sensitive to our DAC timing. It is still unexplained why the `R8` value changes when we perform voltage steps in quick succession, what is causing the glitch behavior in 6-7(b), and how well our piece-wise linear model describes the DAC. These questions may be answered by measuring the output of the AD5542 chip in the Fastino directly during these transport waveforms. While we have statically characterized our circuit in the previous section, we now must characterize the circuit during fast dynamical changes.

We have demonstrated that even without a perfect model of our circuit dynamics, we can be confident that our transport operations will end up cold. A large axial frequency during transport can ensure that ions will be minimally excited during transport. However, to drive the waveforms faster than the filtering cutoffs, we must predistort the waveforms with an accurate *dynamical* model of the circuit. Future characterizing of the DACs during waveform updates is needed to ensure that cold transport is also as fast as we would expect.

6.3 Splitting Spectroscopy

The maximum β value that our MaxBeta trap is poised to create has never been demonstrated before. As such, we are in uncharted territory and it is important to carefully characterize these strong quartic potentials and their effects on ion crystals. To do this, we slowly step through the optimal splitting waveforms in the previous chapter, 5-2, and measure ion spectroscopy to determine the axial mode frequencies throughout the split. The results of sideband spectroscopy is shown in Fig 6-8.

By taking the difference in the corresponding sidebands at each index, we may plot the COM and stretch frequencies as a function of the index. The expected frequencies from our splitting waveforms is also plotted in 6-9. At first glance it is obvious that we do not have the level of control during our splitting operation that we would like. Furthermore, we hope that the COM frequency during the split stays constant (for optimal splitting) rather than varying over a couple hundred kHz like we measure. It is also interesting that the measured stretch and COM mode frequencies essentially remain separated by a factor of $\sqrt{3}$ while we should

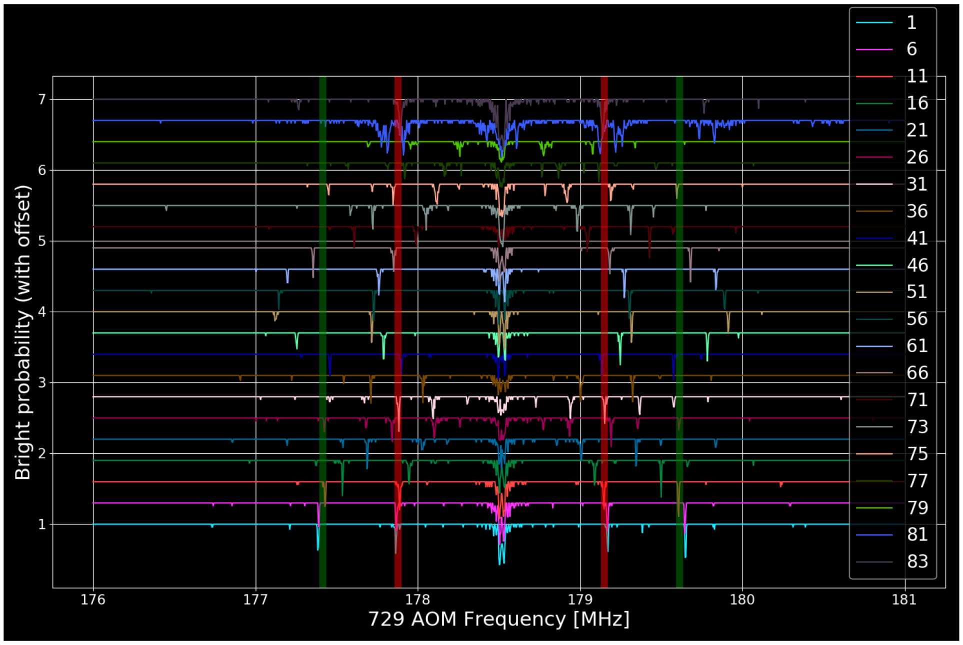

Figure 6-8: Sideband data during a slow motion split. Each horizontal trace is a different index of the splitting waveform, starting with index 1 at the bottom and reaching index 83 at the top. The difference between the two sideband peaks gives the mode frequency. The vertical bars shows the expected sideband location for a COM frequency of 1.2 MHz (red) and a stretch frequency of 2.1 MHz (green).

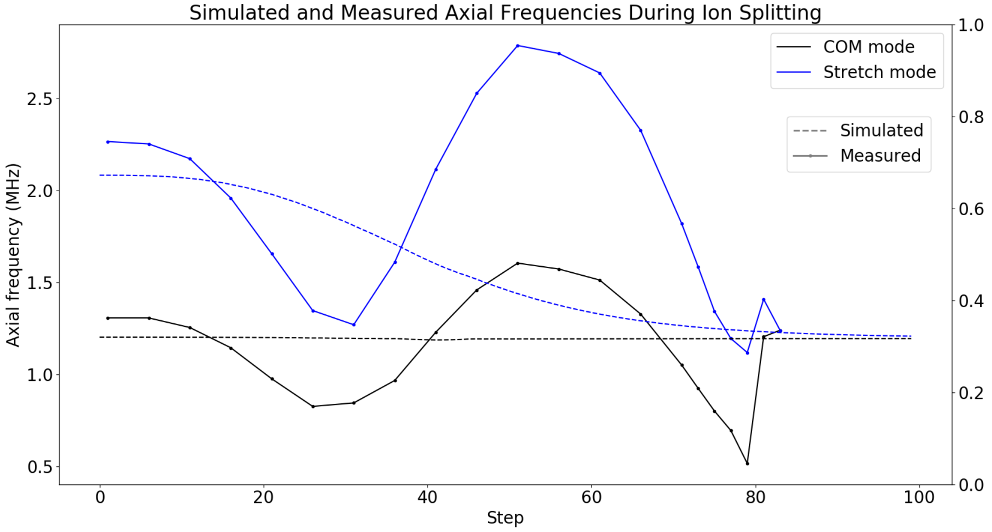

Figure 6-9: Expected and measured axial frequencies during a slow motion split.

N21	N20	N19	N14	N13	N12	N11	N10	N9	N8	N4	N3	N2	N1
0	0	0	0	0	0	0	0	-0.14	-0.14	0	0	0	0

S1	S2	S3	S4	S8	S9	S10	S11	S12	S13	S14	S19	S20	S21
0	0	0	0	0	0	0	0.45	0.07	0.45	0	0	0	0

Table 6.1: Voltages for $E_z = 1$ V/cm on the MaxBeta, applied at a position of $(x, y, z) = (0, 186.5, 50)$ μm. Electrode names correspond to positions in Fig 2-4.

expect that these two modes converge as the ions move apart. This suggests that there are experimental errors that cause the potential to remain as a single harmonic well throughout the split, rather than transforming into a double well.

The critical point of our split (where β reaches its maximum value) occurs around index 40. This is also when we are driving our electrodes the most by applying +40 V on two electrodes. Thus there will likely be strong electric fields in the $\hat{z}$ direction. We may solve for the voltage sets that lead to a z-field of 1 V/cm at the center of the split (186.5 μm)). Such a voltage set is shown in Table 6.1.

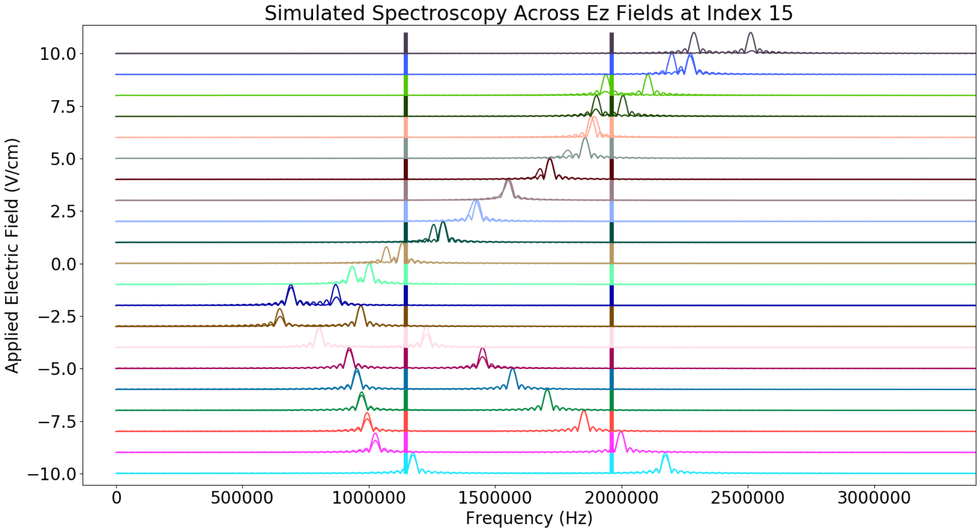

Figure 6-10: Simulated spectroscopy after adding various Ez fields, shown on the y-axis. The vertical bars show the experimentally measured frequencies at index 15. Based on this scan, an optimal E_z field is ~9.5 V/cm

For each index, we may figure out the proper amount of E_z field to add in order to explain our spectroscopy data. I scan over a large range of E_z at each index, and for every E_z value, I add the corresponding voltage set in Table 6.1 to obtain a new adjusted voltage set. I then calculate the resulting potential using (3.3), run my ODE solver with two ^{40}Ca ions, take the FFT of the oscillation in the adjusted potential, and plot the resulting spectrum in Fig 6-10.

Fig 6-10 shows the manual tuning process for a single potential during the splitting (index 15). The added E_z field is shown along the y-axis, with each corresponding horizontal plot showing the peaks of the mode frequencies calculated with my ODE solver. The two vertical bars correspond to the measured mode frequencies at index 15. For this specific example, the simulated modes best match the measured modes when $E_z \approx 9.5$ V/cm.

After repeating this tuning process for every index, we can now plot the optimal E_z field to add at each index in order to match the measured spectroscopy data with simulation, shown in Fig 6-11a. While the reason to require such a E_z correction is still unknown, it is interesting that E_z reaches a maximum magnitude near the critical point of the split, suggesting that the ion crystal is not very well behaved with +40 V electrodes. Furthermore, the shape of the optimal z-field seems to mirror the behavior of the β-term during this splitting protocol. This might be because when β is large, larger voltages on the electrodes are required, but larger electrode voltages may drive the ions in unpredicted ways. A z-shim up to 10 V/cm is not out of the ordinary for standard control of ions in surface traps, however a −70 V/cm z-shim is quite large. Further work remains to be done in understanding the mechanism behind this E_z behavior.

To actually apply the optimal E_z field in my simulations, I must add the corresponding voltage set in Table 6.1, thereby adjusting the voltage set at every index. The new voltage set is closer to what the ions actually "felt" during the split, a so-called "effective" voltage. The effective voltage is plotted in 6-11b.

It is interesting to note in 6-11b that the effective voltages qualitatively look like the applied splitting voltages in Fig 5-2, except the effective voltages are much smaller in magnitude. This suggests that although we have supplied +40 V to

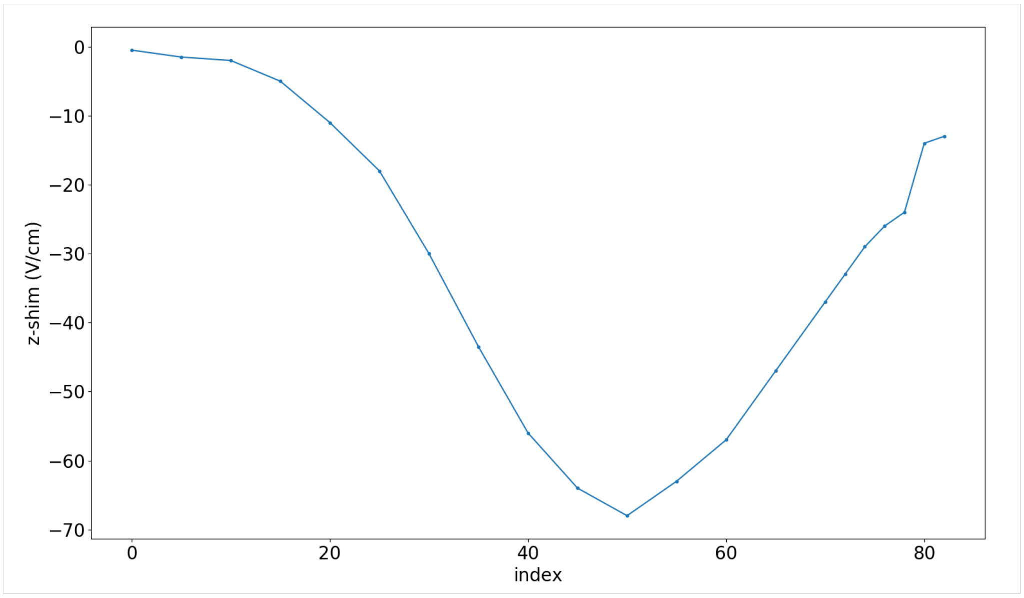

(a) Added E_z field to qualitatively account for the measured spectroscopy.

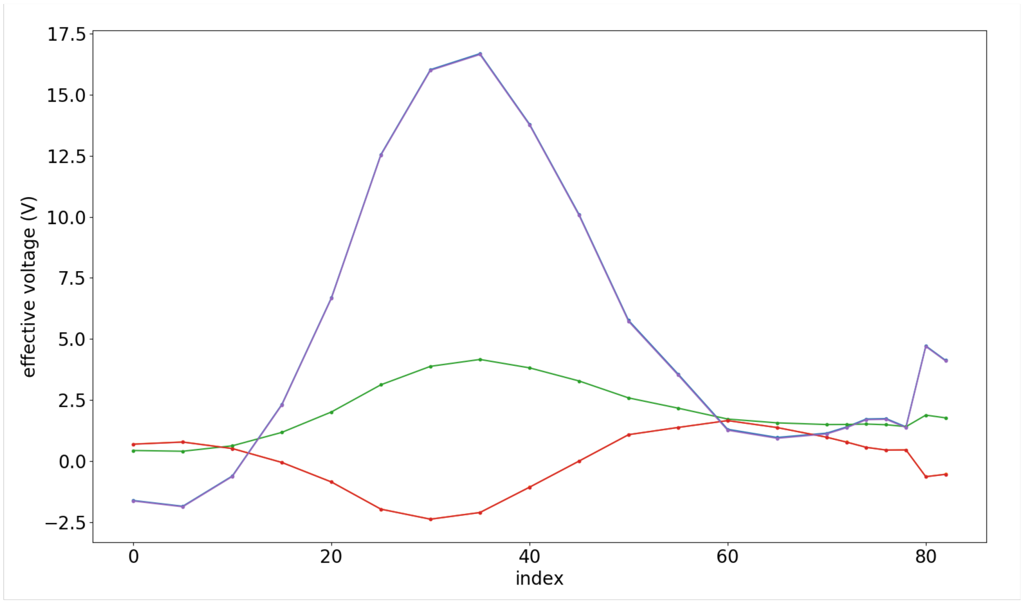

(b) Voltages on electrodes {N8, N9, S11, S12, S13} after adding the optimal *Ez* field.

Figure 6-11: Spectroscopy tuning

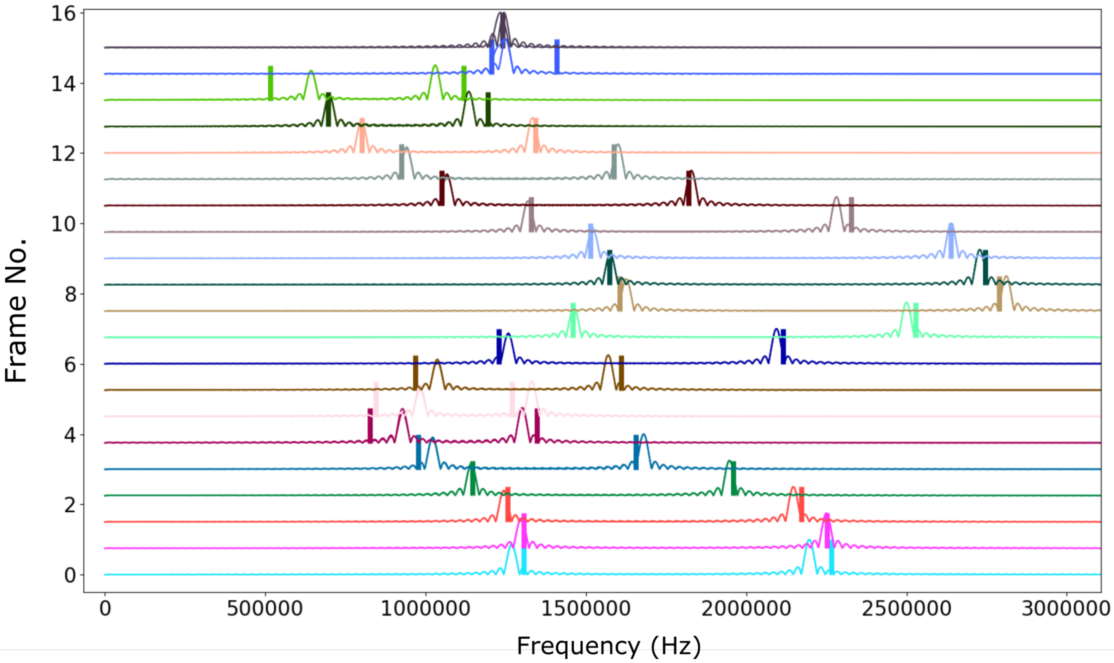

Figure 6-12: Simulated spectroscopy with measured data overlaid. The bars show the measured data. Each horizontal trace represents a different time step along the split, with index 0 at the bottom and index 83 at the very top.

our trap electrodes at the critical point, the ions have only "felt" +17 V. Again, the reason behind this discrepancy is not well understood, but I have some possible hypotheses. Perhaps the large positive voltages push the ion away in the $\hat{z}$ direction, where it feels a smaller effective axial potential at the new z-position. Another suggestion could be due to a decrease in stability as the large values on DC electrodes reduce the confinement in the radial directions. A third possibility could be due to the fact that the ion crystal orientation may no longer be guaranteed to lie along the axial direction, which would drastically affect the frequencies we measure with sideband spectroscopy.

We now have a possible model for the discrepancy between our experimentally measured and simulated spectroscopy. I then overlay the simulated spectroscopy adjusted with the optimal E_z field, shown in 6-12.

While simulations have helped to begin explain the measured spectroscopy of our split, the exact underlying mechanism is still unknown. Future work remains to identify and also correct for sources of this discrepancy. Once this is satisfactorily understood and controlled, we can then work on speeding up the splitting experiment, with the ultimate goal of achieving a cold split in the faster-than-adiabatic regime.

6.4 Equally-Spaced Ion Chains

Besides a large quartic confinement, another advantage of the MaxBeta trap's finely pitched electrode layout (45 μm on the smaller electrodes) is the ability to create potentials that are highly variable in space. By alternating positive and negative voltages on neighboring electrodes, one can create a potential that mimics a lattice potential 6-13.

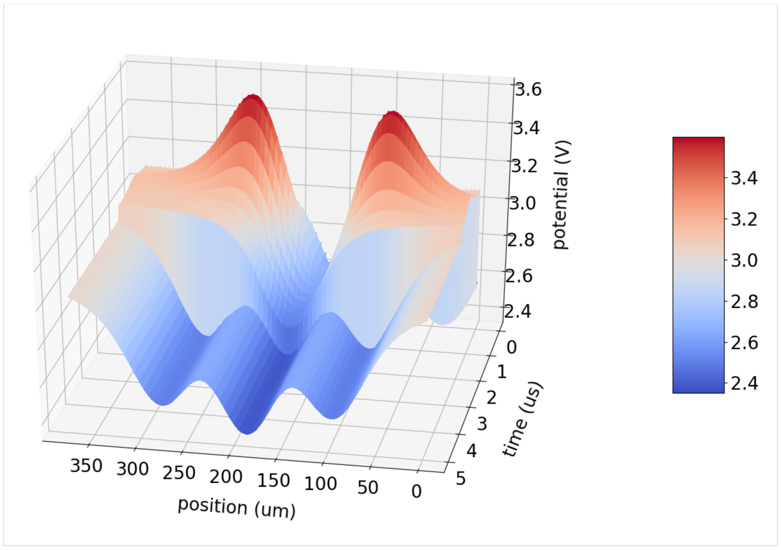

Figure 6-13: Funky potential on the MaxBeta!

This enhanced control of potential shapes can perhaps be more usefully utilized to engineer quartic potentials with a flat bottom, in order to hold ions in a chain at equally spaced intervals. I wrote an optimizer in SciPy that performs a local search for α and β parameters that lead to an equally spaced equilibrium position for a chain of N ions. To calculate the ion chain's equilibrium positions, I minimize the total potential energy of the chain given by,

$$U(\vec{x}) = \sum_{i}^{N} q_i \left(\alpha x_i^2 + \beta x_i^4 + \sum_{j \neq i} \frac{1}{4\pi\epsilon_0} \frac{q_j}{|x_j - x_i|} \right) \tag{6.1}$$

Where the potential energy, U, reaches a minimum at the equilibrium configuration, $\vec{x}^{(0)} = \begin{bmatrix} x_1^{(0)} & x_2^{(0)} & \dots & x_N^{(0)} \end{bmatrix}$. The spacing between neighboring ions in the equilibrium configuration, $\vec{x}^{(0)}$, is compared to the target spacing and the cost function is the squared error of the spacing.

I performed this search on a 4-, 5-, and 9-ion chain of ^{40}Ca spaced by 5 μm. A summary of the results can be seen in Table 6.2. Note that by tuning just two parameters we can accurately space a 5-ion chain, but not a 9-ion chain. Perhaps by allowing for higher-order potential shapes beyond 4th order can allow one more finely tune the 9-ion case.

N	α (V/m^2)	$\omega_0$$^{\mathbf{a}}$ (kHz)	β (V/m^4)	$\beta/\beta_0$$^{\mathbf{b}}$	inter-ion spacing (μm)
4	2.588×10^{-6}	562	2.346×10^{-8}	0.12	5.000, 5.000, 5.000
5	1.407×10^{-6}	415	1.346×10^{-8}	0.07	5.000, 5.000, 5.000, 5.000
9	4.158×10^{-8}	71	2.617×10^{-9}	0.01	5.110, 4.865, 4.955, 5.083, 5.083, 4.955, 4.865, 5.110

Table 6.2: α and β values for a 4-, 5-, and 9-ion ^{40}Ca chain. $^{\mathbf{a}}$For a purely harmonic potential with an α value confines an ion at frequency $\omega_0 = \sqrt{2\alpha q/m}$. $^{\mathbf{b}}$The maximum beta value, β_0 on our trap is 2×10^{-7} V/m^4.

It is worth mentioning that I have not constrained the mode frequencies for these chains. As seen in the small values of α and β, that the externally applied field becomes smaller in magnitude to equally space a longer ion chain. Thus if the ions are too far spaced, their Coulomb interactions may not be enough to actually provide a strong enough confinement to keep the ions stable and shielded from environmental noise sources.

We solve for voltages to achieve the desired potential for the 4-ion chain case, shown in Table 6.3. Note that voltages are more or less symmetrical, as would be expected from a potential with purely even powers.

N21	N20	N19	N14	N13	N12	N11	N10	N9	N8	N4	N3	N2	N1
8	8	8	8	8	8	8	-16.22	-1.28	-1.36	-16.47	8	8	8

S1	S2	S3	S4	S8	S9	S10	S11	S12	S13	S14	S19	S20	S21
8	8	8	8	8	8	8	8.87	0.47	8.94	8	8	8	8

Table 6.3: Voltages for achieving a quartic potential to equally space four ^{40}Ca ions. Electrode names correspond to positions in Fig 2-4.

The simulated spectroscopy for four ^{40}Ca ions with the applied voltages in 6.3 is depicted in 6-14. The four axial modes have frequencies of 893 kHz, 1.536 MHz, 2.020 MHz, 2.332 MHz.

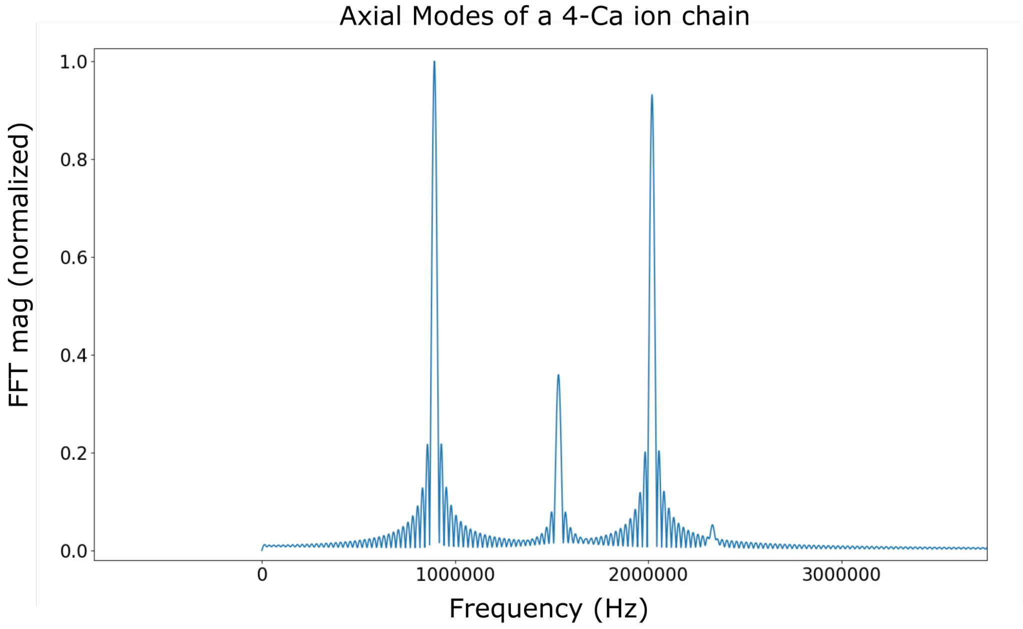

Figure 6-14: The frequency of the four axial modes in a chain of four ^{40}Ca ions spaced by 5 μm.

These voltages will hopefully be applied to the MaxBeta trap. We can more precisely engineering potentials by expanding to higher order terms, but finding voltages to constrain those potentials is trickier, because higher order corrections are typically smaller and thus harder to constrain. Further work remains to be done characterizing the sensitivity of the ion chain to stray fields and voltage errors.

6.5 Summary

The four experimental results presented in this chapter are all necessary efforts to achieve robust, diabatic transport and splitting. They each show the benefits of my numerical tools to better understand ion motion dynamics on surface electrode traps.

While static characterization of our circuit transfer function has been well demonstrated, the dynamics of our circuit during fast waveforms, especially the DACs, desire more investigation. Fortunately we have shown that we can reliably achieve cold ion transport on the MaxBeta trap, and we are positioned to push the limits of our circuit system to achieve faster-than-bang-bang transport.

Our splitting spectroscopy data shows that the MaxBeta trap is more than capable of producing strong confinement of two ^{40}Ca ions, which is highly advantageous for achieving fast and cold splitting. We are currently working towards understanding the sensitivities of the ions during a large quartic confinement and hope to be able to control the underlying mechanisms causing the variable axial mode frequencies. Only once this is well controlled, may we begin predistorting waveforms for fast splitting. As a by-product of understanding the large quartic potentials on our MaxBeta trap, we may possibly gain enough voltage control to precisely engineer potentials to keep long chains of ions equally spaced.

To achieve optimal shuttling operations on modern, scalable ion traps, I strongly recommend the use of rigorous and comprehensive simulations to first understand the effects of experimental imperfections on ion dynamics, and then work towards controlling them.

Chapter 7

Conclusion

The research questions tackled in this thesis reflects the state of modern trapped-ion quantum technologies. Ion trap quantum computers have grown beyond science experiments and are demanding serious considerations into their potential for large-scale quantum processing. The use of industrialized fabrication techniques, state-of-the-art integrated technologies, and collaborations outside academic groups have brought an engineering lens to trapped-ion research. A common goal for many engineers is to create robust systems and my work in this thesis has brought robustness questions to ion shuttling operations, which are likely to be crucial in future trapped-ion devices.

I present comprehensive simulations of ion shuttling experiments, from modelling our voltage controls to evaluating state-of-the-art ion shuttling theories. I bridge the gap between theory and experiment, by collaborating with Gonzalo Muga's theory group to consider realistic experimental noises, accurately characterizing our system's circuitry, and optimizing waveforms to achieve optimal shuttling protocols. My ODE solver has allowed me to identify key characteristics of optimal shuttling operations, which then I use to extend existing splitting methods beyond the state-of-the-art STA splitting protocol [53]. My work with numerical simulation tools, like ITVG, provide a deeper understanding of ion motion dynamics on surface traps by analyzing spectroscopy data of a slow motion split.

I have distilled the requirements for optimal shuttling operations into two criteria: tight and rigid axial confinement. While these criteria has been satisfied for ion transport, ion splitting remains a harder problem to solve. Achieving tight and rigid confinement during a splitting operation requires a custom-designed surface trap with an optimal electrode layout.

I present experiments on the MaxBeta trap towards achieving fast and cold ion splitting. While we show that our MaxBeta trap can indeed provide tight confinement during a split, future work remains in understanding and controlling the stray fields during a split.

Future work also remains to be done in incorporating closed loop feedback with simulation. Currently most ion shuttling operations are open loop, relying on the accuracy of our system models. Extending the cost function to include experimentally measured voltages, or training a machine learning model on ion motion data may help to account for experimental errors.

My ultimate vision in this field is for shuttling operations to be seamlessly and robustly integrated in quantum algorithms. While transport and splitting are the bread and butter operations, there is a need to control and operate on longer ion chains, and even mixed-species chains. Finally, ion shuttling does not have to be limited to transporting quantum information. There have been research and demonstrations of shuttling for fast entangling operations, logic gates, phase gates, and Fock state preparation [75, 15, 52, 66]. A central enabling tool to all the operations presented in this thesis are the simulation capabilities to improve our knowledge and control of the ion's motional dynamics in scalable surface electrode traps.

Bibliography

[1] C. H. Baldwin, B. J. Bjork, J. P. Gaebler, D. Hayes, and D. Stack. Subspace benchmarking high-fidelity entangling operations with trapped ions. *Phys. Rev. Research*, 2:013317, Mar 2020.

[2] C. J. Ballance, T. P. Harty, N. M. Linke, M. A. Sepiol, and D. M. Lucas. High-fidelity quantum logic gates using trapped-ion hyperfine qubits. *Phys. Rev. Lett.*, 117:060504, Aug 2016.

[3] Dana Joy Berkeland, J. D. Miller, J. Bergquist, W. Itano, and D. Wineland. Minimization of ion micromotion in a paul trap. 1998.

[4] R. B. Blakestad. *Transport of trapped-ion qubits within a scalable quantum processor*. PhD thesis, University of Colorado, 2010.

[5] R. B. Blakestad, C. Ospelkaus, A. P. VanDevender, J. M. Amini, J. Britton, D. Leibfried, and D. J. Wineland. High-fidelity transport of trapped-ion qubits through anx-junction trap array. *Physical Review Letters*, 102(15), Apr 2009.

[6] R. B Blakestad, C. Ospelkaus, A. P VanDevender, J. H Wesenberg, M. J Biercuk, D. Leibfried, and D. J Wineland. Near-ground-state transport of trapped-ion qubits through a multidimensional array. *Phys. Rev. A*, 84:032314, Sep 2011.

[7] R. Bowler, J. Gaebler, Y. Lin, T. R. Tan, D. Hanneke, J. D. Jost, J. P. Home, D. Leibfried, and D. J. Wineland. Coherent diabatic ion transport and separation in a multizone trap array. *Physical Review Letters*, 109(8), Aug 2012.

[8] Ryan Bowler. *Coherent Ion Transport in a Multi-electrode Trap Array,*. PhD thesis, University of Colorado, 2015.

[9] K. R. Brown, A. C. Wilson, Y. Colombe, C. Ospelkaus, A. M. Meier, E. Knill, D. Leibfried, and D. J. Wineland. Single-qubit-gate error below $\mathbf{10^{-4}}$ in a trapped ion. *Phys. Rev. A*, 84:030303, Sep 2011.

[10] M. Brownnutt, M. Kumph, P. Rabl, and R. Blatt. Ion-trap measurements of electric-field noise near surfaces. *Reviews of Modern Physics*, 87(4):1419–1482, Dec 2015.

[11] C. D. Bruzewicz, R. McConnell, J. Stuart, J. M. Sage, and J. Chiaverini. Dual-species, multi-qubit logic primitives for ca+/sr+ trapped-ion crystals. *npj Quantum Information*, 5(1), Nov 2019.

[12] Colin D. Bruzewicz, John Chiaverini, Robert McConnell, and Jeremy M. Sage. Trapped-ion quantum computing: Progress and challenges. *Applied Physics Reviews*, 6(2):021314, Jun 2019.

[13] J. Chiaverini and W. E. Lybarger. Laserless trapped-ion quantum simulations without spontaneous scattering using microtrap arrays. *Physical Review A*, 77(2), Feb 2008.

[14] Justin Christensen, David Hucul, Wesley Campbell, and Eric Hudson. High-fidelity manipulation of a qubit enabled by a manufactured nucleus. *npj Quantum Information*, 6, 12 2020.

[15] Ludwig E. de Clercq. *Transport of Trapped-Ion Qubits within a Scalable Quantum Processor,*. PhD thesis, ETH Zürich, 2015.

[16] AK Dhara and SV Lawande. Feynman propagator for time-dependent lagrangians possessing an invariant quadratic in momentum. *Journal of Physics A: Mathematical and General*, 17(12):2423, 1984.

[17] J.R. Dormand and P.J. Prince. A family of embedded runge-kutta formulae. *Journal of Computational and Applied Mathematics*, 6(1):19–26, 1980.

[18] Samuel Earnshaw. On the nature of the molecular forces which regulate the constitution of the luminiferous ether. *Transactions of the Cambridge Philosophical Society*, 7:97, 1848.

[19] H A Fürst, M H Goerz, U G Poschinger, M Murphy, S Montangero, T Calarco, F Schmidt-Kaler, K Singer, and C P Koch. Controlling the transport of an ion: classical and quantum mechanical solutions. *New Journal of Physics*, 16(7):075007, Jul 2014.

[20] J. P. Gaebler, T. R. Tan, Y. Lin, Y. Wan, R. Bowler, A. C. Keith, S. Glancy, K. Coakley, E. Knill, D. Leibfried, and D. J. Wineland. High-fidelity universal gate set for $^9\mathrm{Be}^+$ ion qubits. *Phys. Rev. Lett.*, 117:060505, Aug 2016.

[21] D. Guéry-Odelin and J. G. Muga. Transport in a harmonic trap: Shortcuts to adiabaticity and robust protocols. *Physical Review A*, 90(6), Dec 2014.

[22] D. Guéry-Odelin, A. Ruschhaupt, A. Kiely, E. Torrontegui, S. Martínez-Garaot, and J.G. Muga. Shortcuts to adiabaticity: Concepts, methods, and applications. *Reviews of Modern Physics*, 91(4), Oct 2019.

[23] Brian C Hall. *Quantum theory for mathematicians*, volume 267. Springer, 2013.

[24] Charles R. Harris, K. Jarrod Millman, Stéfan J. van der Walt, Ralf Gommers, Pauli Virtanen, David Cournapeau, Eric Wieser, Julian Taylor, Sebastian Berg, Nathaniel J. Smith, Robert Kern, Matti Picus, Stephan Hoyer, Marten H. van Kerkwijk, Matthew Brett, Allan Haldane, Jaime Fernández del Río, Mark Wiebe, Pearu Peterson, Pierre Gérard-Marchant, Kevin Sheppard, Tyler Reddy, Warren Weckesser, Hameer Abbasi, Christoph Gohlke, and Travis E. Oliphant. Array programming with NumPy. *Nature*, 585(7825):357–362, September 2020.

[25] T. P. Harty, D. T. C. Allcock, C. J. Ballance, L. Guidoni, H. A. Janacek, N. M. Linke, D. N. Stacey, and D. M. Lucas. High-fidelity preparation, gates, memory, and readout of a trapped-ion quantum bit. *Phys. Rev. Lett.*, 113:220501, Nov 2014.

[26] J. Home and A. Steane. Electrode configurations for fast separation of trapped ions. *Quantum Inf. Comput.*, 6:289–325, 2006.

[27] David Hucul, Mark Yeo, Winfried K Hensinger, James Rabchuk, Steven Olmschenk, and Christopher Monroe. On the transport of atomic ions in linear and multidimensional ion trap arrays. *arXiv preprint quant-ph/0702175*, 2007.

[28] Jose L. Jimenez. Lecture notes in chem-5181, October 2014.

[29] H. Kaufmann, T. Ruster, C. T. Schmiegelow, M. A. Luda, V. Kaushal, J. Schulz, D. von Lindenfels, F. Schmidt-Kaler, and U. G. Poschinger. Fast ion swapping for quantum-information processing. *Physical Review A*, 95(5), May 2017.

[30] H. Kaufmann, T. Ruster, C. T. Schmiegelow, M. A. Luda, V. Kaushal, J. Schulz, D. von Lindenfels, F. Schmidt-Kaler, and U. G. Poschinger. Scalable creation of long-lived multipartite entanglement. *Phys. Rev. Lett.*, 119:150503, Oct 2017.

[31] H Kaufmann, T Ruster, C T Schmiegelow, F Schmidt-Kaler, and U G Poschinger. Dynamics and control of fast ion crystal splitting in segmented paul traps. *New Journal of Physics*, 16(7):073012, Jul 2014.

[32] V. Kaushal, B. Lekitsch, A. Stahl, J. Hilder, D. Pijn, C. Schmiegelow, A. Bermudez, M. Müller, F. Schmidt-Kaler, and U. Poschinger. Shuttling-based trapped-ion quantum information processing, 2019.

[33] David Kielpinski, C.R. Monroe, and D.J. Wineland. Architecture for a large-scale ion-trap quantum computer. *Nature*, 417:709–11, 07 2002.

[34] Dieter Kraft. A software package for sequential quadratic programming. *Tech. Rep. DFVLR-FB 88-28, DLR German Aerospace Center – Institute for Flight Mechanics, Koln, Germany*, 1988.

[35] C. Langer, R. Ozeri, J. D. Jost, J. Chiaverini, B. DeMarco, A. Ben-Kish, R. B. Blakestad, J. Britton, D. B. Hume, W. M. Itano, D. Leibfried, R. Reichle,

T. Rosenband, T. Schaetz, P. O. Schmidt, and D. J. Wineland. Long-lived qubit memory using atomic ions. *Phys. Rev. Lett.*, 95:060502, Aug 2005.

[36] H R Lewis, Jr and W B Riesenfeld. An exact quantum theory of the time-dependent harmonic oscillator and of a charged particle in a time-dependent electromagnetic field. *J. Math. Phys. (N.Y.), 10: 1458-73 (Aug. 1969).*, 1 1969.

[37] H Ralph Lewis and PGL Leach. A direct approach to finding exact invariants for one-dimensional time-dependent classical hamiltonians. *Journal of Mathematical Physics*, 23(12):2371–2374, 1982.

[38] Jing Li, Qi Zhang, and Xi Chen. Trigonometric protocols for shortcuts to adiabatic transport of cold atoms in anharmonic traps. *Physics Letters A*, 381(38):3272–3275, Oct 2017.

[39] I. Lizuain, M. Palmero, and J. G. Muga. Dynamical normal modes for time-dependent hamiltonians in two dimensions. *Physical Review A*, 95(2), Feb 2017.

[40] Xiao-Jing Lu, J. G. Muga, Xi Chen, U. G. Poschinger, F. Schmidt-Kaler, and A. Ruschhaupt. Fast shuttling of a trapped ion in the presence of noise. *Physical Review A*, 89(6), Jun 2014.

[41] Xiao-Jing Lu, Mikel Palmero, Andreas Ruschhaupt, Xi Chen, and Juan Gonzalo Muga. Optimal transport of two ions under slow spring-constant drifts. *Physica Scripta*, 90(7):074038, 2015.

[42] Xiao-Jing Lu, A. Ruschhaupt, and J. G. Muga. Fast shuttling of a particle under weak spring-constant noise of the moving trap. *Physical Review A*, 97(5), May 2018.

[43] Xiao-Jing Lu, Andreas Ruschhaupt, Sofía Martínez-Garaot, and Juan Gonzalo Muga. Noise sensitivities for an atom shuttled by a moving optical lattice via shortcuts to adiabaticity. *Entropy*, 22(3):262, Feb 2020.

[44] Raymond E. March. An Introduction to Quadrupole Ion Trap Mass Spectrometry. *Journal of Mass Spectrometry*, 32(4):351–369, April 1997.

[45] Gabriel L. Mintzer. Motional state engineering for continuous-variable quantum computation. Bachelor of science thesis, Massachusetts Institute of Technology, 2021.

[46] C. Monroe and J. Kim. Scaling the ion trap quantum processor. *Science*, 339:1164 – 1169, 2013.

[47] A. H. Myerson, D. J. Szwer, S. C. Webster, D. T. C. Allcock, M. J. Curtis, G. Imreh, J. A. Sherman, D. N. Stacey, A. M. Steane, and D. M. Lucas. High-fidelity readout of trapped-ion qubits. *Phys. Rev. Lett.*, 100:200502, May 2008.

[48] Laurence W. Nagel and D.O. Pederson. Spice (simulation program with integrated circuit emphasis). Technical Report UCB/ERL M382, EECS Department, University of California, Berkeley, Apr 1973.

[49] Michael A. Nielsen and Isaac L. Chuang. *Quantum Computation and Quantum Information: 10th Anniversary Edition*. Cambridge University Press, USA, 10th edition, 2011.

[50] A. H. Nizamani and W. K. Hensinger. Optimum electrode configurations for fast ion separation in microfabricated surface ion traps. *Applied Physics B*, 106(2):327–338, Nov 2011.

[51] M. Palmero, R. Bowler, J. P. Gaebler, D. Leibfried, and J. G. Muga. Fast transport of mixed-species ion chains within a paul trap. *Physical Review A*, 90(5), Nov 2014.

[52] M. Palmero, S. Martínez-Garaot, D. Leibfried, D. J. Wineland, and J. G. Muga. Fast phase gates with trapped ions. *Physical Review A*, 95(2), Feb 2017.

[53] M Palmero, S Martínez-Garaot, U G Poschinger, A Ruschhaupt, and J G Muga. Fast separation of two trapped ions. *New Journal of Physics*, 17(9):093031, Sep 2015.

[54] M. Palmero, E. Torrontegui, D. Guéry-Odelin, and J. G. Muga. Fast transport of two ions in an anharmonic trap. *Physical Review A*, 88(5), Nov 2013.

[55] M Palmero, Shuo Wang, D Guéry-Odelin, Jr-Shin Li, and J G Muga. Shortcuts to adiabaticity for an ion in a rotating radially-tight trap. *New Journal of Physics*, 18(4):043014, apr 2016.

[56] Mikel Palmero. *Shortcuts to adiabaticity in trapped ions*. PhD thesis, University of the Basque Country - UPV/EHU, 2017.

[57] Wolfgang Paul. Electromagnetic traps for charged and neutral particles. *Rev. Mod. Phys.*, 62:531–540, Jul 1990.

[58] J. M. Pino, J. M. Dreiling, C. Figgatt, J. P. Gaebler, S. A. Moses, M. S. Allman, C. H. Baldwin, M. Foss-Feig, D. Hayes, K. Mayer, and et al. Demonstration of the trapped-ion quantum ccd computer architecture. *Nature*, 592(7853):209–213, Apr 2021.

[59] John Preskill. Quantum computing in the nisq era and beyond. *Quantum*, 2:79, Aug 2018.

[60] Luke Qi, John Chiaverini, Hilario Espinós, Mikel Palmero, and Juan Gonzalo Muga. Fast and robust particle shuttling for quantum science and technology, 2021.

[61] R. Reichle, D. Leibfried, R.B. Blakestad, J. Britton, J.D. Jost, E. Knill, C. Langer, R. Ozeri, S. Seidelin, and D.J. Wineland. Transport dynamics of single ions in segmented microstructured paul trap arrays. *Fortschritte der Physik*, 54(8-10):666–685, Aug 2006.

[62] Mary A Rowe, Amit Ben-Kish, Brian Demarco, Dietrich Leibfried, Volker Meyer, Jim Beall, Joe Britton, J Hughes, Wayne M Itano, Brana Jelenkovic, et al. Transport of quantum states and separation of ions in a dual rf ion trap. *arXiv preprint quant-ph/0205094*, 2002.

[63] T. Ruster, C. Warschburger, H. Kaufmann, C. T. Schmiegelow, A. Walther, M. Hettrich, A. Pfister, V. Kaushal, F. Schmidt-Kaler, and U. G. Poschinger. Experimental realization of fast ion separation in segmented paul traps. *Physical Review A*, 90(3), Sep 2014.

[64] S. Schulz, U. Poschinger, K. Singer, and F. Schmidt-Kaler. Optimization of segmented linear paul traps and transport of stored particles. *Fortschritte der Physik*, 54(8-10):648–665, Aug 2006.

[65] J. A. Sedlacek, J. Stuart, D. H. Slichter, C. D. Bruzewicz, R. McConnell, J. M. Sage, and J. Chiaverini. Evidence for multiple mechanisms underlying surface electric-field noise in ion traps. *Phys. Rev. A*, 98:063430, Dec 2018.

[66] M. A. Simón, M. Palmero, S. Martínez-Garaot, and J. G. Muga. Trapped-ion fock-state preparation by potential deformation. *Physical Review Research*, 2(2), Jun 2020.

[67] F Splatt, M Harlander, M Brownnutt, F Zähringer, R Blatt, and W Hänsel. Deterministic reordering of40ca+ions in a linear segmented paul trap. *New Journal of Physics*, 11(10):103008, Oct 2009.

[68] J. Stuart, R. Panock, C.D. Bruzewicz, J.A. Sedlacek, R. McConnell, I.L. Chuang, J.M. Sage, and J. Chiaverini. Chip-integrated voltage sources for control of trapped ions. *Phys. Rev. Applied*, 11:024010, Feb 2019.

[69] T. R. Tan, J. P. Gaebler, Y. Lin, Y. Wan, R. Bowler, D. Leibfried, and D. J. Wineland. Multi-element logic gates for trapped-ion qubits. *Nature*, 528(7582):380–383, Dec 2015.

[70] S. L. Todaro, V. B. Verma, K. C. McCormick, D. T. C. Allcock, R. P. Mirin, D. J. Wineland, S. W. Nam, A. C. Wilson, D. Leibfried, and D. H. Slichter. State readout of a trapped ion qubit using a trap-integrated superconducting photon detector. *Phys. Rev. Lett.*, 126:010501, Jan 2021.

[71] Susanna L. Todaro. *Scalable state detection and fast transport of trapped-ion qubits for quantum computing*. PhD thesis, University of Colorado at Boulder, 2020.

[72] E. Torrontegui, S. Ibáñez, Xi Chen, A. Ruschhaupt, D. Guéry-Odelin, and J. G. Muga. Fast atomic transport without vibrational heating. *Physical Review A*, 83(1), Jan 2011.

[73] Martin W. van Mourik, Esteban A. Martinez, Lukas Gerster, Pavel Hrmo, Thomas Monz, Philipp Schindler, and Rainer Blatt. Coherent rotations of qubits within a surface ion-trap quantum computer. *Phys. Rev. A*, 102:022611, Aug 2020.

[74] Pauli Virtanen, Ralf Gommers, Travis E. Oliphant, Matt Haberland, Tyler Reddy, David Cournapeau, Evgeni Burovski, Pearu Peterson, Warren Weckesser, Jonathan Bright, Stéfan J. van der Walt, Matthew Brett, Joshua Wilson, K. Jarrod Millman, Nikolay Mayorov, Andrew R. J. Nelson, Eric Jones, Robert Kern, Eric Larson, C J Carey, İlhan Polat, Yu Feng, Eric W. Moore, Jake VanderPlas, Denis Laxalde, Josef Perktold, Robert Cimrman, Ian Henriksen, E. A. Quintero, Charles R. Harris, Anne M. Archibald, Antônio H. Ribeiro, Fabian Pedregosa, Paul van Mulbregt, and SciPy 1.0 Contributors. SciPy 1.0: Fundamental Algorithms for Scientific Computing in Python. *Nature Methods*, 17:261–272, 2020.

[75] J. Vogel, W. Li, A. Mokhberi, I. Lesanovsky, and F. Schmidt-Kaler. Shuttling of rydberg ions for fast entangling operations. *Phys. Rev. Lett.*, 123:153603, Oct 2019.

[76] A. Walther, F. Ziesel, T. Ruster, S. T. Dawkins, K. Ott, M. Hettrich, K. Singer, F. Schmidt-Kaler, and U. Poschinger. Controlling fast transport of cold trapped ions. *Physical Review Letters*, 109(8), Aug 2012.

[77] Yong Wan, Robert Jördens, Stephen D. Erickson, Jenny J. Wu, Ryan Bowler, Ting Rei Tan, Pan-Yu Hou, David J. Wineland, Andrew C. Wilson, and Dietrich Leibfried. Ion transport and reordering in a 2d trap array. *Advanced Quantum Technologies*, 3(11):2000028, May 2020.

[78] Yong Wan, Daniel Kienzler, Stephen D. Erickson, Karl H. Mayer, Ting Rei Tan, Jenny J. Wu, Hilma M. Vasconcelos, Scott Glancy, Emanuel Knill, David J. Wineland, and et al. Quantum gate teleportation between separated qubits in a trapped-ion processor. *Science*, 364(6443):875–878, May 2019.

[79] Ye Wang, Mark Um, Junhua Zhang, Shuoming An, Ming Lyu, Jing-Ning Zhang, L-M Duan, Dahyun Yum, and Kihwan Kim. Single-qubit quantum memory exceeding ten-minute coherence time. *Nature Photonics*, 11(10):646–650, 2017.

[80] DJ Wineland, C Monroe, WM Itano, D Leibfried, BE King, and DM Meekhof. Experimental issues in coherent quantum-state manipulation of trapped atomic ions. *Journal of research of the National Institute of Standards and Technology*, 103(3):259—328, 1998.

[81] Qi Zhang, Xi Chen, and David Guéry-Odelin. Fast and optimal transport of atoms with nonharmonic traps. *Physical Review A*, 92(4), Oct 2015.